Silicon Micromachined Vibrating Gyroscopes with Piezoresistive Detection and Electromagnetic Excitation

A dissertation submitted to the Faculty of Sciences of the University of Neuchâtel, in fulfillment of the requirements for the degree of "*Docteur ès Sciences*"

by

Florence Grétillat
Ingénieur en Physique et Matériaux
Institut National des Sciences Appliquées de Lyon (INSA)

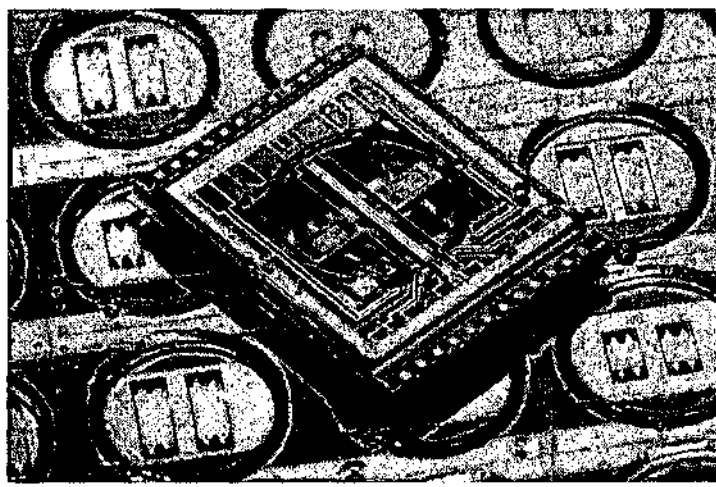

Cotutelle entre l'Université de Franche-Comté (Besançon France) et l'Université de Neuchâtel (Neuchâtel Suisse)

Institut de Microtechnique
Université de Neuchâtel
Rue Jaquet-Droz 1, CH-2007 Neuchâtel

1998

IMPRIMATUR POUR LA THÈSE

Silicon micromachined vibrating gyroscopes with piezoresistive detection and electromagnetic excitation

de Mme Florence Grétillat-Paoletti

UNIVERSITÉ DE NEUCHÂTEL

FACULTÉ DES SCIENCES

La Faculté des sciences de l'Université de Neuchâtel sur le rapport des membres du jury,

MM. N. de Rooij (directeur de thèse), F. Pellandini, D. Hauden (Besançon) et J. Söderkvist (Suède)

autorise l'impression de la présente thèse.

Neuchâtel, le 19 novembre 1998

Le doyen:

F. Stoeckli

à mes parents
à Marc

Contents

Abbreviation table:

Abbreviation	*Description*
AC	Alternative current
A/D	Analog-to-digital
Al	Aluminum
BHF	Buffered hydrofluoric acid
Co	Cobalt
CVD	Chemical vapor deposition/deposited
DC	Direct current
DIL	Dual in line socket
DSP	Digital signal processing
FEM	Finite element modeling
HF	Hydrofluoric acid
HNO_3	Nitric acid
IC	Integrated circuit
IMT	Institute of Microtechnology
KOH	Potassium hydroxyde
LPCVD	Low pressure chemical vapor deposition/deposited
MEMS	Microelectromechanical system
NH_4F	Ammonium fluoride

Abbreviation	***Description***
Polysilicon	Polycrystalline silicon
RIE	Reactive ion etching
SEM	Scanning electron microscope
Si	Silicon
Si_3N_4	Silicon nitride
SiO_2	Silicon dioxide
SUB	Subminiature
µ-TAS	Miniaturized total analysis system
rms	Root mean square

Symbols and Units:

Symbol	Description	Units
Δf	Bandwidth at -3 dB	Hz
σ	Stress	Pa
π	Piezoresistance coefficient	Pa^{-1}
v	Noise	V
ω	Angular frequency (see f: $\omega=2\pi f$)	rad/sec
f	Resonance frequency	Hz
dB	Decibel: $20\cdot\log(V_{out}/V_{in})$	dB
Q	Quality factor: $Q=f/\Delta f$	
$\Omega_{\square}$	Sheet resistance	Ω
k	Boltzman constant ($1.38066\ 10^{-23}$ J/K)	J/K
L	Length of the driving metallic line	m
I	Current amplitude	A
B	Magnetic induction	T
F_l	Lorentz force	N
F_c	Coriolis force	N
m	Mass	kg
v	Velocity	m/sec
Ω	Angular rate	rad/sec
X	Amplitude of vibration	m
R	Resistance	Ω
ΔR	Resistance change	Ω

Symbol	Description	Units
V_b	Voltage over the Wheatstone bridge	V
ΔV	Differential output voltage	V
T	Temperature	K
TCE	Thermal expansion coefficient	ppm/K
TCO	Temperature coefficient of offset	µV/V/K
TCR	Temperature coefficient of resistance	ppm/K
ZRO	Zero rate output	rad/sec

Résumé

Ce résumé en français de la présente thèse répond à deux nécessités. D'une part, ce projet s'inscrit dans le cadre PICS (Projet International de Coopération Scientifique entre des institutions françaises et suisses de recherche en microtechnique) et fait l'objet d'une cotutelle de thèse entre l'Université de Franche-Comté de Besançon et l'Université de Neuchâtel. Comme cette thèse est rédigée en anglais, elle doit comporter un résumé en français pour satisfaire les exigences de la cotutelle. D'autre part, ce résumé devrait permettre au lecteur non familiarisé avec la langue de Shakespeare de connaître les grandes lignes de ce travail.

Ce projet s'inscrit dans le cadre général de recherche des limites en microtechnique. La microtechnique fait appel au savoir faire de la microélectronique qui intervient dans le domaine des microprocesseurs d'ordinateurs, des téléphones sans fil, des cartes à puces...Son but est de réaliser des microcapteurs qui mesurent une grandeur physique (température , pression) et qui transforment cette dernière en signal électrique, des microactionneurs qui effectuent une opération précise comme le ferait un micromoteur ou une microvalve. Si on arrive à combiner capteurs et actionneurs afin qu'ils agissent de façon autonome et intelligente, on forme alors un microsystème.

Pour estimer les limites de la microtechnique, un démonstrateur a été choisi. Il s'agit d'un microsystème de navigation. Certaines voitures sont déjà équipées d'un système de navigation qui permet de guider un véhicule dans une ville sans chauffeur: un ordinateur de bord suit la position de la voiture et la guide grâce à des cartes enregistrées sur CD Rom. Ce dispositif est non seulement coûteux mais présente aussi certaines limites: ces cartes nécessitent une mise à jour constante car des travaux ou des déviations ponctuelles ne figurent pas dessus. Le GPS (Global Positionning System) donne la position (latitude et longitude) en quelques minutes grâce à des repérages par satellites. En cas d'obstacles (immeuble, tunnel, montagne) entre le récepteur GPS et les satellites, le signal électromagnétique n'est plus transmis. Il faudrait lui

associer une plate-forme inertielle. Cette dernière grâce à trois capteurs d'accélération et trois capteurs de vitesse angulaire délivrerait une position suivant les trois axes de coordonnées dans l'espace.

Dans ce projet, les capteurs de force (accélération et vitesse angulaire) utilisent les techniques de la microtechnique. En effet plusieurs capteurs peuvent être fabriqués en grand nombre (taille micrométrique) et à faible coût sur un même substrat en silicium. Le capteur d'accélération micro-usiné en silicium intervient déjà dans les systèmes de coussin gonflant dans les voitures. Il transforme, grâce au corps d'épreuve, une force (accélération) en une contrainte mécanique qui à son tour sera transformée en un signal électrique grâce à des jauges de contraintes appelées piezorésistances. Ces dernières changent une contrainte mécanique en variation de résistance électrique.

Ce principe de mesure a été repris pour les deux capteurs de vitesse angulaire réalisés dans cette thèse. Ce n'est pas une accélération que l'on mesure mais la force de Coriolis. Cette force agit sur tout corps en mouvement contenu dans un plan qui tourne à une vitesse donnée Ω. Par exemple lorsqu'on vide l'eau d'une baignoire, un tourbillon se forme dans le sens des aiguilles d'une montre. Dans l'hémisphère sud, le tourbillon tournera dans le sens inverse et ceci grâce à la rotation de la terre sur elle même. Dans le cas d'un capteur de vitesse angulaire, le corps d'épreuve est constitué par un diapason dont les deux branches vibrent en antiphase (toujours dans des directions opposées). Ce dispositif a déjà été réalisé avec succès en quartz et intervient dans les systèmes de stabilisation des caméras.

Dans cette thèse, deux capteurs de vitesse angulaire basés sur une structure vibrante ont été conçus, fabriqués et caractérisés (chapitres 2 et 4). Dans les deux cas, les deux branches du diapason ont été remplacées par deux accéléromètres, c'est à dire, deux masses suspendues par quatre poutres chacune. L'excitation en antiphase se fait grâce aux forces électromagnétiques Un aimant permanent collé sur le capot supérieur de protection des masses vibrantes interagit avec un courant alternatif qui circule dans un conducteur métallique placé sur les masses. Lorsqu'on fait tourner le capteur, les masses ne vibrent plus dans un même plan mais hors de ce plan dans des directions opposées. Ceci induit des contraintes mécaniques dans les poutres qui sont détectées par des piezoresistances. Chacun des capteurs nous a permis de mesurer des vitesses de plus d'un tour par seconde (400 deg/sec) ainsi que le

sens de rotation. Le deuxième prototype de capteur de vitesse angulaire présente plusieurs améliorations par rapport au premier design. En particulier, un signal de sortie beaucoup moins bruité et surtout beaucoup plus stable dans le temps, ce qui est particulièrement important pour un capteur de vitesse angulaire destiné à la navigation car il devra mesurer un signal pendant plusieurs minutes sans subir de dérive causée par exemple, par une variation de température.

Un paragraphe supplémentaire (chapitre 3) traite d'un problème commun aux deux prototypes de capteur de vitesse angulaire: l'encapsulation. L'utilisation de masses vibrantes nécessite une protection pour éviter tout choc important et faciliter sa manipulation. Pour cela, nous avons mis au point une technique particulière d'usinage du verre. La structuration du verre fait appel aux techniques de photolithographie et d'usinage chimique comme pour la microélectronique. Les capots de verre sont ensuite fixés sur les chips en silicium et le capteur est prêt pour les mesures.

Pour conclure, j'aimerais souligner l'enrichissement que m'a procuré ce travail par la diversité des techniques utilisées et la variété des problèmes abordés. Ce travail a aussi suscité un intérêt certain dans quelques conférences. De nombreux efforts restent à fournir pour envisager une commercialisation d'un de ces prototypes. Cependant, parmi les objectifs atteints, un des plus importants réside dans la formation du doctorat, la manière d'appréhender des nouveaux problèmes, résoudre ces derniers avec un maximum d'efficacité et savoir gérer l'information et les moyens à sa disposition. Pour ma part, ces objectifs sont atteints et l'intérêt qu'a suscité ce travail dans différents domaines constitue déjà une très grande récompense.

1. Introduction

1.1 Inertial sensors:

1.1.1 Accelerometers:

Micromachined inertial sensors, consisting of accelerometers and gyroscopes, are one of the most important types of silicon-based sensors. Microaccelerometers alone have the second largest sales volume after pressure sensors. This is due to their automotive applications where they are used to activate safety systems, including air bag, to implement vehicle stability systems and electronic suspensions [1.1].

An accelerometer generally consists of a proof mass suspended by compliant beams anchored to a fixed frame. External acceleration displaces the support frame relative to the proof mass, which changes the internal stress in the suspension beam. Both this relative displacement and the suspension-beam stress can be used as a measure of the external acceleration. A variety of transduction mechanisms have been used in microaccelerometers: piezoresistive, capacitive, tunneling current, resonant frequency, thermal, optical, electromagnetic and piezoelectric [1.2, 1.3, 1.4].

Accelerometers are typically specified by their sensitivity, maximum operation range, frequency response, resolution, full-scale non linearity, offset, off-axis sensitivity and shock survival. Since micromachined accelerometers are used in a wide range of applications, their specifications are also application dependent and cover a rather broad spectrum. For instance, for microgravity measurements devices with a range of operation greater than ±0.1g, a resolution of less than 1 μg in a frequency range of 0 Hz to 1 Hz are desired, while in ballistic and impact sensing applications, a range of more than 10 000g with a resolution of less than 1 g in a 50 kHz bandwidth is required.

Today microaccelerometers with low and medium sensitivity are in large volume production with prices under $5 and it is believed that gyroscopes will soon be mass produced at similar volumes [1.2, 1.3, 1.4].

1.1.2 Gyroscope applications:

The successful commercial impact of microaccelerometers opens new application domain for another micromachined sensor: the angular rate sensor or gyroscope for measuring the angular velocity. The needs for small and inexpensive gyroscopes are constantly increasing, while new automotive and consumer applications emerge (Table 1.1) [1.5, 1.6, 1.7, 1.8, 1.9, 1.10, 1.11].

Area	Examples of applications	Range	Resolution
automotive safety	improved controls for airbags, anti-skids	200 deg/sec 100 deg/sec	10 deg/sec 1 deg/sec
consumer	anti-jitters compensation for video camera	50 deg/sec	0.5 deg/sec
industrial	machine control	10 deg/sec	0.01 deg/sec
medical	monitoring of body-movement	100 deg/sec	1 deg/sec

Table 1.1: some new applications which need small or inexpensive micromachined gyroscopes, including estimates of typical performances [1.5].

Like the microaccelerometers, the micromachined gyroscopes can be used in a wide range of domains, their required specifications are also application dependent. Resolution (accuracy), drift, zero-rate output (ZRO) or bias and scale factor are important factors that determine the performance of a gyroscope [1.1]. Due to the main commercial impact of the automotive market, many micromachined gyroscopes have been developed for this field [1.12, 1.13, 1.14, 1.15, 1.16, 1.17]. An other promise application for micromachined gyroscope is the automotive navigation system. Studies on automotive navigation systems began in the late 1960's, autonomous inertial navigation technologies as well as radio-aided ones have been developed to locate vehicles positions [1.18]. One of the most promising system is the Global Positioning System (GPS) combined with inertial sensors. Satellites with an orbit time of about 12 hours (corresponding to a satellite distance from the earth's surface of about

20 000 km) transmit an electromagnetic signal that travels at the speed of light. These transmitted microwave signals are received by a high gain receiver on board the vehicle. The range between satellite and vehicle can be calculated from the signal's traveling time multiplied by the speed of light. The traveling time is the time difference measured by two precise clocks, one in the satellite another in the vehicle [1.19]. This system requires a minimum of three visible satellites and updates of the position can only be obtained at a few minutes interval. Ground interferences from tall buildings, mountains, tunnels can prolong this time. There is a need for an additional inertial navigation system (INS) which gives the position in-between the updates. Micromachined accelerometers and angular rate sensors will make such systems economically realistic [1.5, 1.18, 1.20, 1.21, 1.22, 1.23, 1.24, 1.25, 1.26, 1.27].

1.2 The concept of the vibrating gyroscope:

1.2.1 Coriolis force:

Almost all reported micromachined gyroscopes use vibrating mechanical elements to sense rotation. They have no rotating parts that require bearings and hence they can be easily miniaturized and batch fabricated using micromachining techniques [1.1]. All vibratory gyroscopes are based on the transfer of energy between two vibration modes of a structure caused by Coriolis acceleration. Coriolis acceleration is an apparent acceleration that arises in a rotating reference frame and is proportional to the rate of rotation. To understand the Coriolis effect, imagine a particle traveling in space with a velocity vector **v**. An observer, sitting on the *x*-axis of the *xyz* coordinate system shown in Figure 1.1, is watching the particle. If the coordinate system along with the observer starts rotating around the *z*-axis with an angular velocity Ω, the observer thinks that the particle is changing its trajectory toward the *x*-axis with an acceleration equal to $2\mathbf{v} \times \Omega$ [1.1, 1.21].

1.2.2 The tuning fork gyroscope:

A number of vibratory gyroscopes have been demonstrated including tuning forks, vibrating beams and vibrating shells [1.5, 1.28, 1.29, 1.30, 1.31]. The tuning fork design, as illustrated in Figure 1.2, is operated by vibrating two tines in antiphase in one plane. A rotation around the axis, which is parallel with the tines, will generate a vibration out of this plane due to the Coriolis

force. The out of plane deflection of the tines will allow the Coriolis force and thus the rotation rate to be measured.

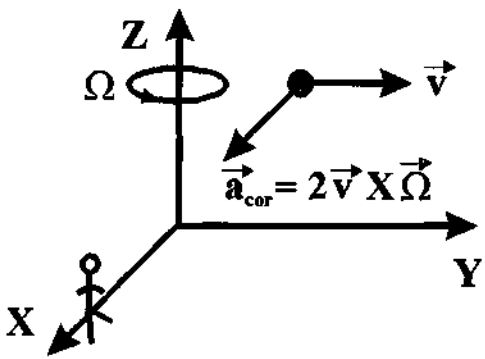

Figure 1.1: the Coriolis effect.

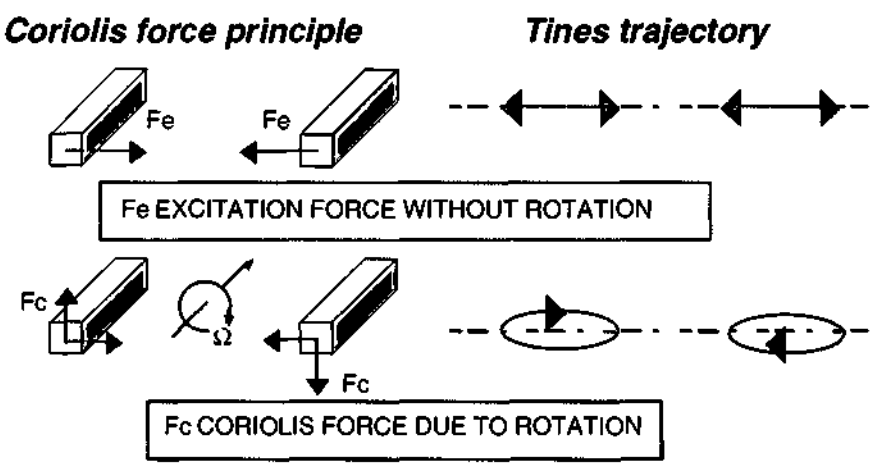

Figure 1.2: the tuning fork principle. The amplitude of the Coriolis force (Fc) depends on the tine mass (m), the velocity of the antiphase vibration (v) and the speed of the rotation (Ω). The oval vibration pattern of the tines trajectory indicates that the tines are vibrating out of the rotating plane.

The vibrating bar can be considered as a half tuning fork and be built-up with an accelerometer [1.32] or a clover-leaf-shaped resonator (Figure 1.3) [1.24]. For the tuning fork also, the two tines can be replaced by two accelerometers to combine proof masses with flexible suspension beams (Figure 1.4) [1.33]. In this work, the tuning fork design built-up with two accelerometers has been chosen.

Not only tuning forks can sense rotation with the Coriolis forces, the vibrating ring concept can be used for a vibrating gyroscope. The ring is vibrated into an in-plane elliptically shaped primary flexural mode. When it is subjected to rotation around its normal axis, Coriolis forces cause energy to be transfer from the primary mode to the secondary flexural mode, which is located 45° apart from the primary mode (Figure 1.5).

These different vibrating gyroscope concepts have been successfully tested and their performances will be compared in chapter 5.

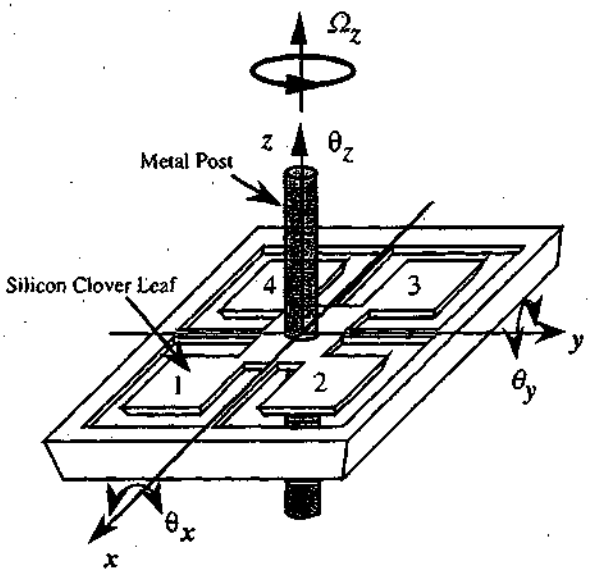

Figure 1.3: the clover-leaf shaped gyroscope design. The leaves 1 and 2 are vibrating in antiphase while the leaves 3 and 4 are sensing the Coriolis force effect [1.24].

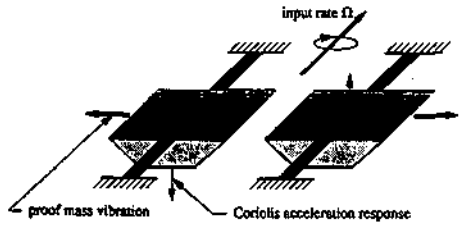

Figure 1.4: the two accelerometers design for a vibrating gyroscope [1.31].

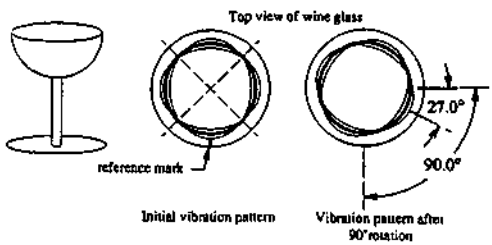

Figure 1.5: vibrating ring gyroscope concept illustrated by a wine glass [1.31].

1.3 Excitation and detection principles:

1.3.1 Motivations:

The application domain will be an inertial navigation system with three gyroscopes and a three axis accelerometer coupled with a GPS. Microsystems or microelectromechanical systems (MEMS) are promising devices because they should integrate all the know-how of the microtechnology: realization of sensors with high performances and a high level of integration (4 sensors with electronics combined with a data processing system). Moreover, navigation microsystems are dedicated to automotive applications thus robustness, low cost and reliability are the main criteria. The whole study of the navigation microsystem has been divided between four Ph. D. students [1.34].

This work is dedicated to the design, the fabrication and the realization of a micromachined silicon gyroscope. As already mentioned, the vibrating concept of the tuning fork has been chosen. For the silicon micromachined gyroscope, the limits in the microtechnology were investigated in the following

way: the micromachining of silicon through a wafer and the piezoresistive effect of silicon [1.35, 1.36, 1.37, 1.38].

At the starting point of this work, some relevant devices have been already published and we tried also to find a new combination of excitation and detection principles (Table 1.2).

Excitation Principle	*Capacitive Detection*	*Piezoelectric Detection*	*Piezoresistive Detection*
electromagnetic	[1.39]		**OUR APPROACH**
electrostatic	[1.31, 1.32, 1.33]		
piezoelectric	[1.30]	[1.5]	

Table 1.2: principles of excitation and detection of several micromachined gyroscopes.

1.3.2 Lorentz forces:

The silicon micromachined gyroscope should be driven dynamically to sense a rotation rate by the Coriolis forces. Due to the tuning fork design, common mode signal due to a linear acceleration can be canceled by exciting both tines in antiphase.

Many devices are relying on electrostatic forces but these forces are depending from the position of the vibrating structure and the levitation effect can induce in the sensing direction an output without any rotation [1.40]. Thus we preferred the electromagnetic forces or Lorentz forces [1.36]. When a constant magnetic induction (B) is interacting with a metallic conductor (length L) with an AC current (I) flowing through the conductor, Lorentz forces are moving the conductor in a direction perpendicular to the plan formed by the conductor and the magnetic induction direction.

$$F = I * L \times B \qquad [1.36]$$

AC current is required for the dynamic driving because the magnetic induction B will be provided by a permanent magnet. An appropriate design in U shape of the metallic conductor will allow the antiphase excitation of the tines of the tuning fork. Driving silicon tuning forks with electromagnetic forces has been successfully tested [1.41]. The excitation of about one millimeter long tuning forks was performed with a power of 20 µWatts. Moreover the metallic line is not necessary on both faces of the tines. One metallic line on the top side of the tines is efficient [1.41].

1.3.3 Piezoresistors:

Piezoresistivity is a material property where the bulk resistivity is influenced by the mechanical stresses applied to the material. All materials have a piezoresistor effect to some extent, but it is particularly important in some semiconductors like monocrystalline silicon [1.36, 1.42, 1.43]. Using the piezoresistivity of silicon to sense stress in a membrane highlights several advantages: the integration of the gauges on the membrane ensures a perfect transfer of the strain, the resistors are limited to the surface of the bending elements in where the stress is maximal, moreover mass fabrication techniques can be used [1.36]. This technique has been successfully used for pressure sensors [1.37] and accelerometers [1.38].

The piezoresistivity of silicon can be characterized by the longitudinal π_l and the transverse π_t piezoresistor coefficients. For the first one, the current and the mechanical force directions are the same, for the second one, the current and the force directions are perpendicular. Then the resistor change ΔR from stresses that are longitudinal (σ_l) and transverse (σ_t) is given by:

$$\frac{\Delta R}{R} = \sigma_l * \pi_l + \sigma_t * \pi_t \qquad [1.36]$$

For (100) silicon wafer, the membrane or beam direction will be (110), thus (p) type resistors will be preferred because π_l and π_t are maximum. As silicon is a cubic crystal, π_l and π_t can be described by several coefficients π_{11}, π_{12} and π_{44} [1.36].

$$\pi_{l} = \frac{1}{2} * (\pi_{11} + \pi_{12} + \pi_{44}) \qquad [1.36]$$

$$\pi_{t} = \frac{1}{2} * (\pi_{11} + \pi_{12} - \pi_{44}) \qquad [1.36]$$

For p-type piezoresistors, π_{44} is by far more important than the other two coefficients [1.36]. Moreover, by an appropriate design of the resistor (U shape), the transverse term can be canceled [1.37].

$$\frac{\Delta R}{R} = \frac{\pi_{44}}{2} * (\sigma_{l} - \sigma_{t}) \approx \frac{\pi_{44}}{2} * (\sigma_{l}) \qquad [1.36]$$

for (p) type resistors with a resistivity of 7-8 Ω.cm:

$\pi_{44} = +138.1\ 10^{-11}\ Pa^{-1}$ [1.36]

With the tuning fork design, the stress induced in each tines by the Coriolis forces will be of opposite sign and then the resistors changes also. Thus the Wheatstone bridge configuration can be used and it converts the resistor change directly to a voltage signal (Figure 1.6). The differential output voltage (ΔR) of an ideally balanced bridge with assumed identical (but opposite in sign) resistor changes is given by:

$$\Delta V = \frac{\Delta R}{R} * V_{b} \qquad [1.36]$$

where R is the zero stress resistor and V_b the bridge supply voltage.

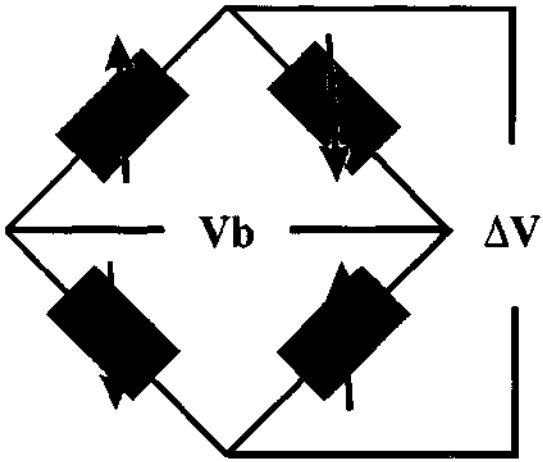

$$\Delta V = \Delta R/R * Vb$$

Figure 1.6: Wheatstone bridge configuration of four resistors.

1.4 Outline of the thesis:

This chapter gives a short description of the vibrating gyroscope design and some examples of concept. The principles of excitation and detection of the sensor are presented and motivated in view of their application in two prototypes gyroscopes. The fabrication and the characterization of two angular rate sensor designs will be presented in chapter 2 and 4 respectively. Chapter 3 describes the packaging technique used for both prototype gyroscopes. In chapter 5, the performances of each angular rate sensors will be discussed and compared with other published devices. Finally the conclusion of this work and an outlook will be given.

1.5 References:

[1.1] N. Yazdi, F. Ayazi, K. Najafi, "Micromachined inertial sensors", Proceedings of the IEEE Special Issue: integrated sensors, microactuators and microsystems (MEMS), Vol. 86 N° 3, August 1998, pp. 1640-1659.

[1.2] H. Jakobsen, "Sensor foundries and production of sensors at Sensonor A.S", Technical Digest of The 6th Workshop on Micromachining, Micromechanics and Microsystems, MME '95, Copenhagen, Denmark, September 1995, pp. 324-329.

[1.3] W. Kuehnel and S. Sherman, "A Surface Micromachined Silicon Accelerometer with On-Chip Detection Circuitry", Sensors & Actuators, A45 (1994), pp. 7-16.

[1.4] G. A. Macdonald, "A review of low cost accelerometers for vehicle dynamics", Sensors & Actuators A - Physical, A21-23 1990, pp. 303-307.

[1.5] J. Söderkvist, "Micromachined gyroscopes", Digest of Technical Papers of the 7th International Conference on Solid-State Sensors and Actuators, Transducers '93, Yokohama, Japan, June 1993, pp. 638-641.

[1.6] J. Söderkvist, "Micromachined gyroscopes", Sensors & Actuators A - Physical, Vol. A43 1994, pp. 65-71.

[1.7] J. Söderkvist, "Micromachined vibrating gyroscopes", Proceedings of the 2nd Micro Structure Workshop, Uppsala, Sweden, March 1996, pp. 14.1-14.6.

[1.8] P. E. M. Frere, "Problems of using accelerometers to measure angular rate in automobiles ", Sensors & Actuators A - Physical, A 25-27 1991, 821-824.

[1.9] J. A. Green, "A path to low cost gyroscopy", Technical Digest of IEEE Solid-State Sensor and Actuator Workshop, Hilton Head Island, SC, June 1998, pp. 51-54.

[1.10] W. Gottschling, J. Rispal, "Advanced piezo-vibrator gyroscope technology for volume applications today and tomorrow", Proceedings of Symposium Gyro Technology 1996, Stuttgart, Germany, September 1996, pp. 16.0-16.9.

[1.11] B. Barshan and H. F. Durrant-Whyte, "Evaluation of a solid-state gyroscope for robotics applications", IEEE Transactions on Instrumentation & Measurement, Vol. 44 N°. 1 1995, pp. 61-67.

[1.12] J. P. Colinot, V. Hernette and Ph. Jarri, "Gyrometer application for a low-frequency active suspension", Sensors & Actuators A - Physical, A 37-38 1993, 116-120.

[1.13] R. H. Grace, "Automotive applications of microelectromechanical systems (MEMS)", Proceedings Sensors Expo Anaheim, Anaheim, CA, April 1996, pp. 133-141.

[1.14] D. S. Eddy, D. R. Sparks, "Applications of MEMS technology in automotive sensors and actuators", Proceedings of the IEEE Special Issue: integrated sensors, microactuators and microsystems (MEMS), Vol. 86 N° 3, August 1998, pp. 1747-1755.

[1.15] J. H. Martin, "Micromechanical gyroscope packaging history and projections", Proceedings of the 1994 International Electronics Packaging Conference, Atlanta, GA, September 1994, pp. 470-480.

[1.16] C. Song, "Commercial vision of silicon based inertial sensors ", Digest of Technical Papers of the 9th International Conference on Solid-State Sensors and Actuators, Transducers '97, Chicago, IL, June 1997, pp. 839-842.

[1.17] R. E. Sulouff, Jr., "Silicon sensors for automotive applications", Digest of Technical Papers of the 6th International Conference on Solid-State Sensors and Actuators, Transducers '91, San Francisco, CA, June 1991, pp. 170-176.

[1.18] S. Oho, H. Kajioka and T. Sasayama, "Optical fiber gyroscope for automotive navigation", IEEE Transactions on Vehicular Technology, Vol. 44, N°. 3 1995, pp. 698-705.

[1.19] G. Schänzer, "High precision navigation for vehicles", Proceedings of the 20th international conference on Industrial Electronics Control and Instrumentation, IECON'94, Bologna, Italy, September 1994, pp. 1706-1711.

[1.20] T. J. Hawkey, R. P. Torti, "Integrated microgyroscope", Proceedings of the SPIE 1992 Conference: Sensors and Sensor Systems for Guidance and Navigation II, Orlando, FL, April 1992, pp. 199-207.

[1.21] A. Lawrence, "Modern inertial technology: navigation, guidance and control", Springer-Verlag New York, Inc., 1993.

[1.22] K. Kobayashi, S. Kawasaki and K. Watanabe, "Accurate navigation via sensor fusion of GPS and rate-gyro", Proceedings of Intelligent Vehicles Symposium, July 1993, pp. 449-454.

[1.23] T. Sasayama, "Sensors and sensing technology for intelligent vehicle era", Proceedings of the 9th International Conference on Automotive Electronics, London, UK, May 1994, pp. 61-67.

[1.24] W. C. Tang, "MEMS applications in space exploration", Proceedings of the SPIE 1997 Conference: Micromachined Devices and Components III, Austin, TX, September 1997, pp. 202-211.

[1.25] W. C. Tang, "Micromachines blast off into space", Vacuum Solutions Technology & Applications, May 1998 Issue 4, pp. 26-29.

[1.26] H. Tsuji, H. Maeda, A. Shibata and F. Morisue, "Evaluation of location system combining a GPS receiver with inertial sensor", Proceedings of the Vehicle Navigation and Information Systems Conference, October 1991, pp. 645-649.

[1.27] T. Yuhara, T. Kumagai, H. Soekawa and H. Hajioka, "Fiber-optic gyroscopes for automotive applications", Journal of Circuits Systems and Computers, Vol. 5 N°. 1 1995, pp. 17-36.

[1.28] S. Dalla Piazza and M. Christen, "Quartz crystal rotation rate sensors", Proceedings of the 7th European Frequency and Time Forum Neuchâtel, Neuchâtel, Switzerland, March 1993.

[1.29] R. Voss, "Silicon micromachined vibrating gyroscopes", Proceedings of the SPIE 1997 Conference: Micromachined Devices and Components III, Austin, TX, September 1997, pp. 62-73.

[1.30] K. Maenaka and T. Shiozawa, "Silicon rate sensor using anisotropic etching technology", Digest of Technical Papers of the 7th International Conference on Solid-State Sensors and Actuators, Transducers '93, Yokohama, Japan, June 1993, pp. 642-645.

[1.31] M. W. Putty and K. Najafi, "A micromachined vibratory ring gyroscope", Technical Digest of IEEE Solid-State Sensor and Actuator Workshop, Hilton Head Island, SC, June 1994, pp. 213-220.

[1.32] P. Greiff, B. Boxenhorn, T. King, L. Niles, "Silicon monolithic micromechanical gyroscope", Digest of Technical Papers of the 6th International Conference on Solid-State Sensors and Actuators, Transducers '91, San Francisco, CA, June 1991, pp. 966-968.

[1.33] J. Bernstein, S. Cho, A. T. King, A. Kourepenis, P. Maciel and M. Weinberg, "A micromachined comb-drive tuning fork rate gyroscope", Proceedings of the 6th IEEE Workshop on Micro Electro Mechanical Systems, MEMS '93, Fort Lauderdale, FL, February 1993, pp. 143-148.

[1.34] Y. Ansel, P. Lerch, P. Renaud, F. Paoletti, M.-A. Grétillat, N. F. de Rooij, G. Schröpfer, S. Ballandras, M. de Labachelerie, C. Marselli, H. P. Amann and F. Pellandini, "Simulation and design of a three axis navigation microsystem based on micromachined sensors", Proceedings of the 2nd International Conference: Microsim'97, Lausanne, Switzerland, September 1997, pp. 107-116.

[1.35] S. M. Sze, "Semiconductor devices: physics and technology", John Wiley & Sons, Inc., 1985.

[1.36] S. M. Sze, "Semiconductor sensors", John Wiley & Sons, Inc., 1994.

[1.37] B. Kloeck, "Design, fabrication and characterization of piezoresistive pressure sensor, including the study of electrochemical etch-stop", Ph. D. dissertation, Institute of Microtechnology, University of Neuchâtel, Switzerland, 1989.

[1.38] T. Tschan, "Simulation, design and characterization of a silicon piezoresistive accelerometer, fabricated by a bipolar-compatible industrial process", Ph. D. dissertation, Institute of Microtecbnology, University of Neuchâtel, Switzerland, 1992.

[1.39] M. Hasbimoto, C. Cabuz, K. Minami, M. Esashi, "Silicon resonant angular rate sensor using electromagnetic excitation and capacitive detection", Proceedings of the Micro System Technologies'94, Berlin, Germany, October 1994, pp. 763-771.

[1.40] R. T. Howe, B. E. Boser and A. P. Pisano, "Polysilicon integrated microsystems: technologies and applications", Sensors & Actuators A - Physical, A 56 1996, pp. 167-177.

[1.41] R. A. Buser, "Theoretical and experimental investigations on silicon single crystal resonant structures ", Ph. D. dissertation, University of Neuchâtel, 1989.

[1.42] R. C. Jaeger, J. C. Suhling and R. Ramani, "Errors associated with the design, calibration and application of piezoresistive stress sensors in (100) silicon", IEEE Transactions on Components Packaging and Manufacturing Technology Part B - Advanced Packaging, Vol. 17 N°. 1 1994, pp. 97-107.

[1.43] S. Durand and CR. Tellier, "Linear and non-linear piezoresistance coefficients in cubic semiconductors.1. theoretical formulations", Journal de Physique III, Vol. 6 N°. 2 1996, pp. 237-266.

2. First gyroscope design

2.1 Introduction:

Low cost silicon micromachined gyroscopes (angular rate sensors) are promising devices for automotive (airbag systems, automatic breaking systems) and consumer applications (anti-jitter compensation for video cameras) [2.1].

Several means of excitation and detection have been demonstrated for angular rate sensors. Different types of actuation have been reported piezoelectric [2.1,2.2], electrostatic [2.3, 2.4, 2.5] or electromagnetic [2.6], while for detection piezoelectric [2.1] or capacitive [2.2, 2.3, 2.4, 2.5, 2.6] are usually employed.

In this chapter, a new silicon resonant gyroscope with piezoresistive detection [2.7] and electromagnetic excitation [2.8] is presented. Piezoresistive detection has been chosen because it is the most common sensing principle for silicon based sensors (pressure sensors and accelerometers) [2.7, 2.9]. The fabrication process of this device is also compatible with the industrial one used for pressure sensors and accelerometers, including wafer scale packaging.

The following paragraphs explain the chosen design, then describe the main technical steps of the fabrication and finally give a full characterization of prototype gyroscopes including dynamic, temperature and rotation tests.

2.2 Design:

This new gyroscope is based on the tuning fork principle. It is operated by vibrating two tines in antiphase in one plane. A rotation around one axis which is parallel with the tines will generate a vibration out of this plane due to the Coriolis force. The out of plane deflection of the tines will allow the Coriolis force and thus the rotation around the working axis to be measured. The amplitude of the Coriolis force (F_c) depends on the tines mass (m), the velocity of the antiphase vibration (v) and the speed of the rotation (Ω).

$$F_c = 2 * m * v \times \Omega \qquad [2.6]$$

The design of the resonator has been chosen in order to achieve an optimal trade-off between the mass and the spring constant of the flexures. It can clearly be seen that the amplitude of the Coriolis force is directly proportional to the tines mass.

Thus a dual accelerometers gyroscope has been designed with two seismic masses each supported by a four-beam bridge-type suspension [2.5, 2.7].

When rotating the gyroscope, the out of plane vibration of the proof masses due to the Coriolis force is sensed by means of four p-type piezoresistors centered on top of the external suspensions and connected in a Wheatstone bridge (Figure 2.1). This configuration presents some advantages. As the two seismic masses are driven in antiphase, the variation (ΔR) in the piezoresistors will be always of opposite sign for the two masses. Thus common mode signal like a linear acceleration in the sensing direction will be canceled in the Wheatstone bridge. The piezoresistors centered on the suspension beam on the frame side have been designed as U shapes to cancel the transverse sensitivity of the strain gauges and they should measure only longitudinal stress due to the out of plane motion of the proof masses.

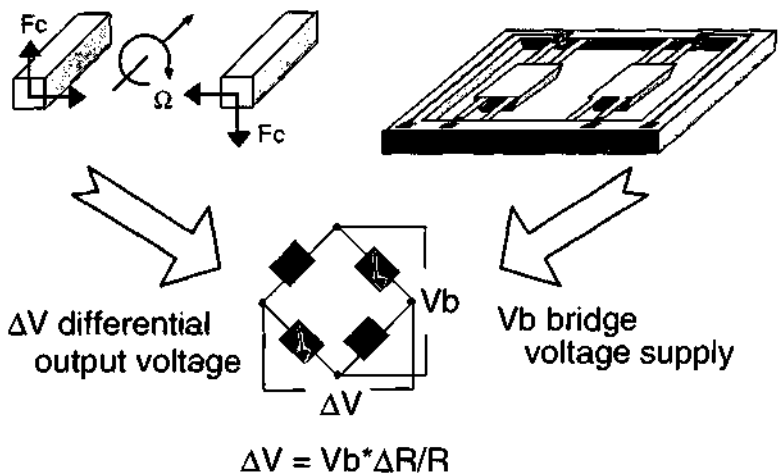

Figure 2.1: schematic of the detection principle: the two tines of the tuning fork design are replaced by two seismic masses suspended by four beams.

Figure 2.2 illustrates the excitation principle of this sensor. When an AC current (I) flows along the metallic conductor (length L) placed on top of the proof masses, the interaction of this current with a perpendicular magnetic induction (B) results in Lorentz forces. The U-shaped design of the excitation current line results in antiphase vibrating forces. Electromagnetic forces have been chosen because on one hand, the driving amplitude is independent from the position of the mass and on the other hand, large excitation amplitude can be obtained with a relatively low driving current (less than 10 mA) [2.6, 2.8]. The permanent magnetic induction is 0.07 Tesla near the reference surface of the AlNiCo magnet .

To test this first prototype gyroscope, 3 different designs have been fabricated (Figure 2.3). Each concept is characterized by the size of the proof masses (M1 design: (0.6*0.6*0.36 mm^3), M2 design: (1*1*0.36 mm^3), M4 design: (2*1*0.36 mm^3)), while the suspension beams are (20*20*500 μm^3).

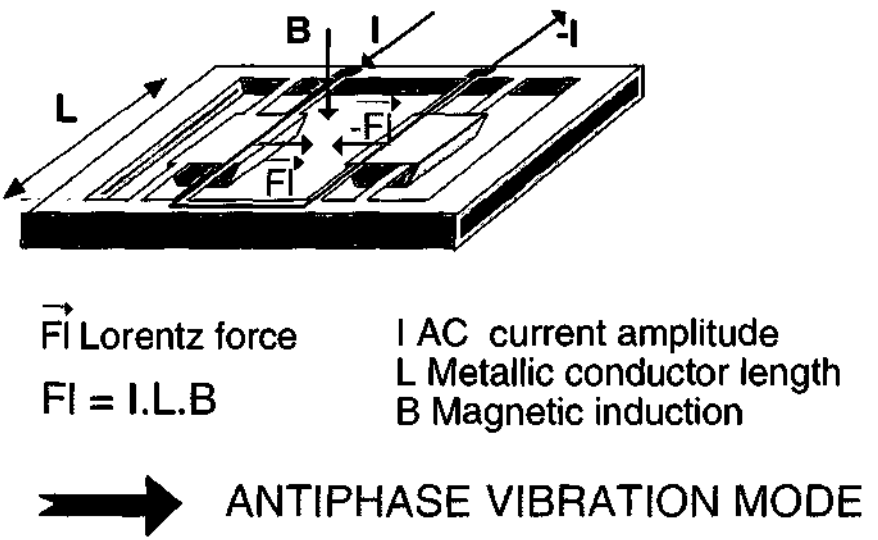

Figure 2.2: schematic of the excitation principle to initiate the antiphase vibration mode.

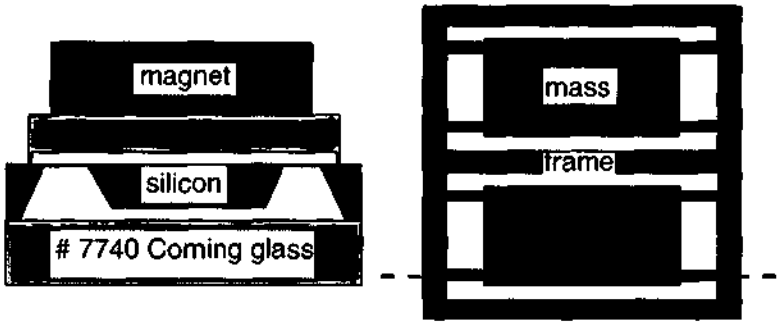

[µm]	length	width	thickness
frame	7000	7000	380
mass	2000/1000/600	1000/1000/600	360
beam	500	20	20

Figure 2.3: drawings of the 3 different designs of the first prototype gyroscope.

2.3 FEM analysis:

The Finite Element Modeling (FEM) analysis is dedicated to the calculation of the resonant frequencies of a vibrating structure (i.e. the proof mass suspended by four beams). The driving mode should be an in plane translation (horizontal direction) and the sensing mode a translation perpendicular to the previous one (vertical motion). For the gyroscope design, we tried to match the first and the second resonant frequencies, with the square cross section of the suspension beams, to benefit in each case from the mechanical amplification and for an efficient energy transfer from the driving mode to the sensing mode. Figure 2.4 illustrates the first 3 resonant frequencies of a gyroscope prototype with the M4 design (proof mass size: 2*1*0.36 mm^3). The sensing and the driving modes are closed due to the quasi square cross section of the beams and the third resonant frequency (rocking mode) is rejected to higher frequencies. On one hand, matching both frequencies is difficult due to the technology and on the other hand, with a perfect matching, the cross coupling between the excitation part and the detection part will be maximum [2.10, 2.11]. These aspects will be discussed later with the resonant frequency measurements.

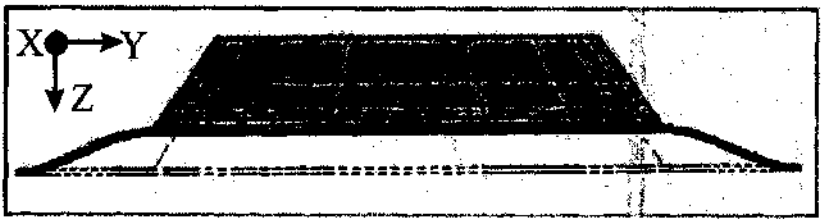

detection mode F=3333Hz

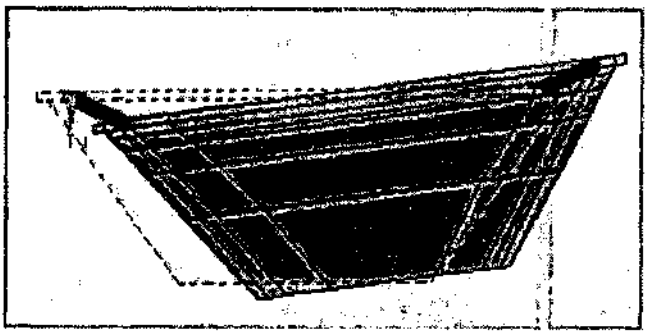

excitation mode F=3466Hz

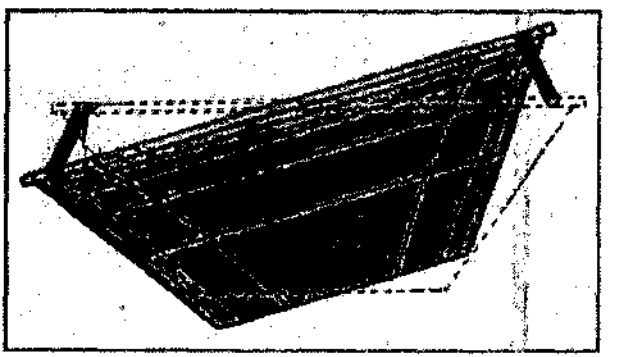

rocking mode F=6843Hz

*Figure 2.4: Mode shapes and resonant frequencies of the first 3 modes of a prototype gyroscope (design M4: (2*1*0.36 mm^3)). The beam thickness is 16.5 µm and its width 18.6 µm. The simulation was performed with the Ansys 5.3™ FEM program.*

2.4 Optical measurements:

Optical measurements have been performed with test structures (vibrating proof masses without the electrical paths) to compare with the previous simulation. A structured wafer was fixed to a vibrating table and both were placed in a vacuum chamber. The laser beam of an interferometer was focused on the center of the seismic mass and the interferometer output was connected to the input of a lock-in amplifier [2.12]. Figure 2.5 shows the vertical displacement of a seismic mass (design M4) versus the excitation frequency.

With the same measurement set-up, we could estimate by changing the pressure in the vacuum chamber, the quality factor of a vibrating mode and its dependency versus the pressure. High quality factor (Q) could enhance the gyroscope performance [2.1, 2.8]. In Figure 2.6, the resonance peak variation versus the pressure is illustrated while Figure 2.7 illustrates the quality factor evolution versus the pressure.

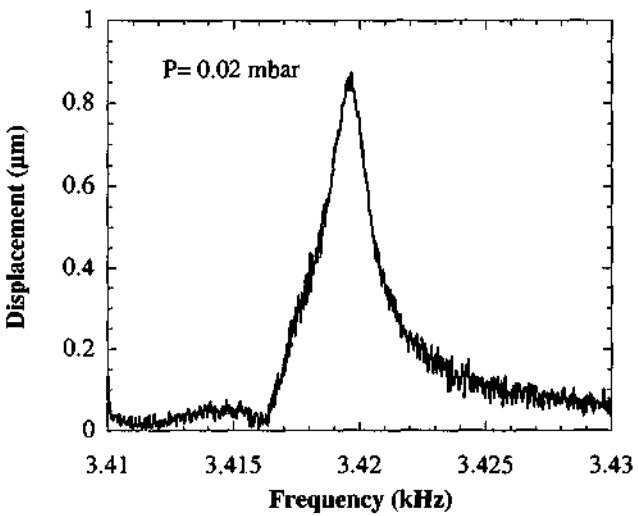

*Figure 2.5: vertical displacement versus excitation frequency for a seismic mass with the M4 design (2*1*0.36 mm^3). The beam width and thickness are respectively 16.8 µm and 16.9 µm. The nitrogen pressure in the vacuum chamber is 0.02 mbar.*

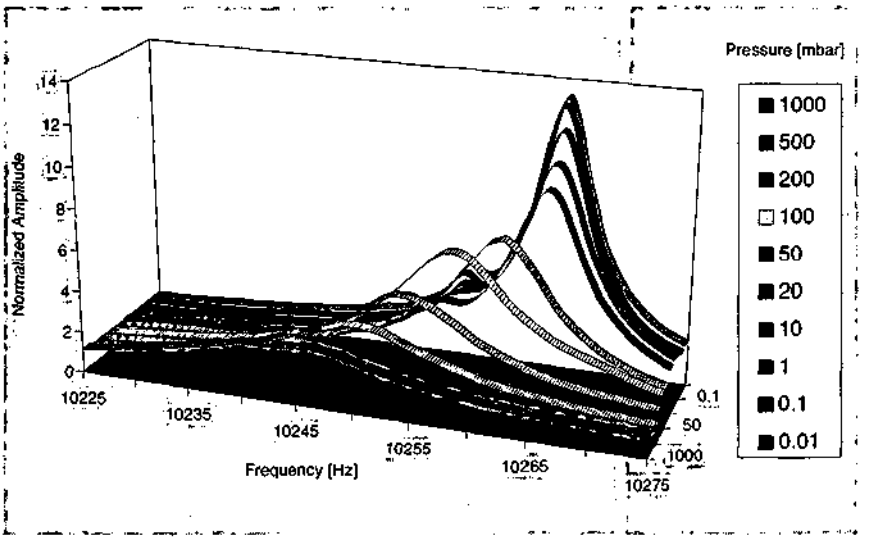

*Figure 2.6: the resonance peak shift versus the pressure for a prototype gyroscope (design M1: 0.6*0.6*0.36 mm^3). The normalized amplitude is calculated with the ratio between the vertical displacement for a given pressure and the vertical displacement at the atmospheric pressure.*

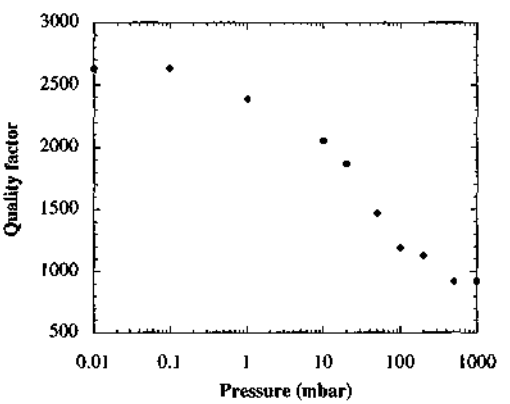

*Figure 2.7: quality factor versus the pressure for a M1 prototype gyroscope (0.6*0.6*0.36 mm^3).*

The quality factor (Q) has been estimated at -3dB. For a pressure of 0.1 mbar, the quality factor is maximum. Lower pressure would not allow higher Q values due to the energy dissipation inside the vibrating structure [2.8].

These preliminary tests underline that the performances of a prototype gyroscope are strongly dependent on the vibrating structure geometry. Thus we have to pay attention to the realization of the prototype gyroscope in particular, of the proof masses and suspension beams.

2.5 Fabrication:

2.5.1 KOH etching:

New developments in the field of micro electro mechanical systems (MEMS) have been essentially determined by the progress made in the micromachining. As batch anisotropic etching of silicon in potassium hydroxide (KOH) allows the structuring of silicon in the third dimension, new devices could be realized [2.8, 2.9, 2.13]. KOH etching of silicon has been required in our process to define the proof mass with an etching depth of 360 µm. Particular attention has to be taken on the definition of the convex corner of the seismic mass. Compensation structure has to be added in the mask layout to avoid the convex corner undercutting. Several designs of compensation structures have been proposed for (100) silicon wafer. The most efficient is the (010) bar, which preserves the convex corner from underetching and leaves the silicon membrane without any roughness [2.7, 2.8, 2.13, 2.14, 2.15, 2.16]. The (010) bar compensation structure takes a huge place in the mask layout and sometimes can not be used due to space consideration. Thus new compensation structures with bars in the (110) direction have been proposed [2.13, 2.17, 2.18, 2.19]. Not only the corner undercutting but also the roughness of the sidewalls and the etched membrane can be an important criteria for some applications[2.19]. Different wet etching solutions (KOH or TMAH/IPA) can also be chosen to obtain wished results [2.20].

For the prototype gyroscope, a (110) compensation structure with an asymmetric T shape has been chosen [2.17]. Figure 2.8 illustrates the T compensation structures. For the smallest mass design M1 (0.6*0.6*0.36 mm^3), a special double T compensation structure has been tested.

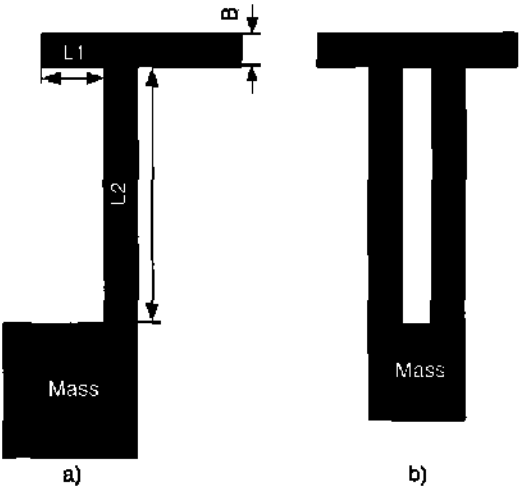

Figure 2.8: schematic of compensation structures in (110) direction for KOH etching of a (100) silicon wafer. a) the asymmetric T compensation structure and b) the double T compensation structure.

The T shape is characterized by 3 dimensions: B, L_1 and L_2. We fixed B at 20 µm and L_1 at 155 µm. The (110) bar width (B) was chosen as thin as possible to avoid large imprints of the compensation structure in the membrane [2.17, 2.18]. L_1 was fixed for the M2 design by a minimum spacing of 90 µm between the two (110) bars of the T compensation for two mass corners on the same side of the seismic mass. Then L_2 is calculated with the following equations:

$$L_{eff} = L_1 + L_2 + 2.83 * B \qquad [2.17]$$

$$L_{eff} = h * 2.7 \qquad [2.17]$$

L_{eff} is the effective length of the T compensation structure and corresponds to the straight moving distance of an etching front along the (110) direction when the compensation structure is completely consumed. As the etching front proceeds along the (110) direction at a rate 2.7 times the vertical rate for a (100) wafer, the equation gives the relationship between L_{eff} and the etching depth (h). Table 2.1 resumes the dimensions for 3 different etch depths of the T compensation structure.

Figure 2.9 shows the etching profile of a T compensation structure designed for an etch depth of 400 µm. In Figure 2.9, on the left side, the T compensation is not yet underetched and the silicon sidewalls are (111) plans but on the right side, the undercutting planes are (411) planes [2.17]. The double T compensation structure has been tested for the M1 design but the latter can not prevent efficiently from the corner undercutting (Figure 2.10). The flat tips between the suspension beams corresponds to the imprints of the T compensation structure in the silicon membrane. Moreover the T compensation structure has been designed for an etching depth of 360 µm and the effective depth was 340 µm. The same flat tips are present for each prototype gyroscope design (M1, M2 & M4) but their mass is negligible versus the seismic mass.

Etch depth (µm)	h	340	360	400
T compensation dimensions (µm)	L1	155	155	155
	L2	706	760	868
	B	20	20	20

Table 2.1: dimensions of the T compensation structure for 3 etch depths.

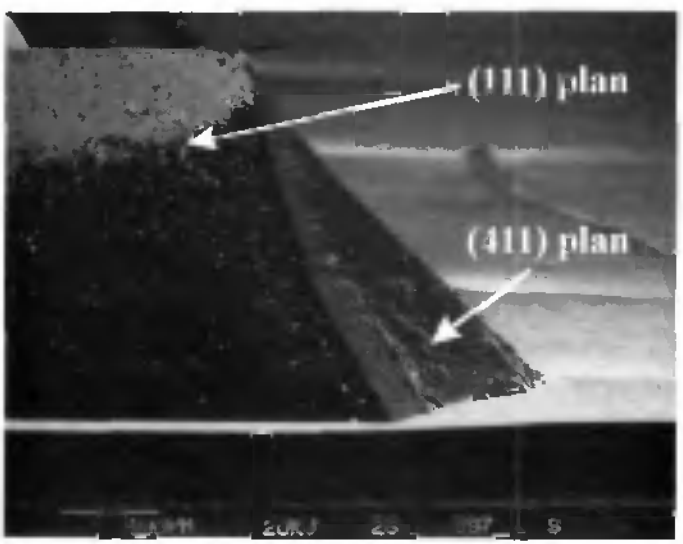

Figure 2.9: SEM picture of the etching profile of a T compensation structure designed for an etch depth of 400 µm. The etching depth is 329 µm.

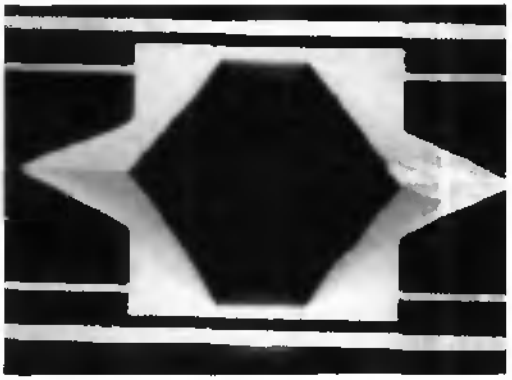

*Figure 2.10: optical view of the back side of a M1 design gyroscope prototype (0,6*0,6*0.36 mm^3) protected with a double T compensation structure during KOH etching.*

For the two other designs (M2 & M4), the T compensation structure was efficient and the seismic mass shape was well defined. The mass and beam definitions are concerning the last steps of the gyroscope process, which is described in details in the next paragraph.

2.5.2 Silicon micromachining:

Double side polished n-type silicon wafers were used for the fabrication of the gyroscopes. The main processing steps are explained in Figure 2.11. The first processing steps concern the top side of the wafer. The four boron doped piezoresistors are implanted. A LPCVD (Low pressure chemical vapor deposition) silicon nitride layer is deposited and patterned. It ensures the electrical insulation and also the masking layer for the subsequent back-side KOH etching. Then a n-type LPCVD polysilicon layer is deposited and defined on the top side. A metallic layer is evaporated and structured to build the excitation line and to connect the piezoresistors together. Then the proof masses are shaped out of the silicon, using a back side KOH etching, while the top side of the wafer is protected with a chuck. Finally the beams are defined by reactive-ion etching (RIE) plasma. This process allows beams with well defined side walls to be fabricated and thus gives control of the mechanical behavior of the proof masses. Table 2.2 resumes the whole process for the first gyroscope design.

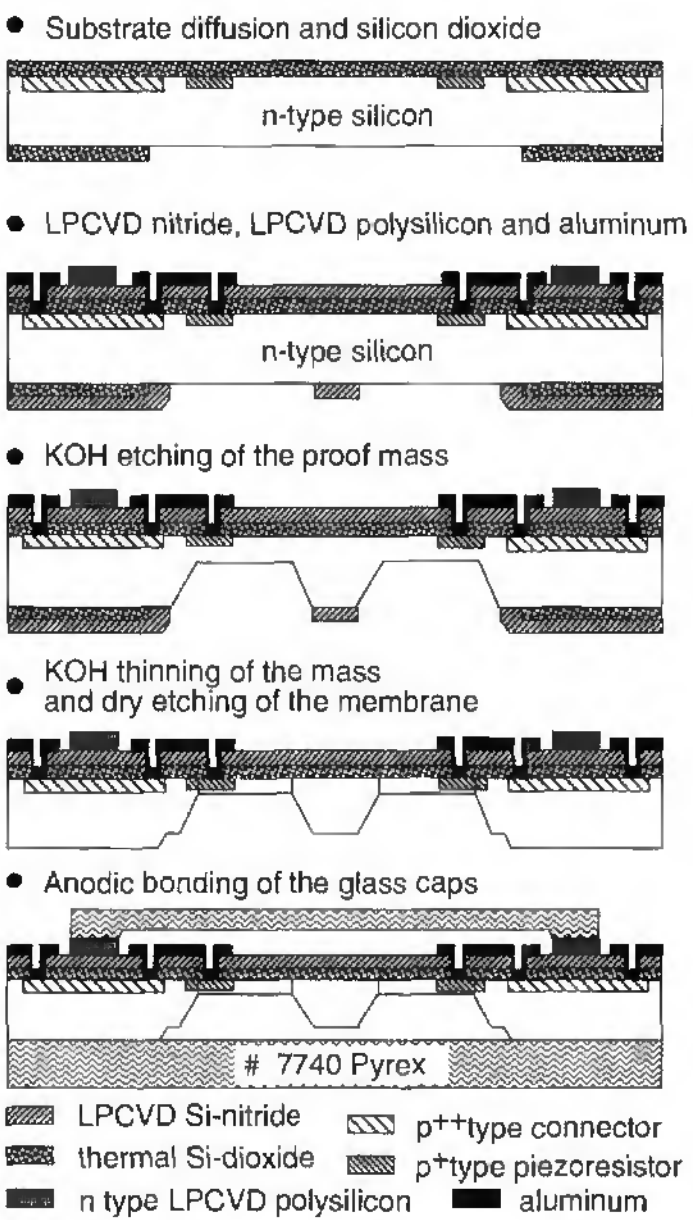

Figure 2.11: process cross sections along the suspension beams and the proof mass in the longitudinal direction for the first prototype gyroscope.

Process Step	Mask / Layer	Thickness
Phosphorus doped 3"		380 µm
double side polished silicon wafers		
Diamond marks		
Standard cleaning		
Positive photolithography (FS)	1: alignment	
Plasma etching	silicon	5000 Å
Resist stripping		
Standard cleaning		
Dry oxidation		1000 Å
Resist spinning for FS protection		
Positive photolithography (BS)	2: space	
BHF [7:1] etching	silicon dioxide	1000 Å
Resist stripping		
Positive photolithography (FS)	3: piezo	
Implantation (boron)		
Resist stripping		
Thermal anneal		
Positive photolithography (FS)	4: connection	
Implantation (boron)		
Resist stripping		
Positive photolithography (FS)	5: substrate	
Implantation (phosphorus)		
Resist stripping		
LPCVD silicon nitride deposition		2000 Å
Positive photolithography (FS)	6: contact	
Plasma etching	silicon nitride	2000 Å
BHF [7:1] etching	silicon dioxide	1000 Å
Resist stripping		
LPCVD polysilicon deposition		5000 Å
CVD oxidation		5000 Å
phosphorus doped		
Thermal anneal		
Thermal anneal		

Process Step	Mask / Layer	Thickness
BHF [7:1] etching	silicon dioxide	5000 Å
Positive photolithography (FS)	7: polysilicon	
Plasma etching on both sides	polysilicon	5000 Å
Resist stripping		
BHF [7:1] etching (FS)		
Metal deposition	aluminum	1 µm
Positive photolithography (FS)	8: aluminum	
Wet etching	aluminum	1 µm
Resist stripping		
Thermal anneal		
Positive photolithography (BS)	9: mass	
Plasma etching	silicon nitride	2000 Å
Resist stripping		
Wet etching	silicon	340 µm
Plasma etching	silicon nitride	2000 Å
Wet etching	silicon	20 µm
BHF [7:1] etching	silicon dioxide	1000 Å
Positive photolithography (FS)	10: beam	
Plasma etching	silicon	20 µm
Resist stripping		
Cleaning for anodic bonding		
Anodic bonding		

Table 2.2: process description for the first prototype gyroscope (first part on the previous page).

Figure 2.12 shows a gyroscope prototype with the M4 design (2*1*0.36 mm^3). A closer view of a suspension beam is presented in Figure 2.13. Details of the seismic mass corner (bottom and top view) are illustrated in Figure 2.14 and in Figure 2.15.

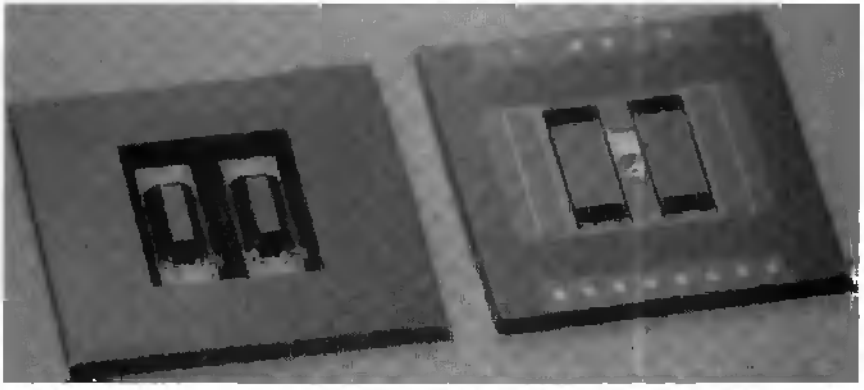

*Figure 2.12: optical view of a prototype gyroscope with from the left to the right, the bottom side and the front side of the silicon chip. The design is M4 with seismic masses of 2*1*0.36 mm^3 and with suspension beams of 0.5*0.02*0.02 mm^3.*

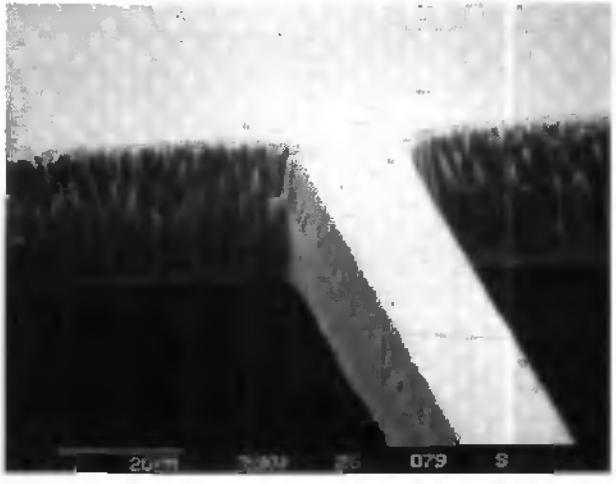

Figure 2.13: SEM picture of a suspension beam. The width is 17 μm and the thickness is 21 μm.

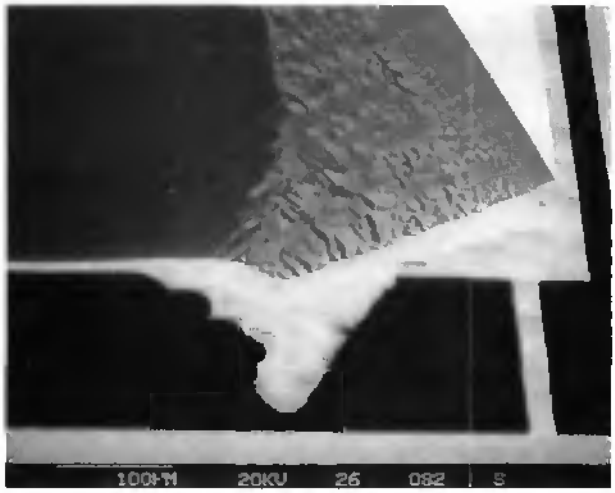

Figure 2.14: SEM picture of the bottom side of a seismic mass corner. The narrow tip in silicon is an imprint of the compensation structure to protect the mass corner. Its size is negligible versus the proof mass size and it will not perturb the further measurements.

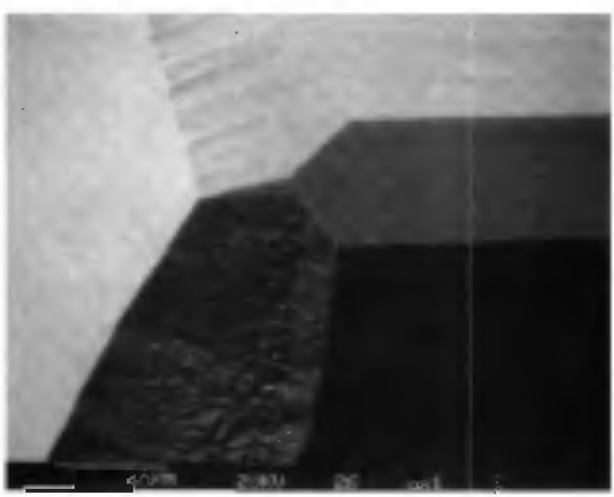

Figure 2.15: SEM picture of the top side of a seismic mass corner. The mass was thinned down of 20 µm for the packaging and the corner was slightly underetched.

2.5.3 Packaging:

Packaging of the prototype gyroscope is an important step because on one hand, it will allow us to handle the silicon chip without damaging the vibrating structures and on the other hand, it can be an efficient protection during the dicing of the chips. Many encapsulation techniques have been reported [2.21]. The anodic bonding has been chosen because it can provide a good overrange protection by the glass micromachining and it required no glue or very high temperature treatment, which can deteriorate the sensor performances. Moreover anodic bonding has been successfully employed for silicon sensor packaging and even high vacuum encapsulation could be realized [2.22, 2.23]. First attempt of anodic bonding was performed chip by chip but the poor yield (less than 20%) convinced us of choosing the wafer scale packaging. This wafer scale packaging consists in an anodic bonding of two 500 µm thick glass wafers (#7740 borosilicate Pyrex).

The top glass wafer is structured, a 20 µm deep cavity is etched [2.24]. The etching depth was fixed to 20 µm because for 14 µm the device would be critically damped at room temperature [2.7]. The bottom glass wafer is not recessed because the proof masses was thinned to insure the same spacing of 20 µm on the bottom side of the cavity. The anodic bonding is performed at 500°C and by applied a negative voltage of 800V on the glass wafer. The bottom glass is directly bonding on silicon but for the top glass a polysilicon frame was designed to ensure a good adhesion of the Pyrex glass to the silicon substrate (Figure 2.12). Figure 2.16 illustrates the top glass masking layout for the 20 µm recessing. For a wafer scale packaging, 20 µm deep tubes have been designed to enable further access to the bonding pads. This tube will be opened by a partial dicing of the top glass wafer before the dicing of the encapsulated chip. After the chips have been diced, they are glued on an IC socket and a permanent magnet is centered and glued on top of them to provide a constant magnetic induction. Vacuum anodic bonding has been performed in a vacuum chamber with a pressure of 0.001 mbar. The vacuum packaged prototype gyroscopes were not further tested due to the bad partial dicing of the top glass. This critical step will be optimized for the second prototype gyroscope. Chapter 3 will give more informations on all these packaging problems including, glass micromachining, anodic bonding and chip dicing.

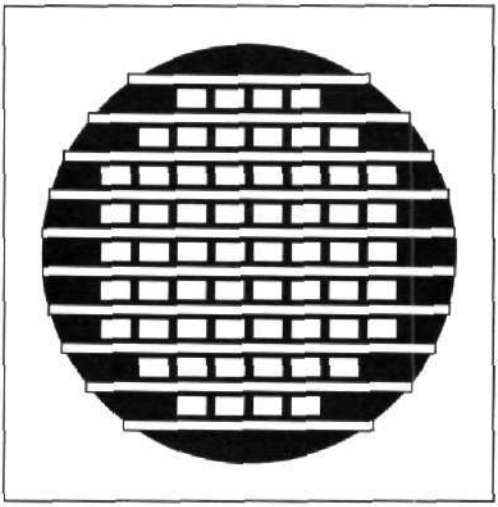

Figure 2.16: mask layout of the top glass wafer for the encapsulation of the first prototype gyroscope.

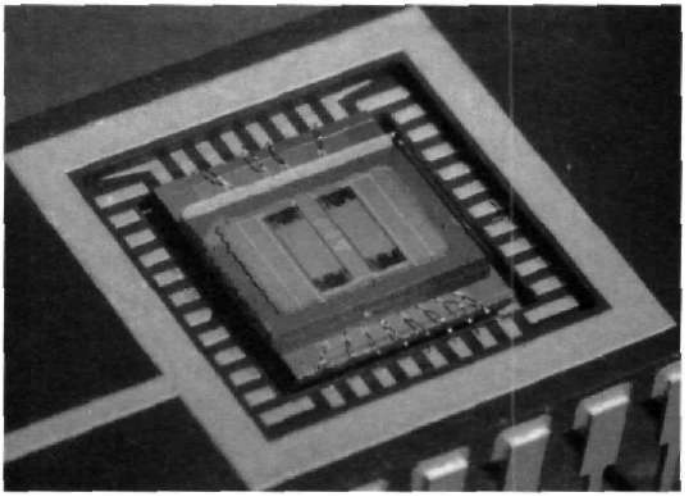

*Figure 2.17: optical picture of a packaged prototype gyroscope before the gluing of a permanent magnet. This is a M4 design with proof masses dimensions of 2*1*0.36 mm^3. The overall size of the chip is 7 mm by 7 mm with a thickness of 1.5 mm.*

To perform the measurements, the top glass cap has to be thinned until 200 µm (whole thickness: 500 µm) to obtain an efficient interaction between the permanent magnet and the AC current flowing though the metallic lines on the silicon chip.

2.6 Characterization:

2.6.1 Resonant frequency characterization:

First, the prototype gyroscopes have been electrically tested without rotation. Figure 2.18 shows the measurement set-up. The excitation circuit is represented by a resistor. Electromagnetic excitation is provided by a constant magnetic induction B of about 0.07 Tesla. A sinusoidal voltage is delivered by the lock-in amplifier which provides the reference for the phase sensitive detection as well as the excitation voltage. The output signal of the Wheatstone bridge is amplified by an instrumentation amplifier INA110 (Burr Brown) and is connected to the lock-in amplifier input. Figure 2.19 and Figure 2.20 illustrate respectively the resonance curves for a M1 design prototype gyroscope and for a M4 design prototype gyroscope.

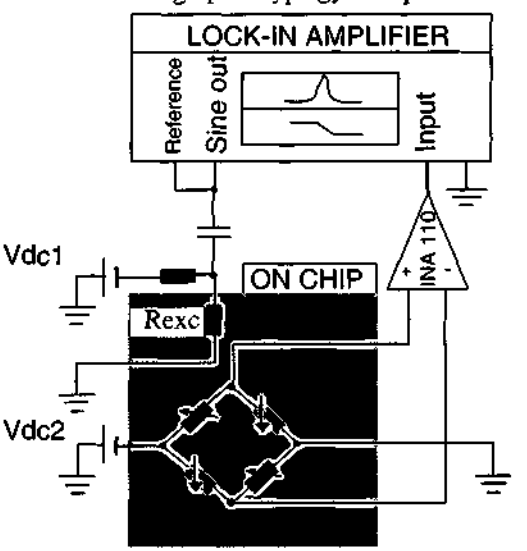

Figure 2.18: measurement set-up for the resonant frequency characterization.

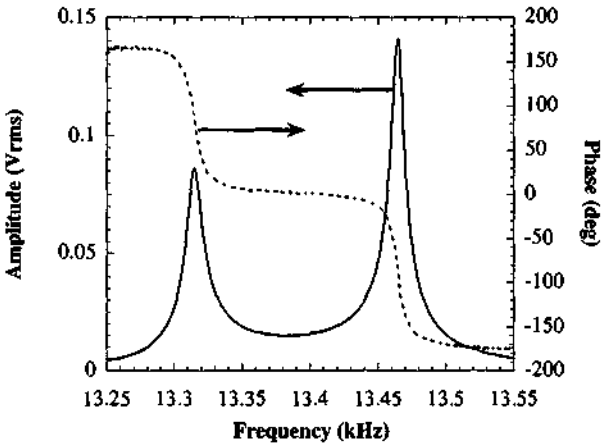

*Figure 2.19: frequency response of a M1 design prototype gyroscope (0.6*0.6*0.36 mm^3). The AC driving current is 1.8 mA, the magnetic induction is 0.07 Tesla and the amplification gain is 500.*

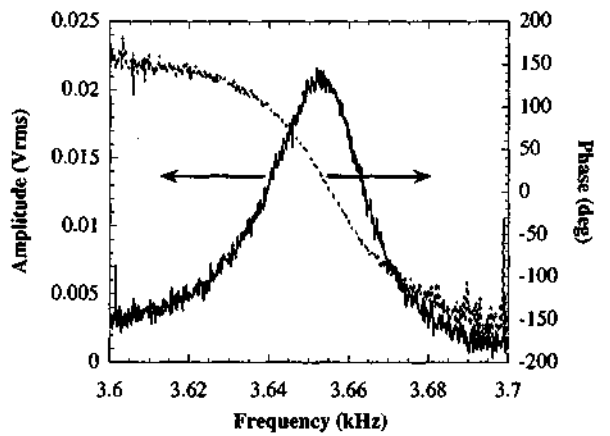

*Figure 2.20: frequency response of a M4 prototype gyroscope (2*1*0.36 mm^3). The AC driving current is 2.7 mA.*

In Figure 2.19, we can observe two resonance peaks. By replacing two piezoresistors of one proof mass by two fixed resistors in the Wheatstone bridge, we can check that each resonance peak corresponds to each seismic mass. For the M1 design, the two proof masses have been underetched during KOH etching (Figure 2.10), thus it was not possible to match perfectly the two resonant frequencies. However, for the M4 design, the superposition of the individual signals gives a single amplitude peak and the phase change corresponds to the addition of the individual signals (360 deg). The KOH corner compensation has been properly defined and thus the shape of each seismic mass is the same, giving the same resonant frequency (Figure 2.12).

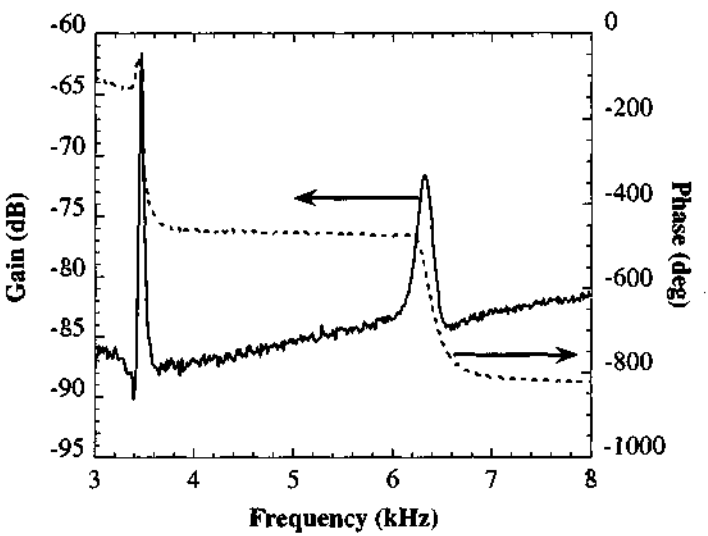

*Figure 2.21: gain-phase diagram of a M4 prototype gyroscope showing the two first rocking modes (2*1*0.36 mm^3).*

This measurements confirm the previous simulated results, where the driving mode was not a perfect in plane movement but a rocking mode (Figure 2.4). With electromagnetic forces, the two proof masses are already moving out of plane without any rotation and this can be sensed by the Wheatstone bridge. The latter doesn't reject all the common motions of the proof masses. The resonance peaks detected by the Wheatstone bridge are not related to the sensing mode (pure vertical translation mode) but to the driving mode (rocking mode). With a M4 design prototype gyroscope, further measurements with a gain-phase analyzer show the next rocking mode about 7 kHz as simulated (Figure 2.21).

These measurements without any rotation point out the drawbacks of the matching of resonance modes (driving and sensing) and some limitation of the Wheatstone bridge detection. Nevertheless, these drawbacks will not prevent us from rotation measurements [2.25]. The angular rate sensor will be tested for a given temperature range and in rotation. The next paragraph will present the main results of the prototype gyroscope versus the temperature.

2.6.2 Temperature measurements:

The temperature have been performed with a M2 design prototype gyroscope (1*1*0.36 mm^3) [2.26]. Temperature dependency of an angular rate sensor is not only concerning silicon sensors. Ceramic gyroscope should also take the temperature dependency in to account [2.27].

The temperature characterization has been realized with the previous measurement set-up (Figure 2.18). But the small circuit board with the angular rate sensor and the differential amplifier was placed in a climate chamber (Heraeus Vötch VMT 04/35). The output signal of the angular rate sensor is amplified and connected to the lock-in amplifier input, which in the same time provides the AC excitation voltage. We performed for a M2 prototype gyroscope the same electrical measurements without rotation for different temperatures. Figure 2.22 shows the resonance curves we obtained. By increasing temperature, the resonance peaks are shifted to higher frequencies and the resonance amplitude becomes smaller. From Figure 2.23, we can draw the variation of the zero-rotation offset versus the temperature. It is decreasing as a parabolic function with temperature.

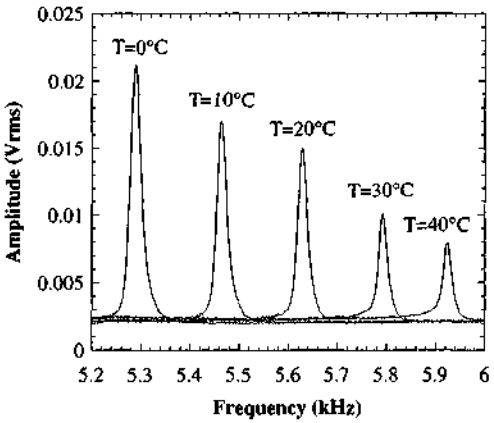

*Figure 2.22: frequency response of a M2 prototype gyroscope versus temperature (1*1*0.36 mm³).*

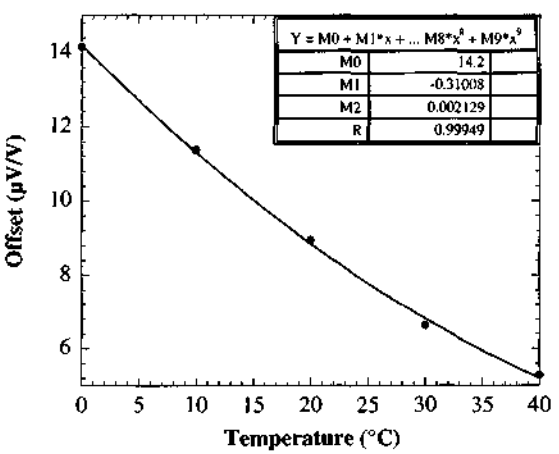

*Figure 2.23: variation of the zero-rotation offset as a function of temperature and the parabolic least-square approximation for a M2 prototype gyroscope (1*1*0.36 mm³).*

The temperature coefficient of offset (TCO) for the M2 prototype gyroscope was 5.25 μV/V/K [2.9]. This temperature dependence is not negligible and can be explained because the temperature coefficients of the piezoresistors are not equal and because stress is introduced by thermal expansion of the different layers which constitute the sensing resonators [2.9]. Moreover, on one hand, the thermal stress in the supporting beams, and on the other hand, the different thermal expansion coefficients of silicon and glass required for the anodic bonding packaging at 500 °C can explain the temperature dependence of the resonant frequency [2.21, 2.22]. From Figure 2.22, we can draw the resonant frequency variation versus the applied temperature. During the electrical measurements, the equivalent resistor of the Wheatstone bridge was calculated from the fixed voltage applied to the Wheatstone bridge and the corresponding DC current. Figure 2.25 illustrates the temperature dependence of the resistor. A temperature coefficient of the resistor (TCR) of 1520 ppm/K at 20 °C was calculated. This value was obtained with a p type impurity concentration of 2 10^{18} at/cm^3 and was higher than the previously reported value [2.9]. It can be partially explain by the fact that the piezoresistors in the Wheatstone bridge are not only sensitive to the temperature but to the stress induced in the suspension beams. These effects can not be separate during the temperature measurements. Moreover, for p type impurity concentration below 10^{19}at/cm^3, π is increasing as well as its temperature sensitivity [2.9].

The temperature coefficient of the sensitivity (TCS) was not investigated because this will require a sophisticated measurement set-up with a rotation table including a temperature chamber. This temperature characterization underlines the importance of the temperature dependency of the prototype gyroscope. For improved performances of this device, a temperature compensation system should be added to the detection electronics.

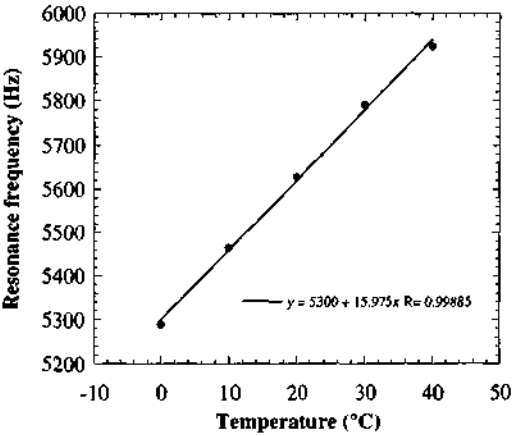

*Figure 2.24: resonant frequency variation versus the applied temperature for a M2 prototype gyroscope (1*1*0.36 mm^3).*

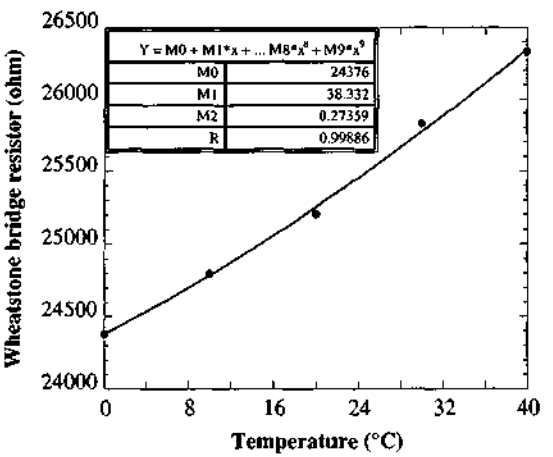

*Figure 2.25: variation of the equivalent resistor of the Wheatstone bridge as a function of temperature for a M2 prototype gyroscope (1*1*0.36 mm^3).*

2.6.3 Rotation measurements:

Three prototype gyroscopes have been subjected to rotation. As shown in Figure 2.26, the board with the encapsulated sensor and amplification circuit has been fixed on a rotating table (ACUTRONIC AG single axis position rate table 120). The experimental set-up is the same that the one used for the resonant frequency (Figure 2.18). By means of rotating contacts, the amplified output signal was fed to the lock-in amplifier and analyzed. Their measured rate responses are shown in Figure 2.27.

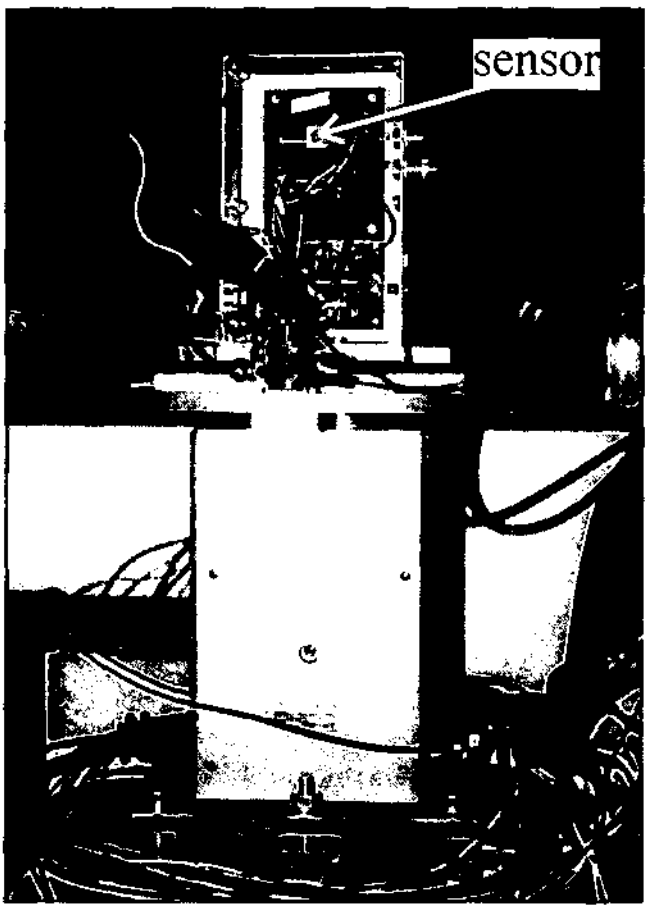

Figure 2.26: picture of the rotating table with a prototype gyroscope fixed on an electronic board. The rotating axis is in the vertical direction.

The three curves presented in Figure 2.27 illustrate that the sensitivity of the sensors increases with the size of the proof masses, which points out the possibility of covering different ranges by an appropriate scaling of the sensor. Moreover, the sign (+ for clockwise and - for counter clockwise) can be detected. It can also clearly be seen that the three prototype gyroscopes show a good linearity. A non-linearity between 0.04 % and 0.19 % has been observed, while a 4 nV/deg/sec sensitivity has been obtained with the M4 design ($2*1*0.36\ mm^3$). These measurements have been performed by subtracting the zero rate output (ZRO) after each measurement due to the ZRO drift. The time constant of the lock-in amplifier was fixed at 3s, which corresponds to a bandwidth of less than 1 Hz. With these parameters, a resolution of 20 deg/sec was achieved with the M2 ($1*1*0.36\ mm^3$) prototype gyroscope.

To perform the rotating measurements, we should apply not only an AC current but also a DC current. This bias current should stabilize the vibrating structures by reducing the misalignment between the driving force and the center of inertia. For each prototype gyroscope a bias voltage of 5V was applied at the driving port. Moreover, the angular rate measurements can not be performed at the resonant frequency but 100 Hz before because as already mentioned, this resonance peak corresponds to the driving mode and not to the sensing mode and shadows the rotating signal when the sensor is driven at this resonant frequency.

Nevertheless, the sensitivity of a prototype gyroscope should be also proportional to the velocity of excitation v:

$$v = \omega * X_{max} \qquad [2.4]$$

with ω the driving angular frequency and X_{max} the peak amplitude of vibration [2.4]. The Lorentz force excitation X_{max} should be linearly dependent of the AC driving current for a given vibrating structure and a constant magnetic induction. A M2 prototype gyroscope has been tested with different AC excitation currents for a fixed angular rate of 200 deg/sec. This feature is shown in Figure 2.28 and as expected the sensitivity is higher for larger AC excitation currents.

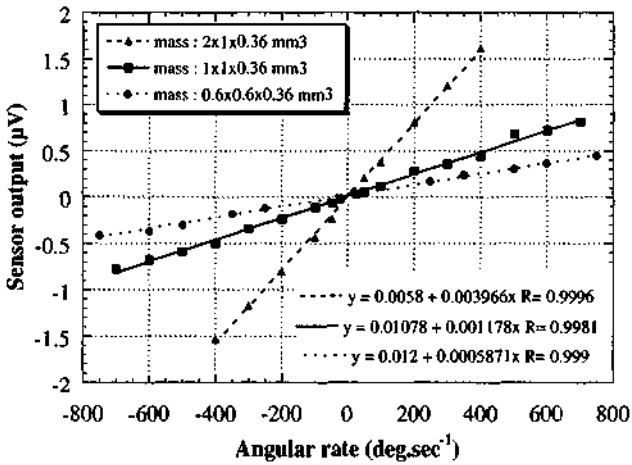

Figure 2.27: the output signal of 3 prototype gyroscopes (M1, M2 & M4 design) at different angular rates.

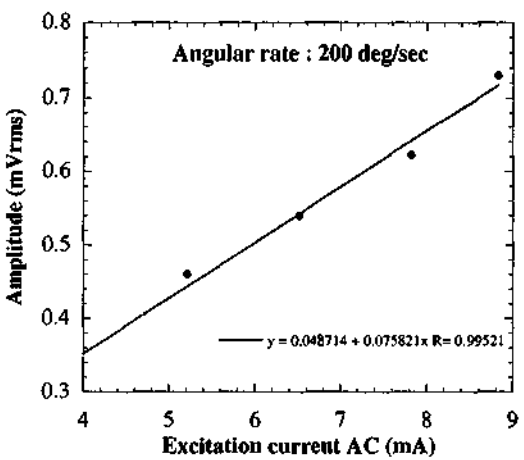

*Figure 2.28: variation of the output voltage as a function of the AC driving current for a M2 prototype gyroscope (1*1*0.36 mm^3).*

2.6.4 Long term measurements:

Long term measurements have been performed with a M4 prototype gyroscope to estimate its output drift. The sensor output voltage is fed to the lock-in amplifier and then to a digital signal processing (DSP) card using a 16 bits analog-to-digital (A/D) converter [2.28]. As shown in Figure 2.29, the sensor output of a M4 prototype gyroscope is recorded during 35 minutes. In the middle of the experiment, the angular velocity is changed from 0 deg/sec to 100 deg/sec. This signal exhibits a large offset drift. After an appropriate correction by Kalman filtering, the high frequency noise is attenuated and the DC drift is removed [2.28]. However a low-pass effect appears when the signal is suddenly changed. Thus, a trade-off has to be found between the drift attenuation and the filtering of the output signal. For more details, please refer to the Ph. D. Thesis of Ms. C. Marselli, which will be published later this year [2.29].

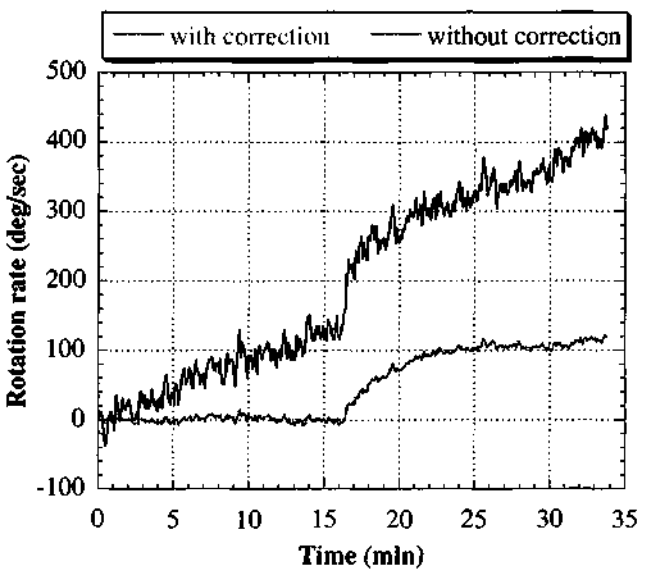

*Figure 2.29: Output drift for a M4 (2*1*0.36 mm^3) prototype gyroscope and its correction by Kalman filtering [2.29].*

2.7 Conclusion:

Several prototype gyroscopes with electromagnetic excitation and piezoresistive detection have been successfully tested under rotation. As expected, the sensitivity of the angular rate sensor is depending from the proof mass size and from the AC driving current. A maximum sensitivity of 4 nV/deg/sec has been obtained with the largest gyroscope prototype with a bandwidth of less than 1 Hz and a resolution of 20 deg.sec^{-1} has been measured.

Temperature measurements have been performed to characterize the variation of the sensor output versus the temperature. The prototype gyroscopes should be compensated in temperature for further industrial applications.

The resonant frequency of the driving mode can not be used to enhance the excitation amplitude because the latter induced a parasitic signal at the device output. A second prototype gyroscope, which will be presented in a next chapter, will try to overcome the previous disadvantages of this first gyroscope design.

2.8 References:

[2.1] J. Söderkvist, "Micromachined Gyroscopes", Tech. Dig. Transducers '93, Yokohama, Japan (1993), pp. 638-641.

[2.2] K. Maenaka, "Analysis and design concept of highly sensitive silicon gyroscope", Tech. Dig. Transducers '95, Stockholm, Sweden (1995), pp. 612-615.

[2.3] P. Greiff, "Silicon monolithic gyroscope", Tech. Dig. Transducers '91, San Francisco, California (1991), pp. 966-968.

[2.4] J. Bernstein, "A micromachined comb-drive tuning fork rate gyroscope", Proc. IEEE MEMS Workshop '93, Fort Lauderdale, Florida (1993), pp. 143-148.

[2.5] M. W. Putty, "A micromachined vibrating ring gyroscope", Proc. IEEE Solid State Sensor and Actuator Workshop '94, Hilton Head, South Carolina (1994), pp. 213-220.

[2.6] M. Hashimoto, "Silicon resonant angular rate sensor using electromagnetic excitation and capacitive detection", Proc. Micro System Technologies '94, Berlin, Germany (1994), pp. 763-771.

[2.7] T. Tschan, "Simulation, design and characterization of a silicon piezoresistive accelerometer, fabricated by a bipolar-compatible industrial process", Ph. D. dissertation, Institute of Microtechnology, University of Neuchâtel, Switzerland, 1992.

[2.8] R.-A. Buser, "Theoretical and experimental investigations on silicon single crystal resonant structures", Ph. D. dissertation, Institute of Microtechnology, University of Neuchâtel, Switzerland, 1989.

[2.9] B. Kloeck, "Design, fabrication and characterization of piezoresistive pressure sensor, including the study of electrochemical etch-stop", Ph. D. dissertation, Institute of Microtechnology, University of Neuchâtel, Switzerland, 1989.

[2.10] J. S. Burdess, A. Harris, D. Wood, J. Cruickshank and G. Cooper, "The microdynamic gyroscope", Technical Digest of The 4th Workshop on Micromachining, Micromechanics and Microsystems, MME '93, Neuchâtel, Switzerland, September 1993, pp. 219-222.

[2.11] Y. Ansel, B. Romanowicz, Ph Lerch and Ph. Renaud, "Optimisation of a vibrating gyroscope by a system level simulation", Proceedings of the 10th European Conference on Solide-State Transducers, Eurosensor X, Leuven, Belgium, September 1996, pp. 1245-1248.

[2.12] F. Lärmer, A. Schilp, K. Funk and C. Burrer, "Experimental characterization of dynamic micromechanical transducers", Journal of Micromechanics and Microengineering, Vol. 6 1996, pp. 177-186.

[2.13] H. Sandmaier, H. L. Offereins, K. Kühl and W. Lang, "Corner compensation techniques in anisotropic etching of (100) silicon using aqueous KOH", Digest of Technical Papers of the 6th International Conference on Solid-State Sensors and Actuators, Transducers '91, San Francisco, CA, June 1991, pp. 456-459.

[2.14] B. Puers and W. Sansen, "Compensation structures for convex corner micromachining in silicon", Sensors & Actuators A - Physical, A 21-23 1990, pp. 1036-1041.

[2.15] H. L. Offereins, K. Kühl and H. Sandmaier, "Method for the fabrication of convex corners in anisotropic etching of (100) silicon in aqueous KOH", Sensors & Actuators A - Physical, A 25-27 1991, pp. 9-13.

[2.16] H. L. Offereins, H. Sandmaier, K. Kühl and W. Lang, "Compensation of convex corners in aqueous KOH-etching", Microsystem Technologies, 1991, pp. 332-337.

[2.17] M. Bao, Chr. Burrer, J. Esteve, J. Bausells and S. Marco, "Etching front control of <110> strips for corner compensation", Sensors & Actuators A - Physical, A 37-38 1993, pp. 727-732.

[2.18] R. P. van Kampen and R. F. Wolffenbuttel, "Effects of <110>-oriented corner compensation structures on membrane quality and convex corner integrity in (100)-silicon using aqueous KOH", Journal of Micromechanics & Microengineering, Vol. 5 1995, pp. 91-94.

[2.19] T. A. Kwa, P. J. French and R. F. Wolffenbuttel, "Anisotropically etched silicon mirrors for optical sensor applications", Journal of the Electrochemical Society, Vol. 142 N°4 1995, pp. 1226-1232.

[2.20] A. Merlos, M. Acero, M. H. Bao, J. Bausells and J. Esteve, "TMAH/IPA anisotropic etching characteristics", Sensors & Actuators A - Physical, A 37-38 1993, pp. 737-743.

[2.21] W.-H. Ko, " Bonding techniques for microsensors", Micromachining and micropackaging of transducers, Elsevier, Amsterdam,The Netherlands (1985), pp. 41-61.

[2.22] C. Cabuz, " fabrication and packaging of a resonant infrared sensor integrated in silicon", Sensors and Actuators A, Vol. 43 (1994), pp. 92-99.

[2.23] H. Henmi, S. Shoji, Y. Shoji, K. Yoshimi and M. Esashi, "Vacuum Packaging for Microsensors by Glass-Silicon Anodic Bonding", Sensors & Actuators, A43 (1994), pp. 243-248.

[2.24] M.-A Grétillat, F. Paoletti, P. Thiébaud, S. Roth, M. Koudelka-Hep and N.F. de Rooij, "A New Fabrication Method for Borosilicate Glass Capillary Tubes with Lateral Inlets and Outlets", Sensors & Actuators, A 60 (1997), pp. 219-222.

[2.25] F. Paoletti, M.-A. Grétillat and N. F de Rooij, "A Silicon Micromachined Vibrating Gyroscope with Piezoresistive Detection and Electromagnetic Excitation", Proceedings of the 9th IEEE Workshop on Micro Electro Mechanical Systems, MEMS '96, San Diego, CA, February 1996, pp. 162-167.

[2.26] F. Paoletti, M.-A. Grétillat and N. F de Rooij, "A Silicon Micromachined Tuning Fork Gyroscope", Proceedings of Symposium Gyro Technology 1996, Stuttgart, Germany, September 1996, pp. 5.0-5.8.

[2.27] H. Abe, T. Yoshida, H. Kobayashi and K. Nakamura, "Temperature dependence of zero offset of piezoelectric-ceramic cylinder vibratory gyroscope", Japanese Journal of Applied Physics Part 1-Regular Papers Short Notes & Review Papers, Vol. 35 N°. 5B, pp. 5031-5033.

[2.28] C. Marselli, H.P. Amann, F. Pellandini, F. Paoletti, M.-A. Grétillat and N. F de Rooij, "Error Modelling of a Silicon Angular Rate Sensor", Proceedings of Symposium Gyro Technology 1997, Stuttgart, Germany, September 1997, pp. 4.0-4.9.

[2.29] C. Marselli, "Data processing of a navigation system", Ph. D. dissertation, Institute of Microtechnology, University of Neuchâtel, Switzerland, to be published.

3. Packaging of microsensors

3.1 Introduction:

Packaging of microsensors refers to the first-level packaging, i.e., enough encapsulation to permit device handling, performance evaluation and actual use in at least some applications [3.1]. As the microsensor technology is issued from the Integrated Circuit (IC) one, the IC packaging can also be used. But the microsystems encapsulation can not provide only moisture and mechanical protections, it has to let the microsensor interacting with the environment in which it is placed [3.2]. Thus the packaging is an essential part of the microsensor and should be designed at the same time. For commercial applications, the packaging becomes the critical point because many applications are dedicated to aggressive media [3.3]. Finally the commercial impact of the packaging is not negligible and is for many sensors the most costly part of their construction. On one hand, the encapsulation can not always take advantage of the batch fabrication and on the other hand, carefully calibration is still necessary after the packaging.

This introduction will underline some of the factors influencing the package reliability and referred different encapsulation technologies. The material for the package has to be chosen very carefully. Plastic caps are cheap, mold in batch but can induce high residual stress in the sensor because their mechanical properties are different from the sensor one. Moreover, residual stress is one of the main cause of instability and drift in sensor packages. The temperature of packaging can also drastically influence the residual stress and has to be chosen as low as possible. Finally the permeability and the chemical stability are two main aspects for the long term stability of the packaged sensor [3.2]. Packaging can be even useful during the fabrication of the sensor by providing an efficient protection during sawing of the chips. Particles generated during the dicing are known to cause defects and to reduce the yield. Thus the choice of a chip by chip or a wafer level packaging has to be carefully considered. Several materials (metal, epoxy, glass, silicon...) can be required

for the encapsulation and thus several techniques of bonding can be employed [3.4, 3.5, 3.6]. W. H. Ko reported in 1985 eleven assembling methods for micromachined devices [3.4]. The gluing, the low temperature glass bonding, the eutectic bonding, the fusion bonding and the anodic bonding are some of them. These sealing methods get different characteristics like the substrates involved, the need of an intermediate layer, the temperature, the applied voltage, the applied pressure and the patterning of the bonding area [3.5]. These parameters have to be controlled because the permeability, the stability and the quality of the package will directly rely on them. Furthermore clean room conditions are almost always required to avoid dust contamination during this step [3.6]. Choosing one of these encapsulation techniques depend on the type of micro device, the influence on its performances, the cost and the equipment required.

For the micromachined gyroscope, the packaging should fulfill the following requirements. First, it should provide an overrange protection for the proof masses and a controlled gap for the damping. It was already the case for some micromachined accelerometers [3.7, 3.8, 3.9, 3.10]. Then it should be the intermediate layer between the silicon chip and the permanent magnet. This induces a controlled thickness of the cap and the centering of the magnet versus the seismic masses for a better efficiency [3.11]. Finally, wafer scale packaging should be possible to protect the vibrating structures during the sawing. Two materials can be chosen silicon or glass but for an easier alignment with the silicon sensor, glass will be preferred. To avoid the dust contamination and the sticking of the proof mass, no glue will be used. Thus anodic bonding will be preferred because it answers all the demands and can give some advantages like a vacuum sealing and a stress control [3.12].

In this chapter, some aspects of the package influence on the sensor performances [3.13], the glass micromachining [3.14, 3.15, 3.16, 3.17, 3.18, 3.19, 3.20, 3.21, 3.22, 3.23, 3.24, 3.25, 3.26], the anodic bonding [3.27, 3.28, 3.29, 3.30, 3.31, 3.32, 3.33, 3.34, 3.35, 3.36, 3.37, 3.38, 3.39, 3.40, 3.41] and the electrical leadthrough as well as the dicing [3.10, 3.20] will be presented.

3.2 Packaging influence:

3.2.1 Introduction:

Micromechanical gyroscope packaging has to be carefully controlled due to the sensor package parasites. But earlier gyroscopes sensors also required thermal control and vibration isolation [3.13]. The encapsulation influence on the sensor performances is well known in the gyroscope domain but the scaling down of the sensor increases this phenomenon. Two kinds of encapsulation can be performed for the angular rate sensor, rather the packaging of the sensor chip or of the sensor chip and the integrated electronic. In this thesis both options will be realized. The simplest one for the first prototype gyroscope (chapter 2) and the other one for the second prototype gyroscope (chapter 4). One particular point is the magnet integration in the device. Thermal and vibration aspects are not specific to gyroscopes, pressure sensors and accelerometers are also concerned [3.27, 3.32, 3.34, 3.36, 3.40]. But the choice of electromagnetic forces for the gyroscope design requires a particular attention for the permanent magnet handling.

3.2.2 Magnet position:

Permanent magnets have been used because they can be scaled to the sensor chip size (less than 1 cm^3), they are inexpensive and they can provide relatively high flux density (magnetic induction). Two kinds of magnet have been tested, the first one (chapter 2) an AlNiCo type providing 0.075 Tesla near the pole face and the second one (chapter 4) a rare-earths and cobalt type providing 0.3 Tesla near the pole surface (trade name Vacomax 225HR). Both magnets exhibit a cylindrical shape with a 5mm diameter and a height between 2 (Vacomax 225HR) and 10 (AlNiCo) millimeters. They are polarized along the symmetric axis of the cylinder and perpendicular to the pole face. Electromagnetic (Lorentz) forces are drastically influenced by the permanent magnet position. On one hand, the magnetic induction is decreasing with the square of the distance along the symmetry axis and on the other hand, the direction and the intensity of the magnetic induction is modifying outside the direction of the symmetric axis.

Figure 3.1 illustrates the principle of the packaging for the first prototype gyroscopes (chapter 2). The silicon resonant structure is encapsulated between a

top glass cap and a bottom glass cap. The sealed chip is fixed on an IC socket and wire bonded for electrical connections. The permanent magnet is glued on the top face of the upper glass.

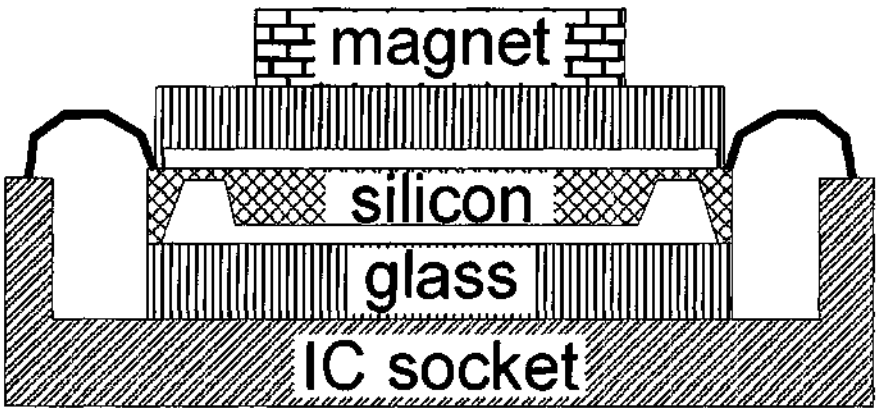

Figure 3.1: schematic of the encapsulated gyroscope prototype (chapter 3).

First prototype gyroscope chips have been tested before gluing of the magnet to show its handling importance [3.42]. To perform the measurements, the output of the sensing Wheatstone bridge was fed to a differential amplifier (INA110 Burr Brown) and then to the input of a lock-in amplifier (Stanford Research SR 850) (figure 2.18). The sine wave output of the lock-in amplifier gives the AC voltage for the driving Lorentz forces and also the internal reference of the lock-in amplifier. Figure 3.2 illustrates the influence of the lateral positioning of the permanent magnet versus the vibrating structures. From the top view, the magnet was moved on the surface of the top glass cap from the right hand side to the left hand side. For each case, a sweep in frequency was done to visualize the change in the resonance peaks (amplitude and resonant frequency) of the two proof masses. The vertical position of the permanent magnet has been also tested by placing a spacer with a control thickness between the top glass cap and the pole face of the magnet (Figure 3.3).

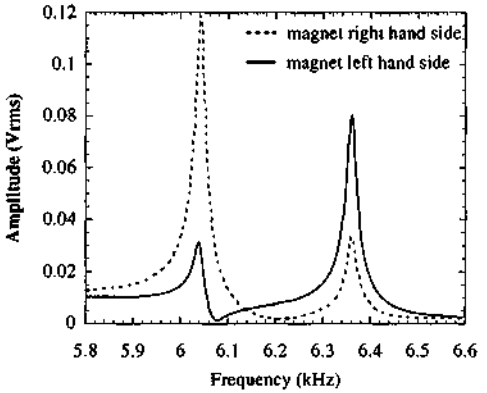

Figure 3.2: the resonance peaks shift due to the lateral position of the permanent magnet. The magnetic induction is 0.25 Tesla, the driving AC voltage is 0.5 Vrms and the amplification gain is 100. The proof mass is 1000 μm long, 1000 μm wide and 360 μm thick.

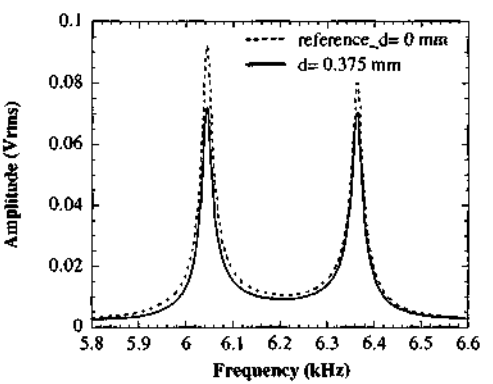

Figure 3.3: the resonance peaks amplitude is decreasing with the increasing distance between the proof masses and the magnet (without spacer d=0 mm and with a spacer d=0.375 mm). The magnetic induction is 0.25 Tesla, the driving AC voltage is 0.5 Vrms and the amplification gain is 100. The proof mass is 1000 μm long, 1000 μm wide and 360 μm thick.

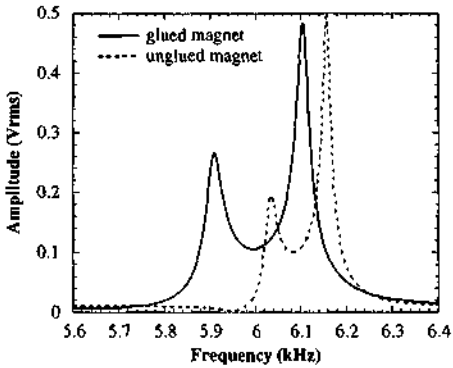

Figure 3.4: the resonance peaks shift due to the permanent magnet fixing on the top glass cap. The magnetic induction is 0.25 Tesla, the driving AC voltage is 0.5 Vrms and the amplification gain is 500. The proof mass is 1000 µm long, 1000 µm wide and 360 µm thick.

The magnet handling in the horizontal and vertical directions can influence the gyroscope output, thus the packaging should integrate the magnet centering and the thinning of the top glass for a better efficiency of the Lorentz force driving. Finally for the rotation rate measurements, the magnet has to be fixed to the package. Figure 3.4 shows the resonance peaks shift induces by compressive residual stress in the encapsulated sensor chip after the gluing of the magnet [3.9].

3.2.3 Conclusion:

Packaging of a micromachined gyroscope has to be undertaken carefully. In particular, for electromagnetic force driving, the handling of the permanent magnet is important. Residual stress induced by the package required at least a dynamic calibration of the sensor due to the resonance peak shift. Stress can result from the difference in the mechanical and thermal properties of the materials involved in the fabrication process, the anodic bonding and the gluing with other materials [3.22, 3.27, 3.30, 3.32, 3.34, 3.36, 3.37, 3.40, 3.41].

This paragraph explains the importance of the packaging for the microsensors and underlines some specific aspects of the microgyroscope encapsulation. The technique of the packaging will be exposed in two steps, the micromachining of glass for the resonant structures and the anodic bonding.

3.3 Glass micromachining

3.3.1 Introduction:

Glass is extensively used in the microsystems technology thanks to its numerous qualities [3.25]. It can be microstructured in any direction because of its amorphous structure, it is transparent in the visible wavelength bandwidth, it has a good chemical stability and a high electrical resistivity. Two different glasses can be distinguished: the borosilicate type (trade name Pyrex) and the photosensitive type (trade name Foturan) [3.14, 3.15, 3.25]. As the latter one is not suitable for anodic bonding, it will not be selected.

Pyrex can be patterned with several techniques like the drilling and the wet etching [3.9, 3.17, 3.20, 3.21, 3.23, 3.24, 3.30]. Drilling holes in glass substrates are dedicated to the microfluidic system to achieve a fluid flow through well defined holes [3.21, 3.23] or to the electrical feedthrough of a packaged microsensor [3.17, 3.30]. Wet etching is preferred for the micromachining of shallow cavities to protect vibrating microstructures [3.9, 3.20, 3.30]. In both cases, several drawbacks have to be underlined. Drilled holes by ultrasonic drilling, sand blasting and laser machining have to be chemically smoothed and for the latter polishing of the substrate surface is necessary before the anodic bonding [3.21, 3.23]. Wet etching of borosilicate glass can be realized with many different fluoride solutions, from concentrate hydrofluoric acid (HF) to buffered solutions of hydrofluoric acid (BHF) with ammonium fluoride (NH_4F). A compromise has to be observed between the etching rate and the undercutting ratio [3.17].

With a higher NH_4F concentration, the etching rate gets smaller and the undercut rate larger. Moreover due to the masking layer, photoresist [3.20] or metal (Cr-Au) [3.9, 3.17, 3.30], the etching depth is limited because, on one hand, the photoresist peels off soon when it is immersed in the concentrate HF solution and on the other hand, the Cr-Au masking layer gets rapidly porous due to pin-holes defaults [3.17].

The latter has been tested for the first prototype gyroscope encapsulation (chapter 2) to recess 20 µm deep cavities in a 7740 Pyrex glass wafer. After the removing of the Cr-Au (500 Å Cr / 5000 Å Au) mask the protected area is filled with pin-holes, which reduces the bonding area (Figure 3.5). The micromachining of glass for the encapsulation of microgyroscopes should at the same time, protect efficiently the bonded area for vacuum packaging and allow deep etching of glass for the magnet handling (§3.1 and §3.2). Thus a new masking material has been investigated to enable the etching of a glass wafer deeply on one side with the other side still suitable for the anodic bonding.

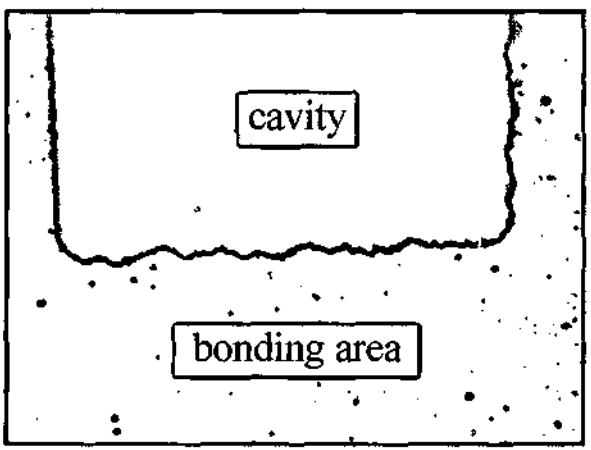

Figure 3.5: Optical picture of the bonding area of a 7740 Pyrex glass chip with a 20 µm deep cavity. The bonding area contains a lot of pin-holes (black points).

3.3.2 Technology:

To combine the deep etching of glass with a perfect area for the anodic bonding, a Low Pressure Chemical Deposition (LPCVD) polysilicon mask is proposed. It has been already used for the micromachining of synthetic quartz (fused silica) substrates [3.43, 3.44]. Due to the lower softening point of the glass versus the quartz this masking material was not considered at first, because the bending of the glass wafer can be induced by the high temperature during the polysilicon deposition and the glass wafer will not be anymore suitable for the anodic bonding. But by choosing an appropriate deposition temperature [3.20] and with the relatively high softening point of the 7740 Pyrex glass also called hard glass [3.14], polysilicon layers have been successfully deposited without damaging the flatness of the glass substrates.

To illustrate the advantages of the polysilicon mask for the micromachining of borosilicate glasses, capillary tubes with lateral inlets and outlets have been fabricated [3.45, 3.46, 3.47, 3.48]. Several microtubes with widths from 340 to 940 µm have been realized as well as different section shapes, which can be circular, elliptic or quasi-rectangular. The main fabrication steps and SEM characterizations are reported [3.24]. The capillary tubes are realized by the assembly of three structured glass wafers (500 µm thick). Figure 3.6 shows an exploded cross-section of the capillary tubes, where the middle glass wafer is patterned on both sides while the two others are only structured on one side.

The micromachining of the different glass wafers has been performed in 50% HF at ambient temperature with an LPCVD polysilicon mask (5000 Å thick). As the glass wafers are held vertically in the furnace, a LPCVD polysilicon layer is deposited on both sides. A standard photolithography followed by a reactive ion etching (RIE) plasma allows to pattern the LPCVD polysilicon mask. The fabrication of the capillary tubes consists in two different levels: first the structuring and second the assembly of the glass wafers. The glass micromachining begins with the fabrication of the access holes (2^{nd} & 3^{rd} glass wafers). A partial etching is performed in 50% HF to obtain 350 µm deep grooves. Then the process continues with the definition of the capillary tubes (1^{st} & 2^{nd} glass wafers). The final size of the access holes (420 µm) is obtained while 170 µm deep capillary tubes are etched in the glass wafers.

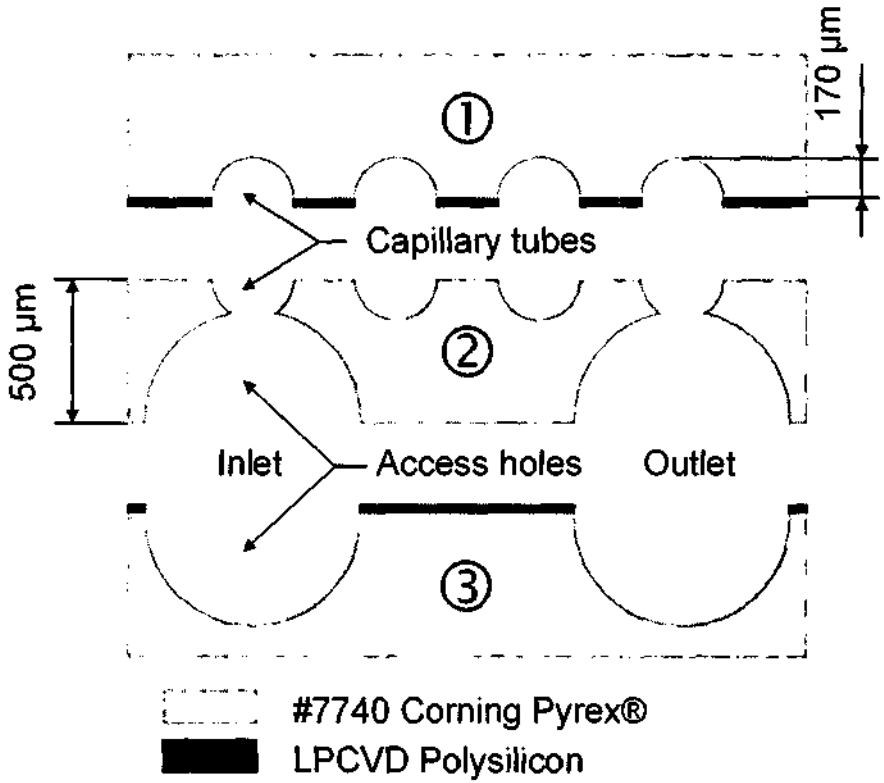

Figure 3.6: Exploded cross-section of the capillary tubes with inlet and outlet access holes just before bonding.

The capillary tubes are obtained by the assembly of the three different structured wafers, which are joined together by anodic bonding technology at about 450 °C and 700 V. The adhesion of the two Pyrex glasses is ensured by the remaining LPCVD polysilicon layer on one wafer side. The capillary tubes are assembled by fixing of the first and second glass wafers, then the lateral access holes are formed by the bonding of the third glass wafer to this glass sandwich. The unused polysilicon layers have been removed by RIE plasma etching before the bonding steps.

With the same technology, several capillary tubes have been realized by changing their length and their width. Figure 3.7 illustrates four widths of capillary tube cross-section. The widths are, from left to right, 340 µm, 440µm,

540 µm and 940 µm while the length is always 10 mm. These circular, elliptic and quasi rectangular shapes have been obtained with the same etching depth (170 µm) by changing the width of the mask. Several lengths of capillary tube have been also fabricated : 2 mm, 4 mm, 6 mm, 8 mm and 10 mm while the width is always 440 µm.

Microcolumns have also been designed to study the shape of the corner with isotropic etching of glass by 50% HF (Figure 3.8). Corner shapes without any corner compensation have been fabricated with a roughness of the inner wall surface of less than 0.1 µm (Figure 3.9). This micro-column realization has demonstrated the possibility to built compact serpentine tubes with well defined corners. All these fluidic paths have been connected by means of lateral holes (Figure 3.8). This kind of access allows easier connection between several modules stacked together without any intermediate module. Moreover the fabrication of the inlet and outlet paths has been integrated with the technology used for the capillary tubes. Circular access tubes with 840 µm diameter have been realized, which can receive 800 µm diameter needles. By using thinner glass wafers, it is also possible to realize smaller capillary tubes with similar access holes.

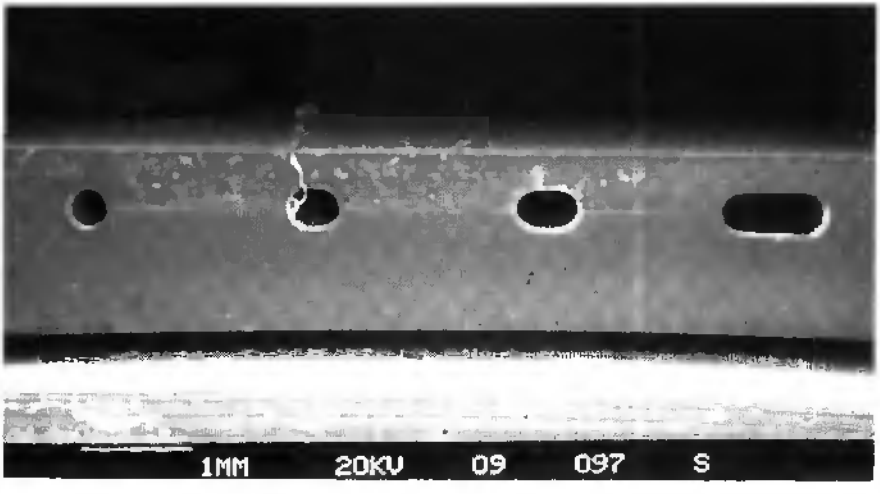

Figure 3.7: SEM of the cross-section of four capillary tubes. The widths are, from left to right: 340 µm, 440 µm, 540 µm and 940 µm.

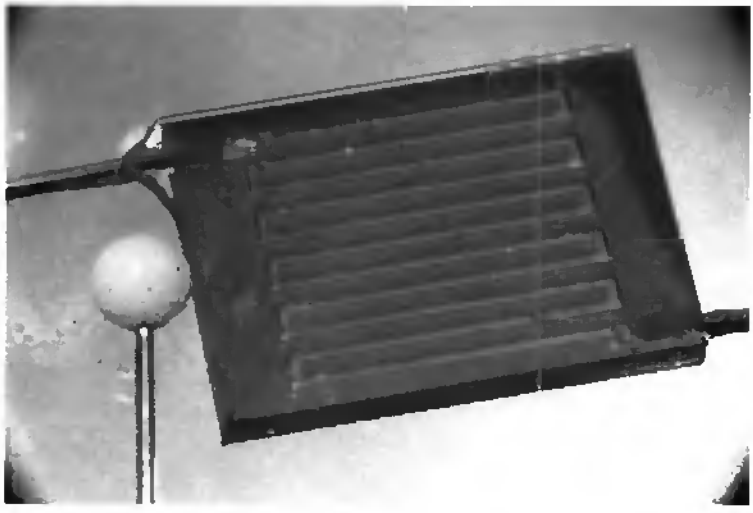

Figure 3.8: Micrograph of a microcolumn. The capillary tube is 118 mm long, with a circular cross-section (diameter: 340 μm).

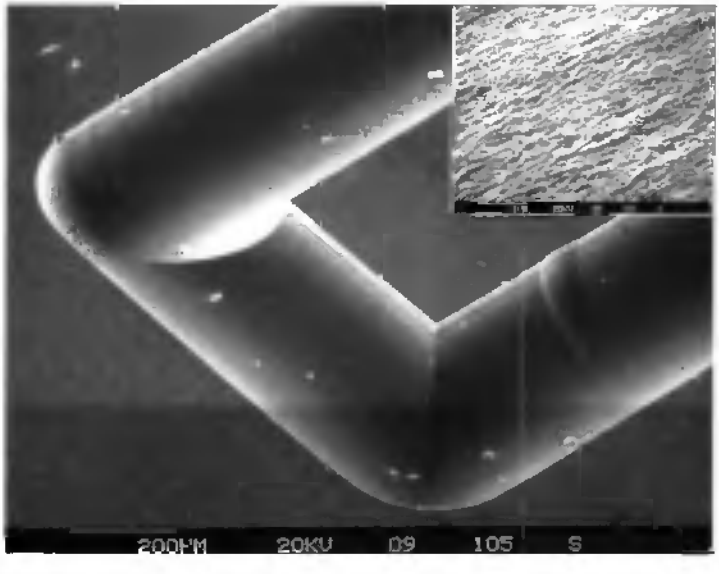

Figure 3.9: SEM of a half microcolumn corner before anodic bonding of the other part and detail of the inner wall surface roughness.

For the encapsulation of the microgyroscope, the same masking material was successfully used. For the first prototype gyroscope (chapter 2), only the top glass was micromachined (20 μm). Figure 3.1 shows the cross section of the packaged gyroscope. But for the second prototype gyroscope (chapter 4), the top and the bottom glass will both be recessed and the top one will combine deep etching (380 μm) on one side to ensure the magnet alignment with a shallow cavity (20 μm) on the other side.

Figure 3.10 illustrates the several processing steps for the top and the bottom glass. Two 7740 Pyrex glass wafers (500 μm thick) are covered with a 0.2 μm thick LPCVD polysilicon layer on both sides. The LPCVD polysilicon mask is patterned by RIE plasma. The first etching step in HF (50%) at ambient temperature is the deeper one with 360 μm. The etching rate is drastically depending of the humidity. Moreover, as the HF solution is viscous, to insure a regular etching rate of 10 μm/min even for long recessing times, the wafer has been shaken every 5 min for a better etching bath homogeneity [3.16]. The second face of the top glass has to be protected by a negativ resist like the OMR 83 (Tokyo Ohka Co.) [3.17]. Then the protection layer is removed in a nitric acid HNO_3 (100%) bath and the remaining 20 μm can be recessed. The top and the bottom glass wafer are etched in the same time to ensure the symmetric depth of the top and bottom cavities.

Figure 3.11 shows the top glass wafer with the LPCVD polysilicon mask patterned on both sides. The circular hole for the magnet has a diameter of 5 mm and is aligned with the cavity containing the vibrating structures. After the glass micromachining, the LPCVD polysilicon mask is removed in 30 seconds in a 40 % KOH bath at 60 °C. Then the glass wafers are carefully risened and dried before the anodic bonding.

Figure 3.12 illustrates the deep etching in glass substrates with different prototype gyroscopes. Details of the fabrication of second generation prototypes will be given in chapter 4.

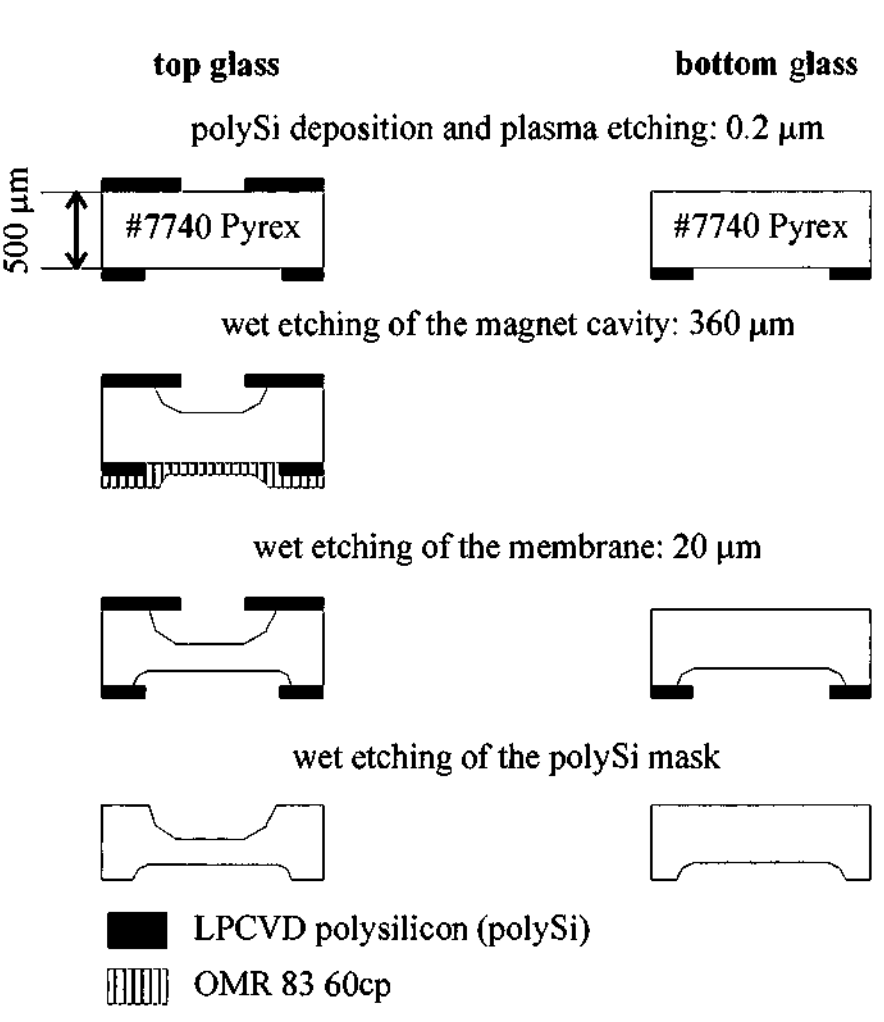

Figure 3.10: cross sections of the top and the bottom glass caps for the encapsulation of the second prototype gyroscope (chapter 4).

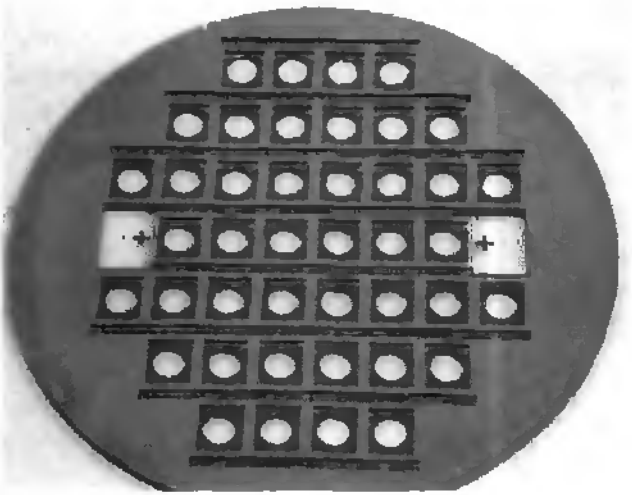

Figure 3.11: micrograph of a 4" 7740 Pyrex glass wafer with the LPCVD polysilicon mask patterned on both sides.

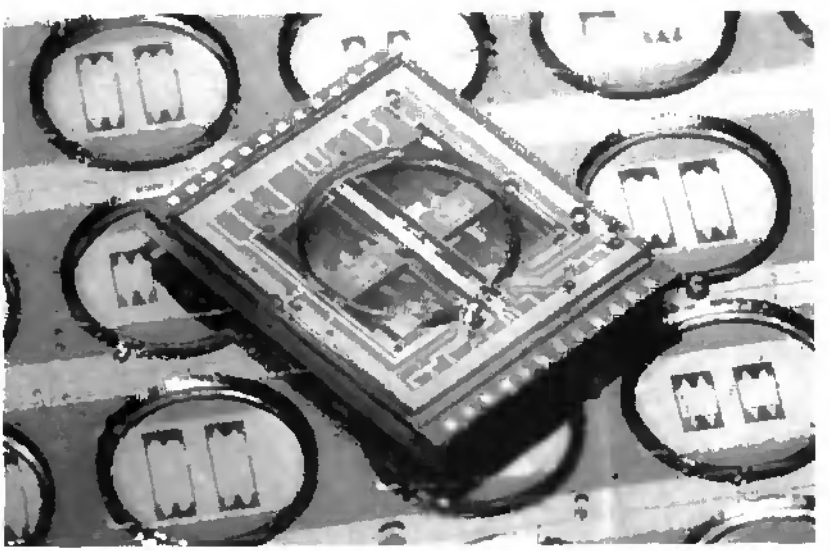

Figure 3.12: micrograph of a second prototype gyroscope encapsulated between two glass pieces (chapter 4).

3.4 Anodic bonding:

3.4.1 The bonding process:

Anodic bonding is an attractive method because it is easy to apply and requires no expensive installation. It is performed at low temperature and allows bonding to silicon surfaces with an silicon dioxide film (glass wafer, sputtered glass layer…) [3.6, 3.35]. Anodic bonding is a combined thermal and electrostatic process. It can be performed on a hot plate at temperature between 180°C and 500°C, using a DC voltage of typically 200 to 1000V. The glass needs to have a certain quantity of sodium cations, which act as charge carriers through the Pyrex because of their high mobility when the temperature is increased [3.18, 3.28]. Glass 7740 Pyrex is used because its thermal expansion matches well that of silicon [3.4, 3.14], in view of minimizing the stress in the final structure after cooling.

The basic set-up for anodic bonding is shown in Figure 3.13. To avoid dust particles, a careful handling of the two wafers and a bonding set-up in clean room atmosphere are necessary. The top glass wafer is aligned to the silicon one by optical adjustment through a binocular and thanks to the ring shape of the electrode (cathode) holding the glass substrate. In the same time, the hot plate is heating the both substrates progressively until the bonding temperature is achieved. Then the polished Pyrex surface is placed against the polished silicon surface and a negative voltage is applied to the Pyrex. The bond progress can be checked visually by observing the pattern through the Pyrex.

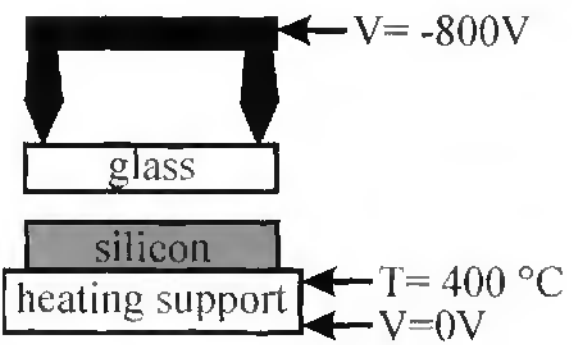

Figure 3.13: basic set-up for anodic bonding.

The Newton rings, which are typical for a small air gap, disappear. The interface becomes dark and homogeneous in color when the bond is formed. *Figure 3.14 and Figure 3.15 show the top and the bottom faces of the* encapsulated 3" wafer (chapter 3) with the patterned top Pyrex glass and the bottom Pyrex glass.

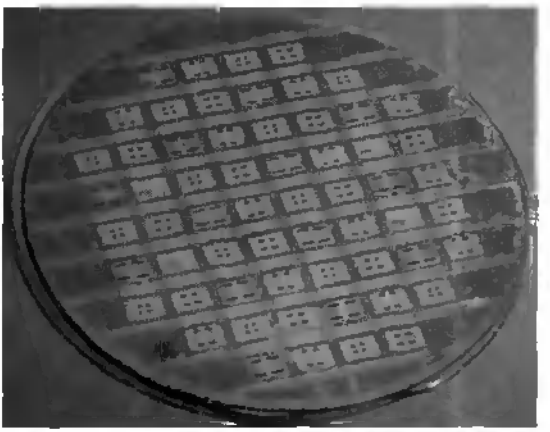

Figure 3.14: micrograph of the top side of a 3" wafer with prototype gyroscopes (chapter 2).

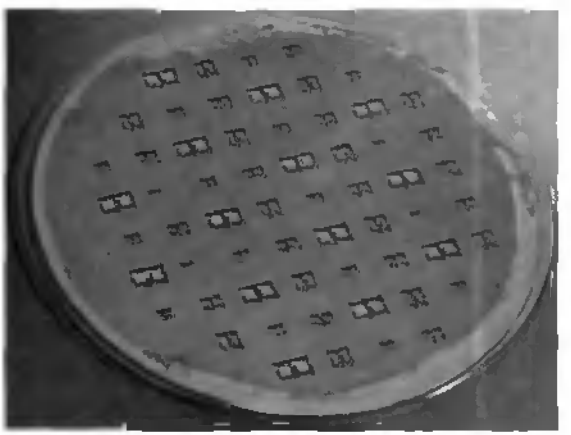

Figure 3.15 micrograph of the bottom side of a 3" wafer with prototype gyroscopes (chapter 2).

The microscopic process of bond formation is well known and is clearly explained in [3.18, 3.35]. This technique has been extensively employed not only for the microsensor encapsulation but also for the realization of glass-silicon stacks with more than two substrates [3.28, 3.35]. By the way, the stability of the silicon/glass anodic bond has been characterized [3.33, 3.39] and the possibility to reduce the pressure in the cavity (vacuum package) has also be investigated [3.31, 3.38]. For the encapsulation of the microsensors, the residual stress induced by the anodic bonding can drastically influence the microsensor behavior. Thus the bond parameters (temperature and voltage), as well as, the glass properties and the possibility of a post thermal treatment have been extensively studied [3.22, 3.27, 3.36, 3.41].

3.4.2 The dicing process:

The wafer level packaging induces that the dicing of the chips is performed afterwards. The mechanical structures are now protected during the sawing but a critical step is still to come: the dicing of the top glass wafer to uncover the bonding pads for the further electrical connections.

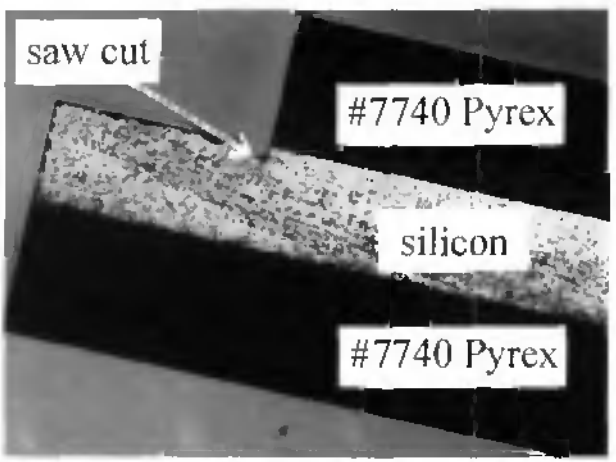

Figure 3.16: picture of a bad dicing of the top glass with the saw cut damaging the leadthroughs. The top and bottom glass substrates thickness is 500 µm and the silicon one is 400 µm.

For the first prototype gyroscopes (chapter 2), the partial dicing has been performed by subtracting 400 µm to the whole thickness of the sandwich (glass/silicon/glass). Thus a 100 µm membrane should be easily broken to release the bonding pads. This technique was employed 2 times: for one (Figure 3.14) it worked, for the other not (Figure 3.16). This results can be partially explained by the precision of the substrates thickness (for the glass wafer: 500 µm ± 5 µm) and by the precision of the dicing tool itself. Thus to achieve 100% of yield, another method has been investigated, which consists in pre-dicing the top glass substrate before the anodic bonding [3.20]. Figure 3.17 illustrates the pre-dicing process of the top glass wafer.

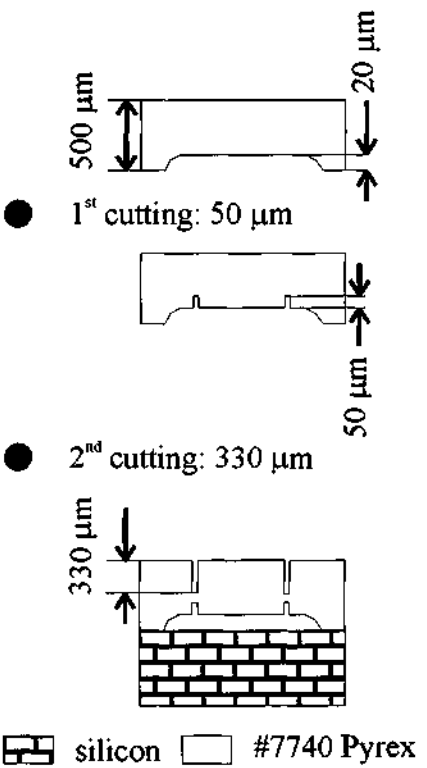

Figure 3.17: pre-dicing process for the top glass wafer of the gyroscope encapsulation.

After the micromachining of the top glass substrate, the glass wafer is partially diced (50 µm) to move the cut interface further from the silicon substrate. Then the wafer bonding is performed and the top glass wafer is partially cut (330 µm). The remaining 100 µm glasses are broken to release the metallic bonding pads without damaging the silicon substrate. Figure 3.18 shows the marks of the saw cuts in the glass membrane. The top width of the saw cut is 400 µm. Figure 3.19 illustrates the depth of the saw cut in the glass membrane.

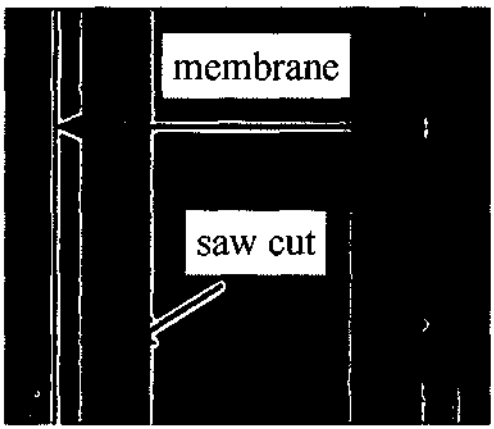

Figure 3.18: picture of the saw cuts in the glass membrane.

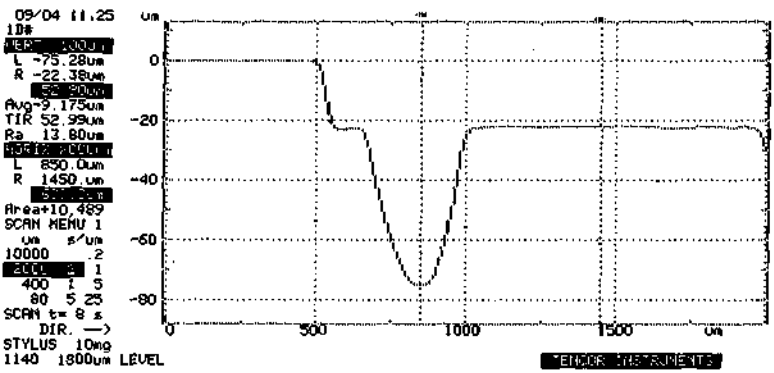

Figure 3.19: alphastep profile of the saw cut performed in the 20 µm deep glass membrane.

3.5 Conclusion:

In this chapter, different aspects of the encapsulation of microsensors have been presented. The glass micromachining, the anodic bonding and the dicing techniques have been described. The packaging steps can significantly change the device performances, thus the packaging process has to be prepared at the same time as the silicon micromachining. Both prototype gyroscopes presented in this thesis are packaged and the respective consequences for each of them have been studied (chapter 2 and chapter 4).

3.6 References:

[3.1] S. D. Senturia and R. L. Smith, "Microsensor Packaging and System partitioning", Sensors & Actuators, 15 (1988), pp. 221-234.

[3.2] G. Kelly, J. Alderman, C. Lyden and J. Barrett, "Microsystem packaging: lessons from conventional low cost IC packaging", Journal of Micromechanics and Microengineering, Vol. 7 1997, pp. 99-103.

[3.3] K. Dyrbye, T. Romedahl Brown and G. F. Eriksen, "Packaging of Physical Sensors for Aggressive Media Applications", Technical Digest of The 6th Workshop on Micromachining, Micromechanics and Microsystems, MME '95, Copenhagen, Denmark, September 1995, pp. 315-323.

[3.4] W. H. Ko, J. T. Sumitomo and G. J. Yeh, "Bonding Techniques for Microsensors", Micromachining and Micropackaging of Transducer's, Elsevier Science Publishers, Amsterdam, The Netherlands, 1985, pp. 41-61.

[3.5] S. Shoji and M. Esashi, "Bonding and Assembling Methods for Realising a μTAS", Proceedings of Miniaturized Total Analysis Systems, μ-TAS94, Twente, The Netherlands, November 1994, pp. 165-179.

[3.6] M. A. Schmidt, "Silicon wafer bonding for micromachined devices", Technical Digest of IEEE Solid-State Sensor and Actuator Workshop, Hilton Head Island, SC, June 1994, pp. 127-131.

[3.7] P. W. Barth, F. Pourahmadi, R. Mayer, J. Poydock and K. Pertesen, "A monolithic silicon accelerometer with integral air damping and overrange protection", Technical Digest of IEEE Solid-State Sensor and Actuator Workshop, Hilton Head Island, SC, June 1988, pp. 35-38.

[3.8] J. D. Starr, "Squeeze-film damping in solid-state accelerometers", Technical Digest of IEEE Solid-State Sensor and Actuator Workshop, Hilton Head Island, SC, June 1988, pp. 44-47.

[3.9] T. Tschan, "Simulation, design and characterization of a piezoresistive accelerometer fabricated by a bipolar-compatible industrial process", Ph.D. Thesis, Institute of Microtechnology, University of Neuchâtel, Switzerland, 1992.

[3.10] R. P. Van Kampen, "Bulk-micromachined capacitive servo-accelerometer", Ph. D. dissertation, Technology University of Delft, 1995.

[3.11] R.-A. Buser, "Theoretical and experimental investigations on silicon single crystal resonant structures", Ph. D. dissertation, Institute of Microtechnology, University of Neuchâtel, Switzerland (1989).

[3.12] M. Esashi, "Encapsulated micro mechanical sensors", Microsystem Technologies, Vol. 1 1994, pp. 2-9.

[3.13] J. H. Martin, "Micromechanical gyroscope packaging history and projections", Proceedings of the 1994 International Electronics Packaging Conference, Atlanta, GA, September 1994, pp. 470-480.

[3.14] Data sheet: Corning 7740 borosilicate Pyrex®, Corning Keramik GMBH & CO., Abraham-Lincoln Strasse 30, D-65189 Wiesbaden, Germany.

[3.15] T. R. Dietrich, "Photostructurable glass", Materials for microstructures (edited by UETP MEMS FSRM Training in microsystems), 1996, pp. 161-182.

[3.16] C. B. Shin and D. J. Economou, "Effect of transport and reaction on the shape evolution of cavities during wet chemical etching", Journal of the Electrochemical Society, Vol. 136, N°. 7 1989, pp. 1997-2004.

[3.17] S. Shoji and M. Esashi, "Photoetching and electrochemical discharge drilling of pyrex glass", Technical Digest of The 9th Sensor Symposium, 1990, pp. 27-30.

[3.18] K. B. Albaugh, "Electrode phenomena during anodic bonding of silicon to sodium borosilicate glass", Journal of the Electrochemical Society, Vol. 138 N°. 10 1991, pp. 3089-3094.

[3.19] D. Hülsenberg, A. Harnisch, H.-J. Horst, K. Schmidt and B. Straube, "New Glasses for Microsystem Technologies", Proceedings of the 4th International Conference on Micro Electro, Opto, Mechanic Systems and Components, Micro System Technologies 94, Berlin, Germany, October 1994, pp. 259-268.

[3.20] H. R. C. Strato, "Glass Technology", Master Thesis, Department of Electrical Engineering, TU Delft, the Netherlands, A94-09, August 1994.

[3.21] T. Diepold and E. Obermeier, "Smoothing of ultrasonically drilled holes in borosilicate glass by wet chemical etching", Technical Digest of The 6th Workshop on Micromachining, Micromechanics and Microsystems, MME '95, Copenhagen, Denmark, September 1995, pp. 35-38.

[3.22] T. Rogers and J. Kowal, "Selection of Glass, Anodic Bonding Conditions and Material Compatibility for Silicon-Glass Capacitive Sensors", Sensors & Actuators, A46-47 (1995), pp. 113-120.

[3.23] T. Diepold and E. Obermeier, "Bulk micromachining of borosilicate glass by ultrasonic drilling and sand blasting", Proceedings of the 5th International Conference on Micro Electro, Opto, Mechanic Systems and Components, Micro System Technologies 96, Potsdam, Germany, September 1996, pp. 211-217.

[3.24] M.-A Grétillat, F. Paoletti, P. Thiébaud, S. Roth, M. Koudelka-Hep and N.F. de Rooij, "A New Fabrication Method for Borosilicate Glass Capillary Tubes with Lateral Inlets and Outlets", Sensors & Actuators, A 60 (1997), pp. 219-222.

[3.25] D. Hülsenberg, "Glasses for microsystems technology", Microelectronics Journal, Vol. 28 N°. 4 1997, pp. 419-432.

[3.26] T. Corman, P. Enoksson and G. Stemme, "Deep wet etching of borosilicate glass using an anodically bonded substrate as mask", Journal of Micromechanics and Microengineering, Vol. 8 (1998), pp. 84-87.

[3.27] H. L. Offereins, H. Sandmaier, B. Folkmer, U. Steger and W. Lang, "Stress free assembly technique for a silicon based pressure sensor", Digest of Technical Papers of the 6th International Conference on Solide-State Sensors and Actuators, Transducers '91, San Francisco, CA, June 1991, pp. 986-989.

[3.28] M. Harz, "Anodic Bonding for the Third Dimension", Journal of Micromechanics and Microengineering, 2 (1992), pp. 161-163.

[3.29] M. Nese and A. Hanneborg, "Anodic Bonding of Silicon to Silicon Wafers Coated with Aluminium, Silicon Oxide, Polysilicon or Silicon Nitride", Sensors & Actuators, A37-38 (1993), pp. 61-67.

[3.30] C. Cabuz, S. Shoji, K. Fukatsu, E. Cabuz, K. Minami and M. Esashi, "Fabrication and Packaging of a Resonant Infrared Sensor Integrated in Silicon", Sensors & Actuators, A43 (1994), pp. 92-99.

[3.31] H. Henmi, S. Shoji, Y. Shoji, K. Yoshimi and M. Esashi, "Vacuum Packaging for Microsensors by Glass-Silicon Anodic Bonding", Sensors & Actuators, A43 (1994), pp. 243-248.

[3.32] Y.-C Lin, P. J. Hesketh, J. P. Schuster , "Finite-element analysis of thermal stresses in a silicon pressure sensor for various die-mount materials", Sensors & Actuators A - Physical, A 44 (1994), pp. 145-149.

[3.33] D. S. Hurd, R. Caretta and W. W. Gerberich, "An experimental fracture mechanics study of a strong interface: the silicon/glass anodic bond", Journal of Materials Research, Vol. 10 N°. 2 (1995), pp. 387-400.

[3.34] K. Hilgendorf, P. Krause and E. Obermeier, "Reduction of the Influence of the Anodic Bonding Process on the Behavior of Pressure Sensors by Using New Glass Substrates", Proceedings of the 5th International Conference on Micro Electro, Opto, Mechanic Systems and Components, Micro System Technologies 96, Potsdam, Germany, September 1996, pp. 331-336.

[3.35] M. Despont, H. Gross, F. Arrouy, C. Stebler and U. Staufer, "Fabrication of a silicon-pyrex-silicon stack by a.c. anodic bonding", Sensors & Actuators A - Physical, A 55 (1996), pp. 219-224.

[3.36] M. Harz and W. Brückner, "Stress reduction in anodically bonded silicon and borosilicate glass by thermal treatment", Journal of the Electrochemical Society, Vol. 143 N°. 4 1996, pp. 1409-1414.

[3.37] WB. Choi, BK. Ju, YH. Lee, MR. Haskard, MY. Sung and MH. Oh, "Anodic bonding technique under low temperature and low voltage using evaporated glass", Journal of Vacuum Science & Technology B, Vol. 15 N°. 2 1997, pp. 477-481.

[3.38] S. Mack, H. Baumann, U. Gösele, H. Werner and R. Schlögl, "Analysis of bonding-related gas enclosure in micromachined cavities sealed by silicon wafer bonding", Journal of the Electrochemical Society, Vol. 144 N°. 3 1997, pp. 1106-1110.

[3.39] J. Plaza, J. Esteve and E. Lora-Tamayo, "Nondestructive anodic bonding test", Journal of the Electrochemical Society, Vol. 144 N°. 5 (1997), pp. L108-L110.

[3.40] F. Schilling, W. Langheinrich, K. Weiblen and D. Arand, "Simulation of thermally induced package effects with regard to piezoresitive pressure sensors", Sensors & Actuators A - Physical, A 60 (1997), pp. 37-39.

[3.41] S. Shoji, H. Kikuchi and H. Torigoe, "Low-temperature anodic bonding using lithium aluminosilicate-b-quartz glass ceramic", Sensors & Actuators A - Physical, Vol. 64 (1998), pp. 95-100.

[3.42] F. Paoletti, M.-A. Grétillat and N. F de Rooij, "A Silicon Micromachined Vibrating Gyroscope with Piezoresistive Detection and Electromagnetic Excitation", Proceedings of the 9th IEEE Workshop on Micro Electro Mechanical Systems, MEMS '96, San Diego, CA, pp. 162-167, February 1996.

[3.43] W. Kaplan, H. Elderstig and C. Vieider, "A novel fabrication method of capillary tubes on quartz for chemical analysis applications", Proceedings of the 7th IEEE Workshop on Micro Electro Mechanical Systems, MEMS '94, Oiso, Japan, January 1994, pp. 63-68.

[3.44] D. Sobek, S. D. Senturia and M. L. Gray, "Microfabricated fused silica flow chambers for flow cytometry", Technical Digest of IEEE Solid-State Sensor and Actuator Workshop, Hilton Head Island, SC, June 1994, pp. 260-263.

[3.45] A. Manz, N. Graber and H. M. Widmer, "Miniaturized total chemical analysis systems: a novel concept for chemical sensing", Sensors & Actuators, B1 (1990), pp. 244-248.

[3.46] P. Gravesen, J. Branebjerg and O. S. Jensen, "Microfluidics - A Review", Technical Digest of The 4th Workshop on Micromachining, Micromechanics and Microsystems, MME '93, Neuchâtel, Switzerland, September 1993, pp. 143-164.

[3.47] B. H. van der Schoot, E. M. J. Verpoorte, S. Jeanneret, A. Manz and N. F. de Rooij, ", "Microsystems for analysis in flowing solutions", Proceedings of Miniaturized Total Analysis Systems, μ-TAS94, Twente, The Netherlands, November 1994, pp. 181-190.

[3.48] D. J. Strike, P. Thiébaud, A. C. van der Sluis, M. Koudelka-Hep and N. F. de Rooij, "Glucose measurement using a micromachined open tubular heterogeneous enzyme reactor (MOTHER)", Microsystem Technologies, Vol.1 N°1 (1994), pp. 48-50.

4. Improved gyroscope design

4.1 Introduction:

Micromachining is one of the most important emerging technologies for inertial sensors (accelerometers and gyroscopes) because it offers small size and low cost. Commercial issues are not negligible: the microelectromechanical systems (MEMS) world wide market in 1995 was $ 2.7 billion (US) of which the automotive market comprised 41% for pressure sensors and inertial sensors [4.1, 4.2]. Thus research and development activities in micromachined gyroscopes are intensively undertaken both in industry and in university [4.3].

In chapter 2, a first silicon micromachined gyroscope with electromagnetic excitation and piezoresistive detection has been presented. Several prototype gyroscopes have been tested and have shown promising results in a range of ±700 deg/sec [4.4]. Unfortunately further measurements have shown an important bias drift, which makes the sensor unsuitable for real applications [4.5, 4.6].

To overcome these drawbacks, a new design of the silicon micromachined gyroscope was realized. The sensor was modified to have increased symmetry and less parasitic vibrations induced by any misalignment of the suspension beams and the center of inertia of the proof masses (Figure 4.1). The resonant frequency of the first mode and the resonant frequency of the second mode have been separated to avoid cross-coupling between both modes. Thus the out of plane motion due to the rotation will be sensed at the first resonant frequency and uncoupled from the vertical vibrations due to the second resonant frequency [4.7, 4.8, 4.9].

In this chapter, a new design of silicon micromachined gyroscope with the above mentioned mode decoupling, piezoresistive detection and electromagnetic excitation is presented. The design and the main fabrication steps are described. Results of the dynamic behavior and the temperature dependence will be presented. Also results of rotation measurement and the sensor stability will be given.

4.2 Design:

4.2.1 Principle:

For the typical requirements in the automotive market, despite the shortcomings of miniaturizing, the inertial sensors have to achieve outstanding performances, low power requirements and mechanical robustness [4.1, 4.2]. Several designs for micromachined gyroscopes exist [4.3]. The gyroscope design in this study is based on the tuning fork principle. It is operated by vibrating two tines in antiphase in one plane. A rotation around the axis which is parallel with the tines will generate a vibration out of this plane due to the Coriolis force. This out of plane deflection of the tines can be used to determine the rotation around the working axis [4.10].

Both bulk micromachining and surface micromachining have been investigated to realize angular rate sensors [4.11, 4.12, 4.13]. For the detection path, piezoresistors are well suited to the mechanical strain sensing [4.14, 4.15]. For the antiphase driving, Lorentz forces provide large displacements with relatively low currents (< 10 mA) and are independent of the proof mass position [4.16].

4.2.2 Previous gyroscope design:

Figure 4.1 illustrates the previous gyroscope concept.

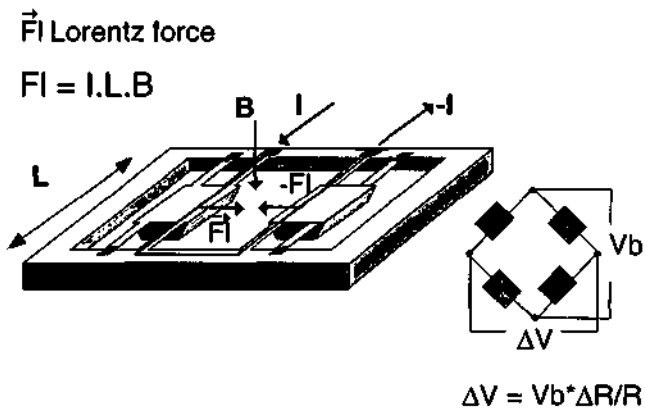

Figure 4.1: schematic of the previous gyroscope design (chapter 2).

The two tines of the tuning fork were replaced with two proof masses suspended by four beams [4.4]. When an AC current (I) flowed along the U-shaped metallic conductor (length L) placed on top of the proof masses, the interaction of this current with a perpendicular magnetic induction (B) resulted in an antiphase Lorentz force [4.4]. When rotating the gyroscope, the out of plane vibration of the proof masses due to the Coriolis force was sensed by means of four piezoresistors centered on top of the external beams and connected in a Wheatstone bridge configuration. As the beam cross section had a square shape, the detection path was both sensitive to the Coriolis force and the mechanical coupling of the driving mode in the sensing direction. Excitation of the gyroscope at its mechanical resonant frequency was not possible and a large zero rate output (ZRO) drift was measured [4.4, 4.6]. Finite Element Modeling (FEM) of the first prototype gyroscope confirmed that the matching of the driving and the detection frequency led a large output without any rotation because the driving mode was not a pure in plane movement but a rocking mode with a non negligible component in the sensing direction [4.4, 4.17, 4.18]. Moreover, the detection path was unable to separate the signals of the driving motion from the sensing one because the piezoresistors implanted on the external beams could sense the out of plane vibration of both modes [4.4].

4.2.3 New improved gyroscope design:

The new design was reached after a critical analysis of the shortcomings of the previous design. The design of the proof masses has been changed to give improved symmetry and to reduce the out of plane movements due to the excitation [4.7, 4.8, 4.19]. The first excited mode should be the horizontal one, pure or quasi-pure translation, then the vertical mode, pure translation orthogonal to the previous one and the rocking mode far away from the two other ones [4.4, 4.17]. As the beams cross section is no more square, the resonant frequency of the mode in the horizontal (excitation) direction and the resonant frequency of the second mode in the vertical (detection) direction are not matched thus avoiding mechanical cross-coupling [4.7, 4.8]. Moreover, the gyroscope is operated at the resonant frequency of the first mode and the detection performed at the same frequency.

Both the mass and the suspension beams are 400 µm thick (Figure 4.2). The beam's width is 40 µm and its length is 2000 µm so allowing large horizontal displacements. Both beams on one side of the proof mass are connected to the silicon frame by a thinner plate to achieve a better compromise between the mode separation and the sensitivity of the gyroscope.

FEM analysis of the resonant frequencies of the gyroscope has been performed first with a simple design: the proof mass was directly connected to the silicon frame by the suspension beams. This simplest design was rejected since high aspect ratio of the suspension beam dimensions (1:10 width/thickness) led to a high stiffness in the vertical mode and would drastically limit the sensitivity of the gyroscope. The first resonant frequency (horizontal motion) and the second resonant frequency (vertical motion) were respectively found about 6 kHz and 60 kHz.

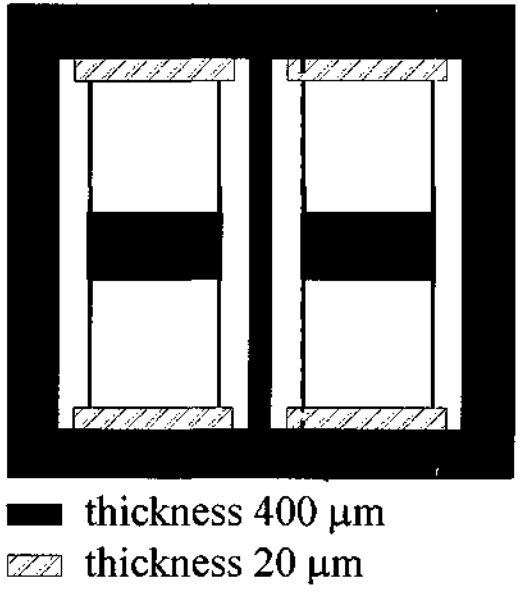

Figure 4.2: schematic of the new gyroscope design with the thickness of the different parts (proof mass, suspension beam and detection plate). The proof mass is 1000 µm long, 2000 µm wide and 400 µm thick. The suspension beams are 2000 µm long and 40 µm wide. The detection plate is 20 µm thick and its length can be either 250 µm and 500 µm.

For the improved design, the same frequencies were about 6 kHz and 25 kHz with a detection plate thickness of 20 µm and length of 250 µm. Three different designs of the detection plate have been chosen (Figure 4.3).

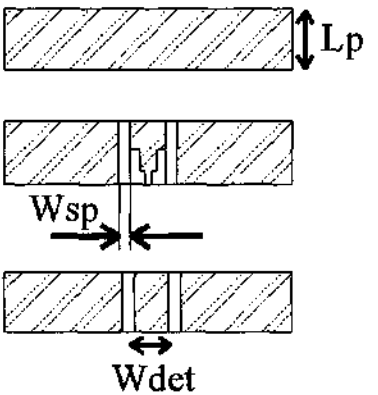

Figure 4.3: 3 different designs of the center part of the detection plate: the simple plate, the pyramid (P) shape and the beam (B) shape. The spacing width between the plate and the center part (W_{sp}) is 20 µm and the width of the center part (W_{det}) is 120 µm.

Special central part (beam (B) or pyramid (P)), where the piezoresistors for the Coriolis force will be implanted, have been patterned in the plate to uncouple this central part from the whole plate. Table 4.1 resumes the six different designs of the new gyroscope, which will be realized on the same wafer. For each type of detection plate (plate, beam and pyramid), two plate lengths (250 µm and 500 µm) will be used.

Plate design (center part)	Plate length (µm)	250	500
simple	reference	250	500
beam	reference	250B	500B
pyramid	reference	250P	500P

Table 4.1: the six different designs of the new gyroscope with 3 center part shapes and 2 lengths for the detection plate.

Thanks to the plate design, the piezoresistors for the Coriolis force detection can be moved from the edge to the center of the mass where the vertical displacement due to the driving mode is smaller (Figure 4.4). In addition, piezoresistors are dedicated to the measurement of the excitation amplitude and also to the measurement of the detection amplitude. Each proof mass driving motion is sensed by the combination of a fixed piezoresistor on the silicon frame and a sensing piezoresistor implanted on the plate in the continuation of the suspension beams.

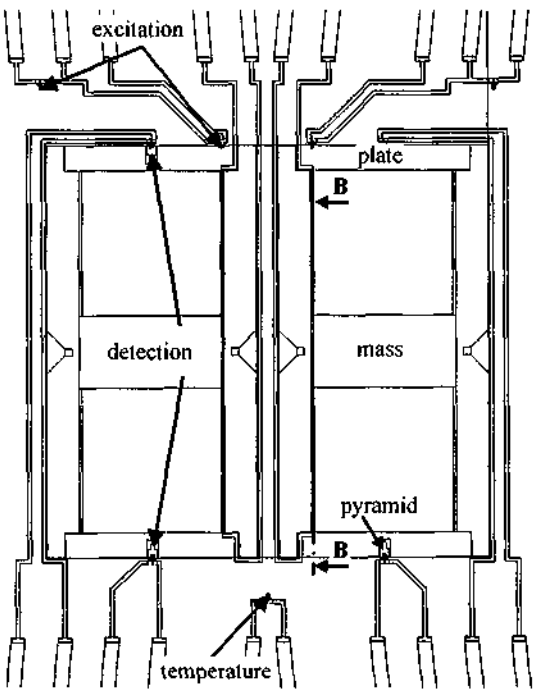

Figure 4.4: top view of the new gyroscope design. The arrows are pointing out the different piezoresistor locations depending of their purpose (temperature, driving and Coriolis force sensing).

For the Coriolis force, two sensing piezoresistors are implanted on each side of the proof mass in the center part of the detection plates. Moreover, each proof mass can be driven separately or in antiphase to enable a better understanding of the dynamic behavior of the gyroscope (Figure 4.4).

4.3 Fabrication:

4.3.1 Advanced Deep Reactive Ion Etching (ADRIE):

The fabrication of microelectromechanical systems (MEMS) has always relied on several sophisticated techniques. The surface micromachining [4.20, 4.21] and the bulk anisotropic silicon etching [4.14, 4.15, 4.16] were used to build pressure sensors, inertial sensors, micropumps, micromotors, xy-stages and other smart devices [4.22, 4.23]. Both technologies suffer some limitations such as the sticking of the structures for the surface micromachining and the silicon crystal orientation dependency for the anisotropic etching.

Deep silicon dry etching has been investigated to extend the bulk micromachining and to fulfill some requirements like: etch depths from 20 µm to 300 µm, aspect ratio greater than 10 and more freedom in the design [4.24, 4.25, 4.26, 4.27, 4.28, 4.29, 4.30]. First trials with deep reactive ion processes have shown that by extending the etching time, the photoresist mask deteriorated faster due to the increasing temperature of the substrate [4.24]. Thick photoresist [4.25, 4.30], multilayer [4.26, 4.27] and silicon dioxide [4.28, 4.31] mask or low-temperature wafer stage [4.26] have been investigated. In both cases, trade-off between the etching rate and the etching selectivity to the mask has been observed. Therefore advanced deep reactive ion etching (ADRIE) tools have been proposed [4.32, 4.33, 4.34]. There are currently two ADRIE systems available on the market. One system is manufactured by Alcatel [4.33] and the other by STS [4.35]. For these new tools, silicon etch rates up to 2 µm/min, with geometrical aspect ratio of at least 15:1, even at depths up to 300 µm are obtained. Different micro structures have been fabricated successfully with both equipments [4.36, 4.37, 4.38].

The second prototype gyroscope has been fabricated with the commercial ADRIE etcher from STS Ltd., Gwent, UK. Preliminary tests have been performed to optimize the deep etching process. The aims were the following:

etching a 400 µm thick wafer from both sides (etch depth: back side 380 µm and front side 20 µm) and maintaining the high aspect ratio of the suspension beams (width 40 µm, thickness 400 µm). The back side deep etching step have been tested with (100) double side polished 400 µm thick silicon wafer. Figure 4.5 illustrates the underetching of the suspension beams. The remaining membrane thickness is 18 µm. Even the support bar (left hand side of Figure 4.5) to fixed the suspension beams to the detection plate has been underetched. Its width was designed to 100 µm and Figure 4.6 shows a closer view of the support bar cross section.

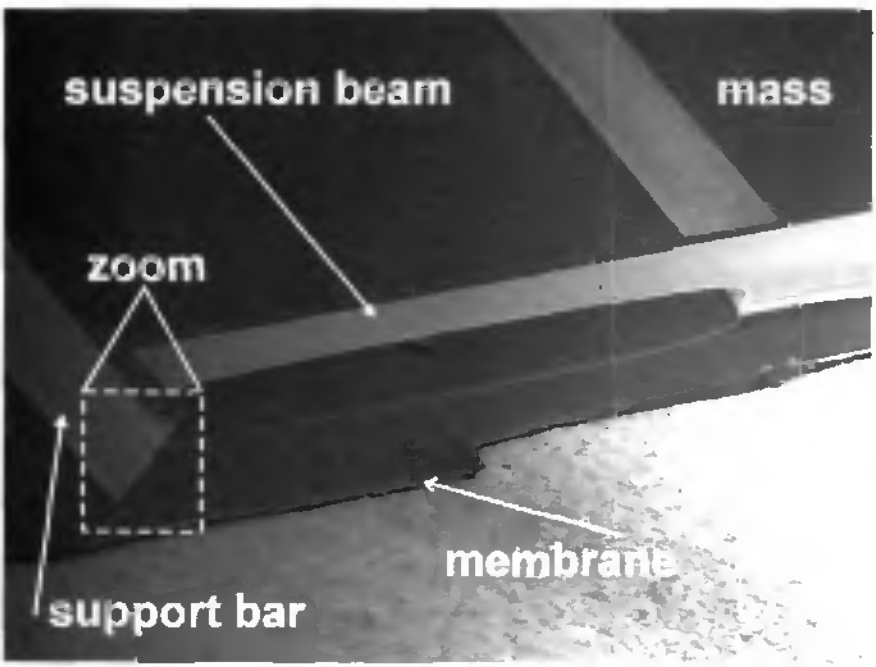

Figure 4.5: SEM picture of the back side etching of a silicon prototype gyroscope. The wafer is 400 µm thick and the remaining membrane thickness is 18 µm. The length of the suspension beams is 2 mm.

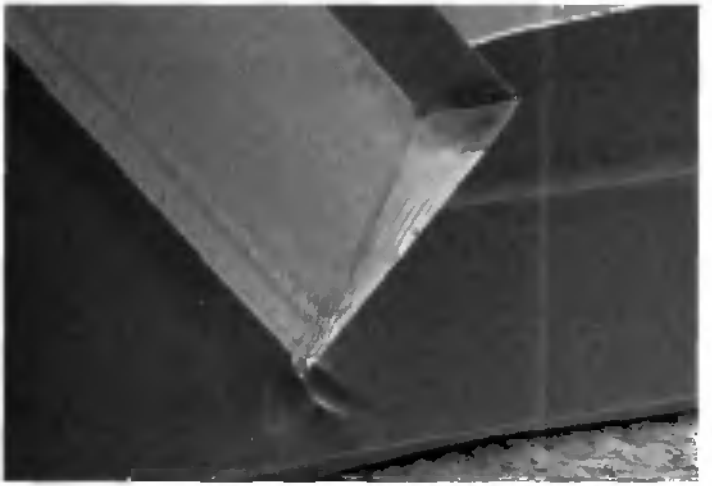

Figure 4.6: SEM closer view of the cross section of the support bar. Its top width is designed to 100 μm.

To overcome the underetching of the suspension beams, two new options have been investigated. Double side polished silicon on insulator (SOI) wafers have been preferred because the buried silicon dioxide layer could be used as an etch stop layer and the top side layer thickness would be the same for the whole surface of the wafer [4.32].

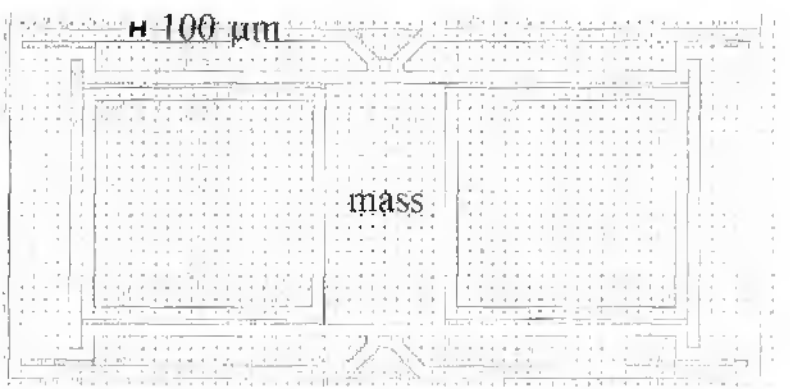

Figure 4.7: the optimized back side mask design for the deep etching of silicon (380 μm).

An optimized back side mask has been designed to reduce the open area around the beams because the etching rate in silicon was drastically depending from the open surface. Large areas were etched deeper than narrow areas in the same time [4.36]. Figure 4.7 shows the optimized mask layout for the back side etching.

The two following pictures illustrate the reduced under etching of the suspension beams by using the optimized mask and a SOI wafer. Figure 4.8 shows a beam profile from the top side (20 µm thick) for a chip from the edge of the wafer and Figure 4.9 for a chip from the center of the same wafer. In Figure 4.8, the top silicon layer is released from the bottom one by the underetching. The roughness of the sidewalls by ADRIE technique for the bottom silicon layer is shown in Figure 4.8 and in Figure 4.9. With the optimized layout, an underetching is still observed at the edge of the wafer and can be reduced with further optimization of the back side mask by increasing the etch width from the edge to the center of the mask [4.36].

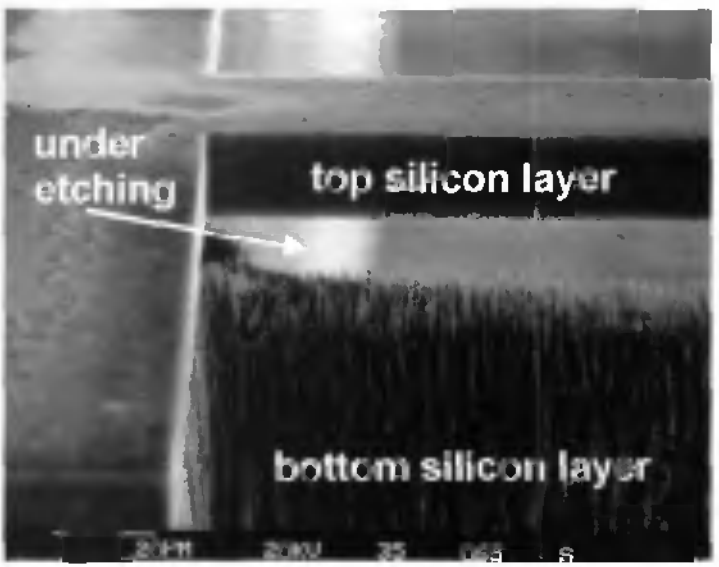

Figure 4.8: SEM picture of a suspension beam profile for a chip from the edge of a SOI wafer. The top side layer is 20 µm thick.

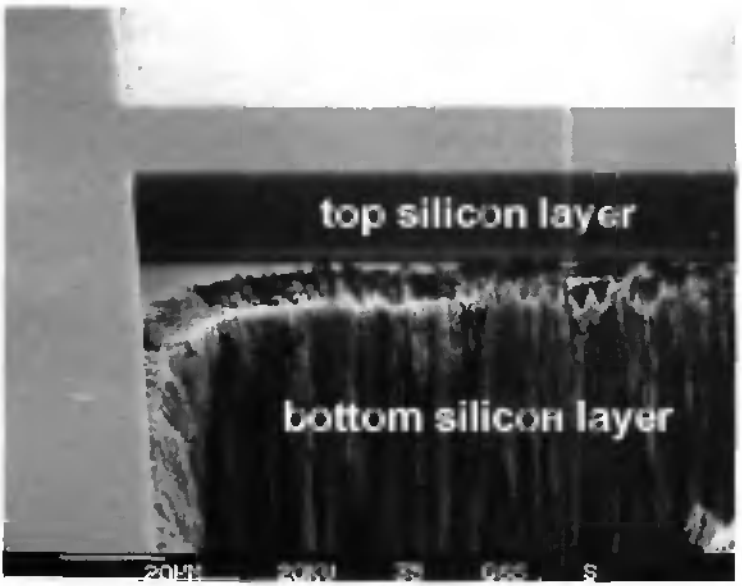

Figure 4.9: SEM picture of a suspension beam profile for a chip from the center of a SOI wafer. The top side layer is 20 µm thick.

4.3.2 Piezoresistive detection:

Piezoresistive detection has been extensively used for pressure sensors and accelerometers [4.14, 4.15, 4.39]. For both gyroscope prototypes, (100) silicon wafers have been used and the sensing direction was (110). Thus p-type piezoresistors have been designed because their longitudinal piezoresistor coefficient (π_l) was larger than for the n-type [4.14]. The piezoresistor shape was a U shape to cancel the transversal sensitivity of each branch for a piezoresistor centered on a suspension beam (first prototype) or on a detection plate (second prototype) [4.14]. Finally the piezoresistor was placed on the frame side for an easier interconnection by the frame and its length was fixed by a ratio of 1:8 of the detection plate length for this new gyroscope design [4.15].

The piezoresistor length was chosen by considering the stress distribution on the surface of the detection plate [4.15]. Piezoresistors have been implanted because shallow junction and steeper concentration profile can be achieved. Thus a higher sensitivity to the stress and a better control of temperature behavior will be obtained [4.14]. But the piezoresistor characteristics are drastically depending from the further thermal processes. Thanks to technical simulation tools like Athena™ (product of SILVACO), the whole thermal process can be simulated to realize the doping areas for the prototype gyroscope: the implanted p-type piezoresistors (PIEZO), the chemical vapor deposited (CVD) doped p-type connectors (CONP+) for the feedthroughs and the CVD doped n-type substrate contacts (SUBN+). The extracted parameters are the sheet resistor (R(ohm/square)) and the junction depth (X_j). In Table 4.2, the simulation results and some measurements results are compared.

Type	**Process**	**Simulation**		**Measurement**	
		R (ohm/square)	*Xj (μm)*	*R (ohm/square)*	*Xj (μm)*
PIEZO	implantation	182	0.96	215.3	0.8
CONP+	CVD	14.5	2.9	14.1	NA
SUBN+	CVD	8.7	NA*	6.5	NA

*NA not available

Table 4.2: the simulation and measurement results for different doping examples.

For the piezoresistor implantation (dose: 2.5e15 at/cm^2 and energy: 40 keV) in a n-type substrate (resistivity: 10 ohm.cm), Figure 4.10 shows the doping concentration profile after the polysilicon anneal (1050°C, 30 min), which represents the highest thermal treatment after the implantation. High temperature anneal have to be limited after the implantation because the concentration profile will be deeper and thus higher temperature dependence will be obtained [4.14].

The doping concentration has been measured with the sheet resistor in a test cell included in the mask layout. For each doping type, five resistors with different number of squares have been designed (Figure 4.11) [4.40]. The sheet resistor was calculated by the slope of the resistor curve versus the number of squares (Figure 4.12).

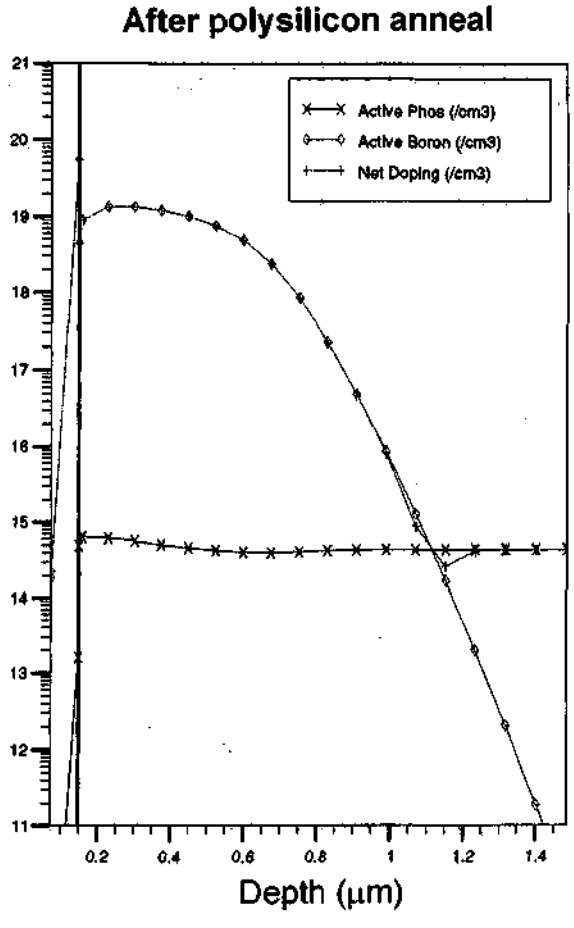

Figure 4.10: the simulated doping profile for the piezoresistor implantation.

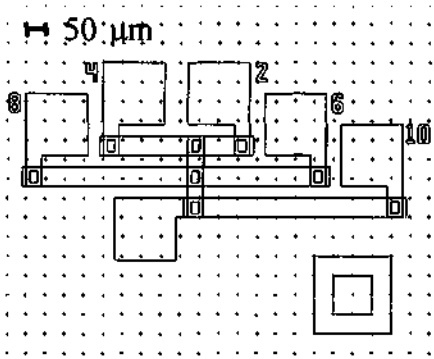

Figure 4.11: the mask layout for the sheet resistor measurement.

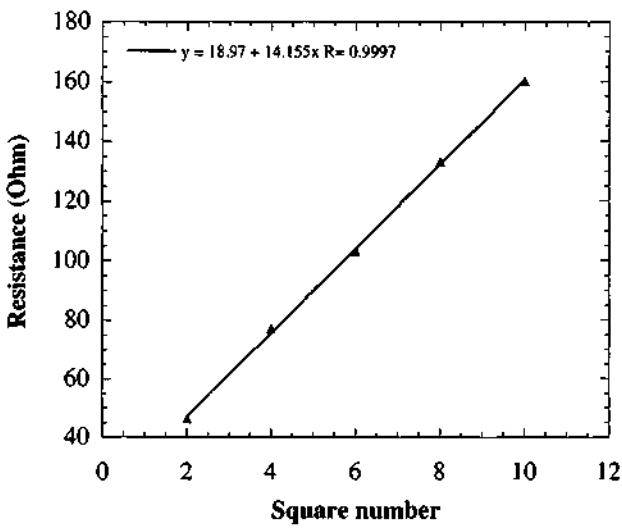

Figure 4.12: the CVD doped p-type connector (CONP+) resistor versus the number of squares.

4.3.3 Silicon micromachining:

Double side polished silicon on insulator (SOI) n-type wafers are used for the fabrication of the gyroscopes. The ADRIE process requires SOI substrates for the etch stop technique [4.32, 4.38]. The high aspect ratio (1:10) of the suspension beams is obtained by backside etching through the whole thickness of the base silicon layer of the SOI wafer (380 µm) and the topside etching of the top silicon layer (20 µm), while the 1 µm thick silicon dioxide layer is used as a buried etch stop. The main processing steps are explained in Figure 4.13 with a cross section along the suspension beams and the proof mass in the longitudinal direction.

The first processing steps concern the top side of the wafer. The boron doped (p^{++}) connectors are diffused. They connect the inside metallic lines and the piezoresistors with the outside metallic pads. A silicon dioxide (700 Å) layer, a LPCVD (Low pressure chemical vapor deposition) silicon nitride (2000 Å) layer and a LPCVD polysilicon (5000 Å) layer are deposited. Both LPCVD layers are removed on the back side. The LPCVD polysilicon layer is patterned on the front side to realize a frame for the packaging. The silicon dioxide and the LPCVD silicon nitride are opened to connect the diffused layers with a thick aluminum (1 µm) layer evaporated and patterned to build the excitation line and to connect the piezoresistors together.

Then the proof masses and the beams are shaped out of the silicon, using the ADRIE process with a photoresist mask, first from the back side with a 380 µm etch depth and then from the front side with a 20 µm etch depth to define at the same time the thin detection plates. Finally the vibrating structure is completely released by the wet etching of the 1 µm thick buried silicon dioxide. Two shapes (beam B and pyramid P) have been designed in the detection plate, where the piezoresistors would be implanted (Figure 4.3). Figure 4.14 illustrates the pyramid design for a detection plate length of 250 µm. Figure 4.15 is a SEM picture of a suspension beam attached on one side at the edge of a seismic mass (left hand corner).

The whole process for the new gyroscope design is described step by step in the following tables (Table 4.3, Table 4.4).The mask name as well as the thickness of the deposited layers are mentioned.

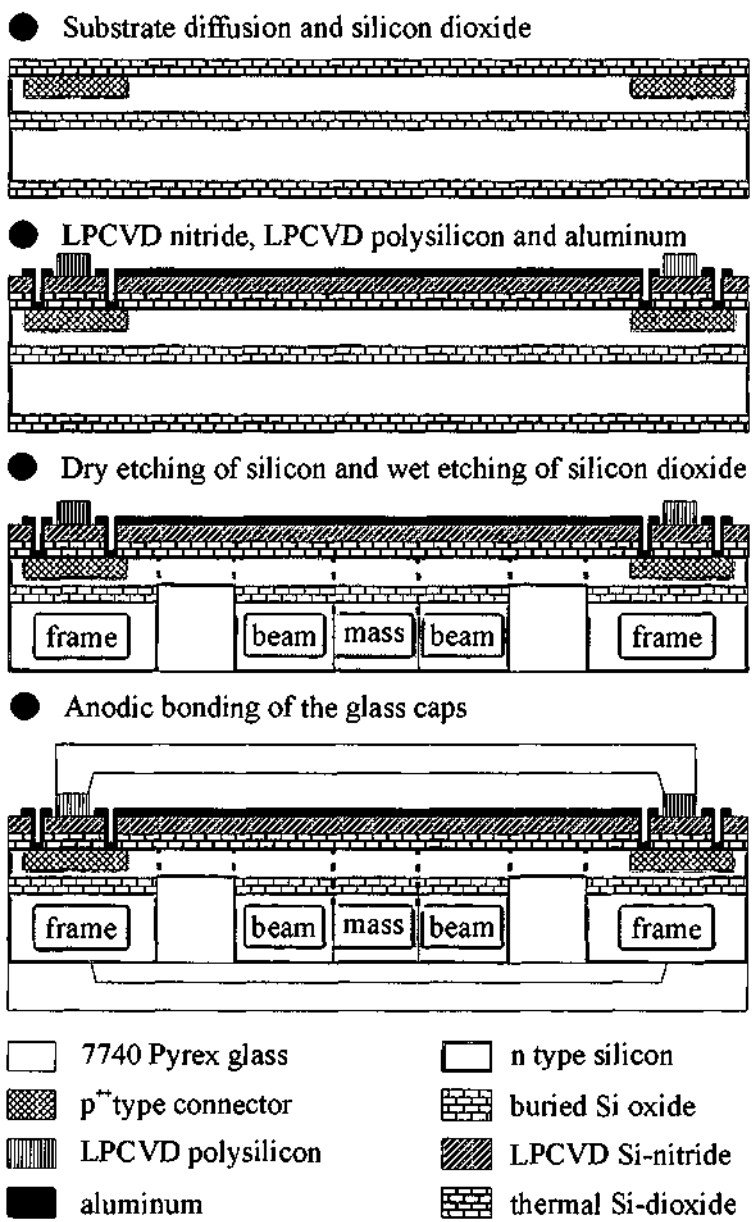

Figure 4.13: process cross-section for the suspension beams and the proof mass in the longitudinal direction.

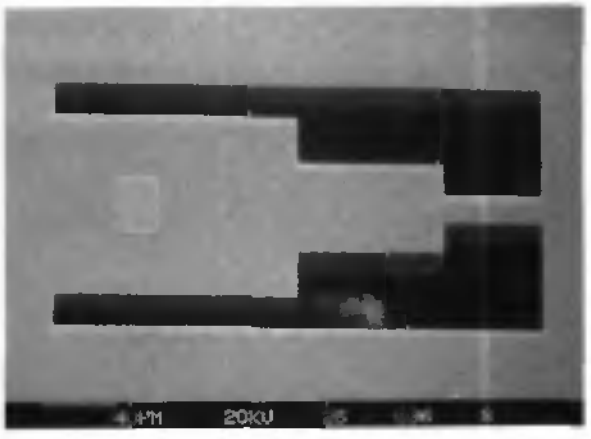

Figure 4.14: SEM picture of a pyramid (P) center part of a detection plate. The largest width (frame side) is 120 μm and the smallest one (beam side) is 20 μm. The detection plate thickness is 20 μm and its length 250 μm.

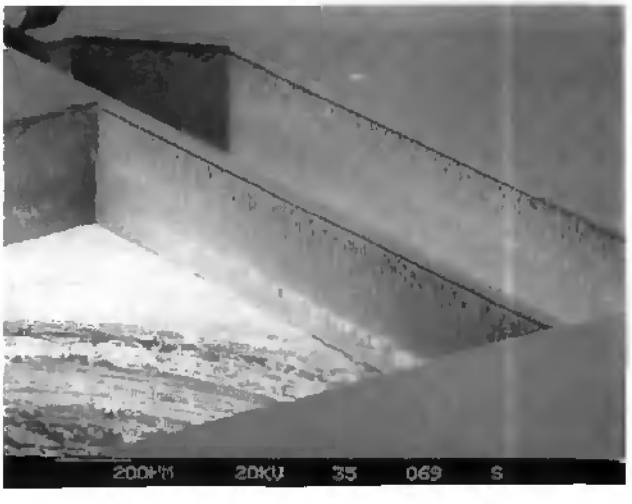

Figure 4.15: SEM picture of a suspension beam: 2000 μm long, 40 μm wide and 377 μm thick.

Process Step	Mask/Layer	Thickness
Phosphorus doped 4" SOI wafers		400 µm
Diamond marks		
Standard cleaning		
Positive photolithography	1:alignement	
Plasma etching	silicon	5000 Å
Resist stripping		
Standard cleaning		
Wet oxidation		4000 Å
Positive photolithography	2:SUBN+	
BHF [7:1] etching	silicon dioxide	4000 Å
Resist stripping		
CVD dioxide deposition		4000 Å
(phosphorus doped)		
Thermal anneal		
Standard diffusion		
BHF [7:1] etching	silicon dioxide	8000 Å
Wet oxidation		4000 Å
Positive photolithography	3:CONP+	
BHF [7:1] etching	silicon dioxide	4000 Å
Resist stripping		
CVD dioxide deposition		4000 Å
(boron doped)		
Thermal anneal		
Standard diffusion		
BHF [7:1] etching	silicon dioxide	8000 Å
Dry oxidation		700 Å
Positive photolithography	4:PIEZO	
Implantation (boron)		
Resist stripping		

Table 4.3: process schedule for the second prototype gyroscope (part 1).

Process Step	Mask/Layer	Thickness
BHF [7:1] etching	silicon dioxide	700 Å
Standard cleaning		
Dry oxidation		300 Å
Wet oxidation		350 Å
LPCVD silicon nitride deposition		2000 Å
LPCVD polysilicon deposition		5000 Å
Polysilicon standard diffusion		
Positive photolithography	5:polysilicon	
Plasma etching of both sides	polysilicon	5000 Å
Resist stripping		
Positive photolithography	6:contact opening	
Plasma etching of the front side	silicon nitride	2000 Å
BHF [7:1] etching	silicon dioxide	750 Å
Resist stripping		
Aluminium deposition		1 µm
Positive photolithography	7:metal	
Plasma etching	aluminium	1 µm
Resist stripping		
Aluminium anneal		
Plasma etching of the back side	silicon nitride	2000 Å
Positive photolithography	8:mass bottom	
Positive photolithography	9: mass top	
BHF [7:1] etching	silicon dioxide	700 Å
Deep plasma etching	silicon	400 µm
Resist stripping		
BHF [7:1] etching	silicon dioxide	1 µm
Cleaning for anodic bonding		
Anodic bonding		

Table 4.4: process schedule for the second prototype gyroscope (part2).

The two last steps in Table 4.4 are concerning the packaging of the prototype gyroscopes and are explained in more details in the following paragraph.

4.3.4 Packaging:

The encapsulation of the sensing elements was performed before chip dicing. This wafer scale packaging consists in the anodic bonding of two 500 µm thick Pyrex wafers (#7740 borosilicate glass) [4.41]. First the top glass wafer is bonded to the polysilicon frame to ensure a better electrical contact. Bonding glass with silicon nitride is possible but requires high bonding temperature and can increase the residual stress in the mechanical structure [4.42]. Then the bottom glass was directly bonded to the silicon.

Both glasses have to be micromachined to ensure an overrange protection of the seismic masses (chapter 3). 20 µm deep cavities are etched in the hydrofluoric acid (HF 50%) using a LPCVD polysilicon mask (5000 Å) [4.43]. Moreover the top glass was etched from the top side to produce a 380 µm deep cavity which reduces the distance between the magnet and the proof mass. Finally, the LPCVD polysilicon mask is removed in KOH (40%, 60°C) before the anodic bonding.

The anodic bonding is performed in a clean room environment to avoid any dust contamination at 400 °C and by applying a negative voltage on the glass wafer (800 V). To survive the saw cutting, a minimum bonded area width of 900 µm has been designed. More details about the bonding process as well as the dicing of the chips are described in chapter 3. Figure 4.16 and Figure 4.17 show a packaged prototype gyroscope from the top side and from the bottom side.

After the chips were diced, they were glued in an metallic housing (Figure 4.18). The permanent magnet (an axial rare earths and cobalt magnet Vacomax 225 HR) was suspended in the cavity by a metallic cap. It was not fixed to the chip to allow further observations of the gyroscope to be made. The metallic cap with the glued permanent magnet is held on to the metallic housing by four screws.

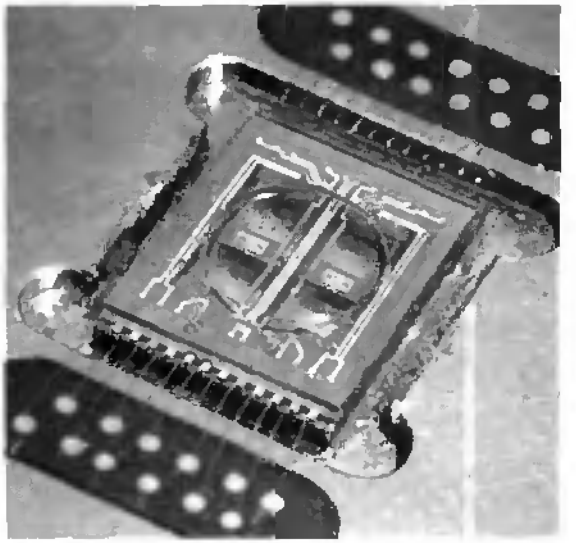

Figure 4.16: top view of a packaged prototype gyroscope glued in a metallic housing. The overall size of the chip is 12 mm long, 9 mm wide and 1.4 mm thick.

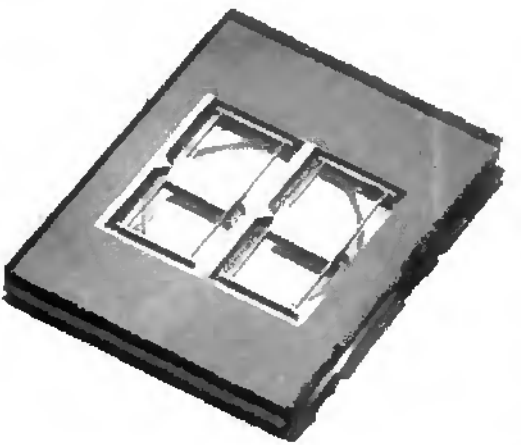

Figure 4.17: bottom view of a prototype gyroscope. The dark area is the bonded area

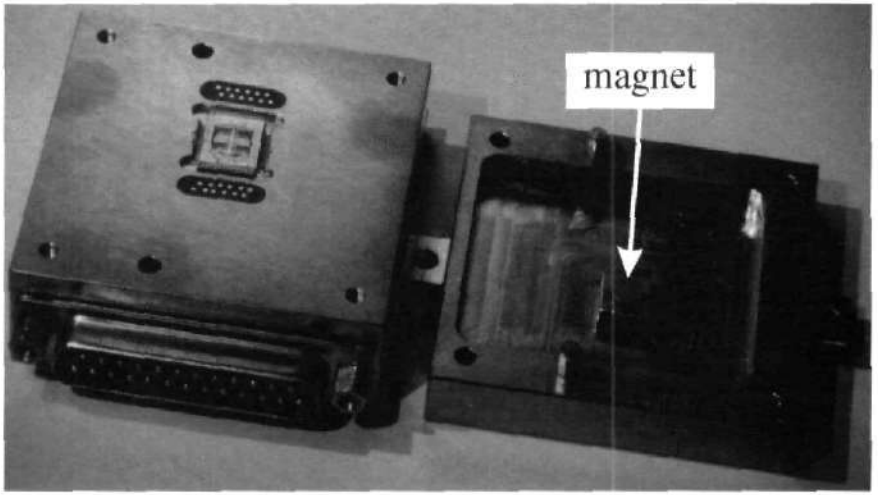

Figure 4.18: pictures of a packaged gyroscope and of a permanent magnet both in titanium housings.

4.4 Characterization:

4.4.1 Resonant frequency characterization:

First the prototype gyroscopes have been electrically tested without rotation. Figure 4.19 shows the measurement set-up. Each proof mass of the gyroscope can be separately driven. The Lorentz force is the result of the interaction of the AC current with a constant magnetic induction (B = 0.3 Tesla). The excitation resistors have been designed at 200 Ohm for all the gyroscopes, the piezoresistors at 2000 Ohm for the 250, 250B and 250P gyroscopes and at 3000 Ohm for the 500, 500B and 500P gyroscopes (Table 4.1).

A sinusoidal voltage is delivered by the lock-in amplifier and gives the reference for the phase sensitive detection as well as the excitation voltage. For each seismic mass, the driving amplitude can be measured by two piezoresistors, one located on the frame, which is fixed and the other at the edge of the detection plate (Figure 4.4).

By driving the seismic masses in antiphase, the two variable piezoresistors will vary the same way and can be combined into a Wheatstone bridge. This is possible thanks to the slight out of plane motion of the excitation mode and the external position of the piezoresistors. As already explained the driving mode is not a pure in plane translation but a small rocking effect is present which has been used for this purpose. The output signal is amplified by an instrumentation amplifier INA110 (Burr Brown) and is connected to the lock-in amplifier input. The amplitude of the driving forces (Lorentz forces) can be quantified with the above measurement set-up. Figure 4.20 shows the voltage amplitude versus the frequency for a 250P prototype gyroscope.

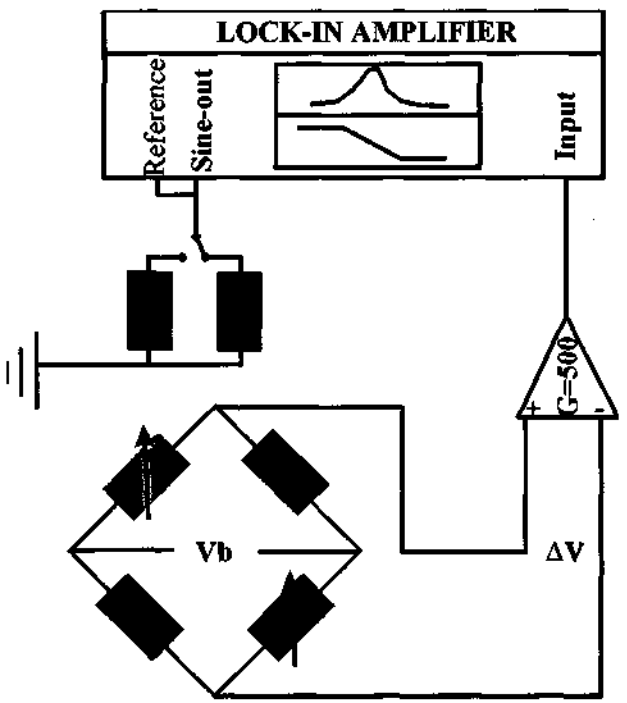

$$\Delta V = 1/2 * \Delta R/R * Vb$$

Figure 4.19: the measurement set-up for the resonant frequency characterization.

Each resonant peak corresponds to each mass. The frequency mismatch is 100 Hz and the amplitude mismatch is a 1:3 ratio due to the technology limits. As the homogeneity of the etching in the ADRIE tools is given with an error of ± 5% from the edge to the center of a wafer, the position of each sensor chip is of importance in its behavior [4.32]. For this prototype gyroscope located at the edge of the wafer, the suspension beams of one of the two proof masses were underetched. Thus the driving forces are less efficient for moving the proof mass (lower driving amplitude) and the resonance frequencies of the driving mode are not exactly the same (100 Hz frequency mismatch). To check that each resonant peak characterizes each seismic mass, the excitation was switched to drive separately each mass. This characteristics result in the plots of Figure 4.21 and Figure 4.22.

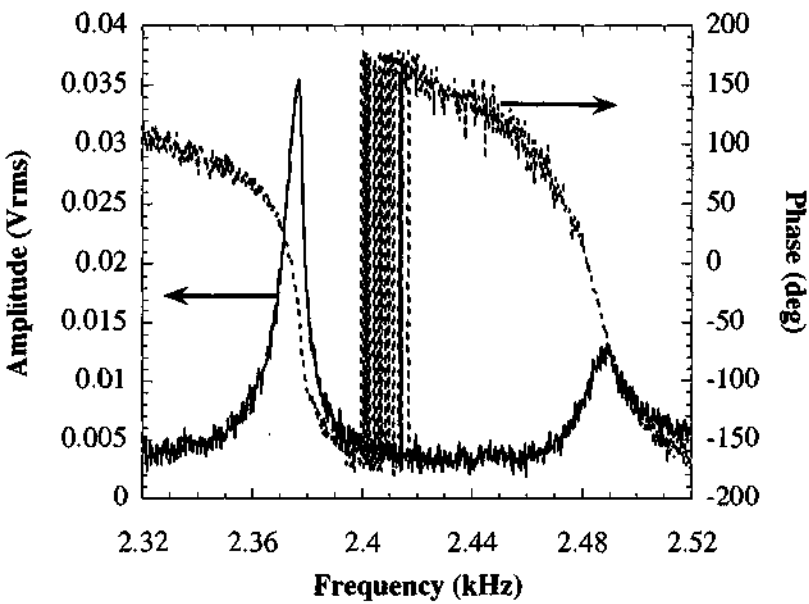

Figure 4.20: the driving amplitude and phase of a 250P prototype gyroscope. The AC excitation current amplitude is 9.6 mA and the magnetic induction is 0.3 Tesla. The amplification gain is 500.

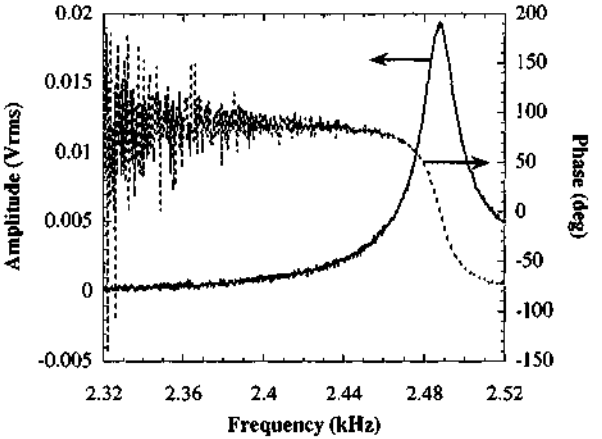

Figure 4.21: the driving amplitude for a 250 P prototype gyroscope when the right excitation resistor is disconnected (Figure 4.19). The AC excitation current amplitude is 9.6 mA and the magnetic induction is 0.3 Tesla. The amplification gain is 500.

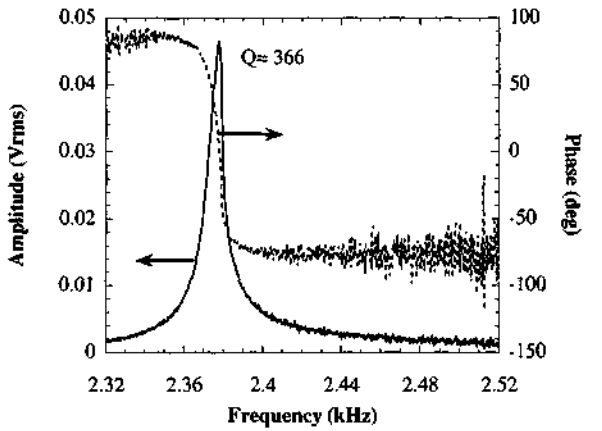

Figure 4.22: the driving amplitude for a 250 P prototype gyroscope when the left excitation resistor is disconnected.

For this prototype gyroscope (250P), the quality factor (Q) at - 3 dB was 366 with a vacuum packaging (Figure 4.22). The pressure during the anodic bonding was set at 1 µbar. For a 500B prototype gyroscope, the driving amplitude was measured by exciting the both masses (Figure 4.23). The measured quality factor at -3 dB was 185 with an air packaging. The two resonant frequencies are 10 Hz one from the other for this prototype gyroscope chosen at the center of a wafer.

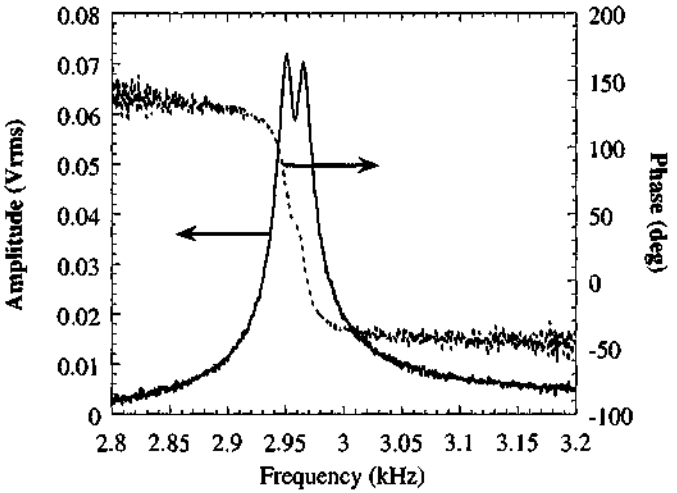

Figure 4.23: the driving amplitude for a 500 B prototype gyroscope versus the frequency. The AC excitation current amplitude is 8.8 mA and the magnetic induction is 0.3 Tesla. The amplification gain is 500.

4.4.2 Linearity of the excitation:

With the same prototype gyroscope (500B), the dependency of the resonant amplitude versus the excitation current has been investigated. In Figure 4.24, a linear variation has been measured as the Lorentz force is directly proportional to the driving current.

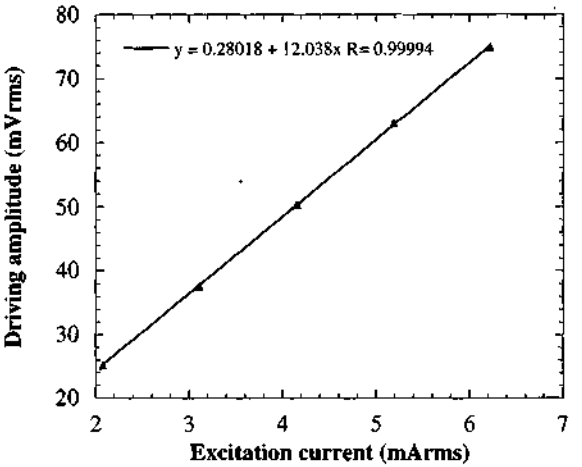

Figure 4.24: the linear dependency of the voltage amplitude at the driving port versus the excitation AC current for a 500B prototype gyroscope. The amplification gain is 500 and the magnetic induction is 0.3 Tesla.

4.4.3 Measurement of the temperature influence:

To perform the temperature measurements, the same set-up as for the previous characterization was employed but with a heater included in the metallic cap. This was realized with two warming resistors in contact with the metallic housing containing the gyroscope chip. The power supply of the heater is controlled by a calibrated platinum sensor (Pt 100) placed under the sensor chip. In Figure 4.25, the metallic cap including the heater is illustrated.

The temperature coefficient of the piezoresistor (TCR) was estimated by a temperature sensor designed on the frame near the detection path (Figure 4.4). The measured TCR was 870 ppm/K. The sensing piezoresistor could not be characterized because it was not possible to separate the temperature effect from the stress effect [4.5]. These temperature effects are well-known drawback for piezoresistor detection and can be compensated by appropriate active or passive electronics [4.44, 4.45, 4.46]. With a 250 P prototype gyroscope, the same measurement of the driving amplitude versus the excitation frequency is performed. Figure 4.26 illustrates the resonant curves obtained for several temperatures. By increasing the temperature, the resonant peaks are shifted to higher frequencies and the resonant amplitudes become smaller. This temperature dependence is not negligible and can be simulated with a FEM analysis of the gyroscope including the packaging. With Memcad™, the static bending at ambient temperature (20°C) was simulated for a gyroscope bonded at 400°C [4.47]. This static bending is due to the mismatch of the thermal expansion coefficients (TCE) of the silicon and the glass [4.42, 4.43, 4.48].

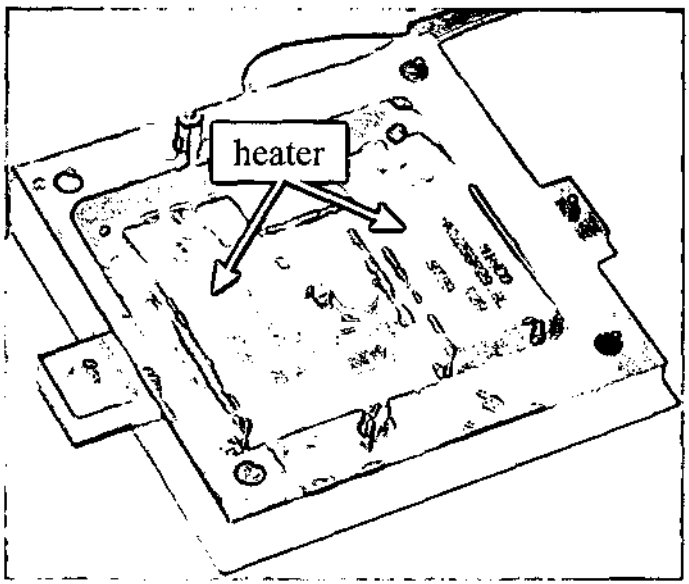

Figure 4.25: the metallic cap including the magnet and the heaters for the temperature measurements.

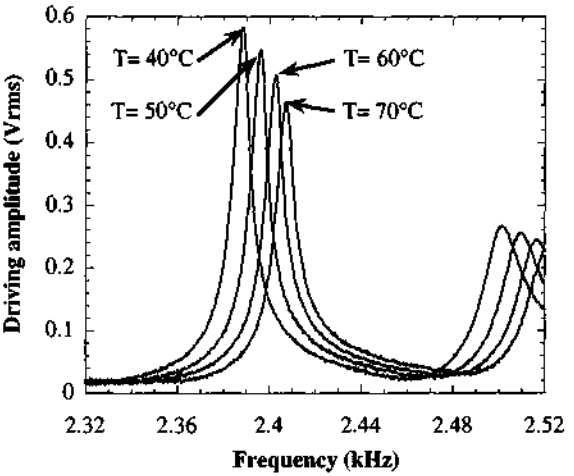

Figure 4.26: the driving amplitude of a 250P prototype gyroscope for several temperatures. The AC excitation current amplitude is 3 mA and the magnetic induction is 0.3 Tesla. The amplification gain is 15610.

With a sample line, the static displacement along the longitudinal axis of the package gyroscope on the bottom face of the bottom glass cap can be displayed. This simulated static displacement along a symmetric axis of the gyroscope has been compared with the static deflection at 20°C of the bottom glass surface along the same axis measured by an optical profilometer (UBM) and both curves agree very well (Figure 4.27). The same simulation has been performed for several temperatures and this static bending has been applied to the FEM model of the gyroscope before calculating the first resonant frequency. Figure 4.28 illustrates the first resonant frequency shift for both the simulation and the measurements for several temperatures ranging from 35°C to 70°C. The simulation and the measurements are in good agreement with less than 1% of error.

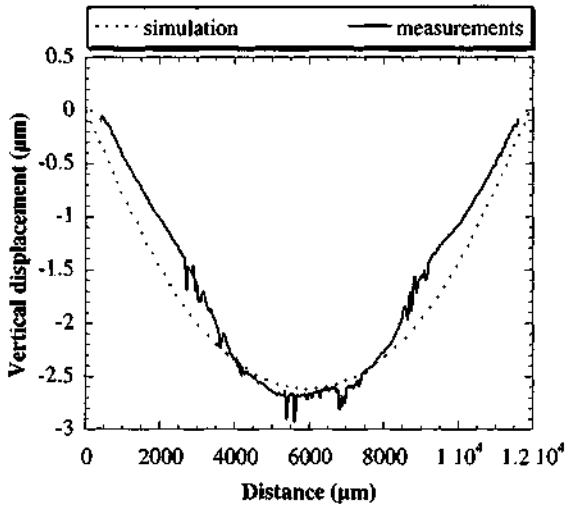

Figure 4.27: the static deflection of a 250P gyroscope simulated and measured at 20°C along a longitudinal axis on the bottom glass surface.

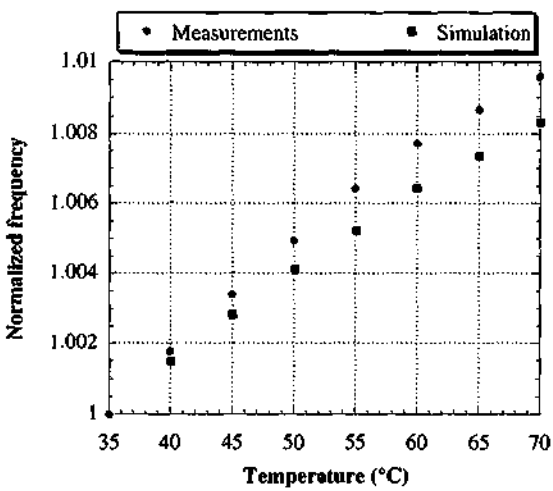

Figure 4.28: the first resonant frequency shift versus the temperature for a 250P gyroscope simulated and measured at 20°C along a longitudinal axis on the bottom glass surface.

4.4.4 Rotation measurements:

The rotating table is a one axis table (model DC 120 Acutronic S.A) with a maximum velocity of 1000 deg/sec and a resolution of 0.0001 deg/sec. To perform the angular rate characterization, both the prototype gyroscope and its electronic are placed on the rotating table. With the previous design, the gyroscope has to be driven 100 Hz before its first resonant frequency and needed to be stabilized with a bias current at the excitation [4.4]. For each rotation rate, the zero rate output value was subtracted because it was slightly changing with time and the time constant of the lock-in amplifier has to be fixed at 3 sec.

With the new design, the gyroscope prototypes are operated by fixing the excitation frequency to the first resonant frequency. No further bias current has to be added at the driving part. Two gyroscopes (500B and 250P), which have been already characterized in a previous paragraph, were successfully tested (Figure 4.20, Figure 4.23). Figure 4.29 illustrates the gyroscope outputs versus the angular rate. Both prototype gyroscopes show excellent linearity. A sensitivity of 1.2 nV/deg/sec is obtained with the 500B prototype gyroscope compared with 0.8 nV/deg/sec for the 250P prototype gyroscope. This higher sensitivity corresponds to the longer detection plate (500 μm for the 500B design and 250 μm for the 250P).

Moreover, the time constant of the lock-in amplifier can be reduced to 100 ms. Thus the new design gyroscope bandwidth is 10 Hz , which represents an improvement by 30 times [4.4]. Within the 10 Hz bandwidth, the minimum angular rate is measured at 50 deg/sec for both prototype gyroscopes, although a 20 deg/sec angular rate was also detected with a 1 Hz bandwidth.

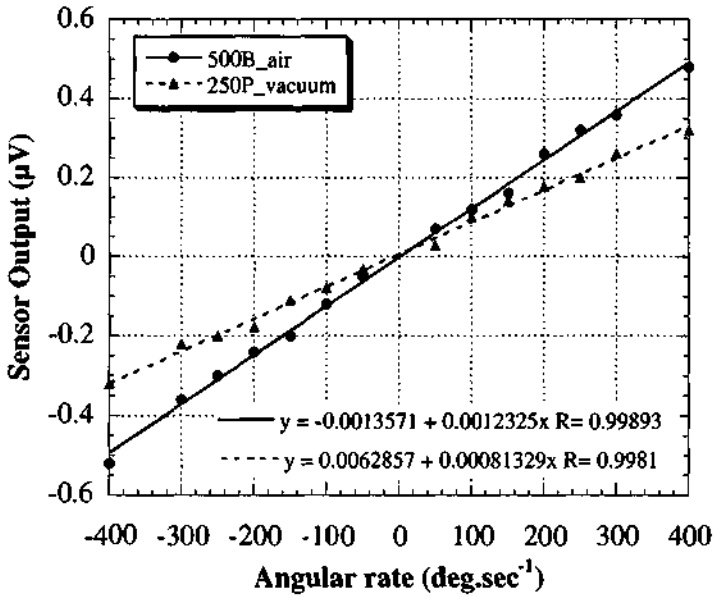

Figure 4.29: the outputs of two prototype gyroscopes (500B and 250P) for several angular rates. The AC excitation current amplitude is 6 mA, the magnetic induction is 0.3 Tesla and the amplification gain is 500.

The minimal angular rate was decreased by changing the measurement bandwidth. As the angular rate resolution is limited essentially by the noise level, we estimated the thermal noise level versus the measurement bandwidth and compared it with the experimental noise level for a fixed angular rate (200 deg/sec) (Figure 4.30). The thermal noise level for one piezoresistor can be roughly estimated by the following equation:

$$v = \sqrt{4 * k * T * R * \Delta f} \qquad [4.49]$$

with: v noise level (V) — 4.k.T (23°C) = $1.66\ 10^{-20}$ C.V

R = 3000 ohm — Δf bandwidth

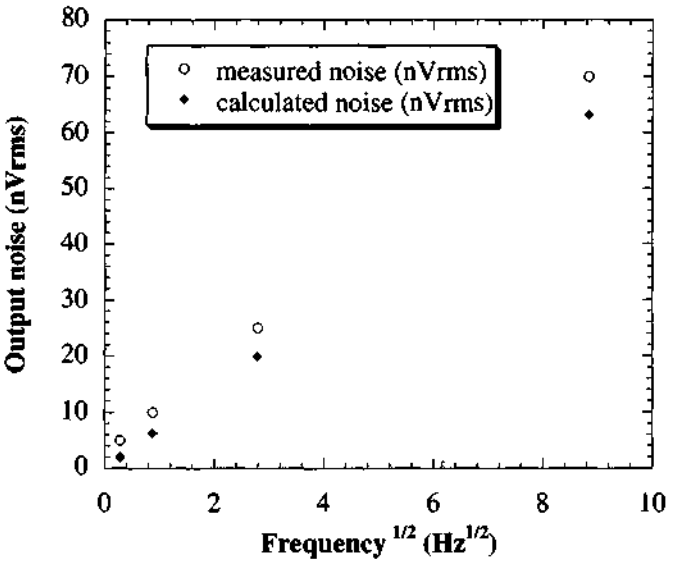

Figure 4.30: comparison between the measured and calculated noise levels for a sensing piezoresistor of a 500 B gyroscope prototype.

The previous noise level is depending from the chosen bandwidth and defines the resolution. The latter depends from the white noise and can be expressed in terms of the standard deviation of equivalent rotation rate per square root of bandwidth of detection [deg/sec/ √Hz]. This is the angle random walk in [deg/ √sec] [4.50, 4.51]. From the previous graph, we can calculate the slope of the noise level versus the square rate of the bandwidth and the calculated random walk is 4 deg/√sec for the 500B prototype gyroscope.

4.4.5 Long term measurements:

Due to the chosen application domain namely, a navigation microsystem, the long term drift of the gyroscope should be characterized [4.51, 4.52]. With the new design, the stability of the angular rate sensor output has been improved but for long term measurements, an important drift was still observed. Figure 4.31 illustrates the sensor output for the 500B prototype gyroscope in two cases.

First the excitation frequency was fixed at the driving resonant frequency (open loop) and secondly the excitation frequency was locked by a PLL (Phase locked Loop) electronic to the driving resonant frequency (closed loop). The comparison of both curves shows how the effect of the PLL control on the driving mode frequency reduces the long term drift of the prototype gyroscope [4.53, 4.54, 4.55].

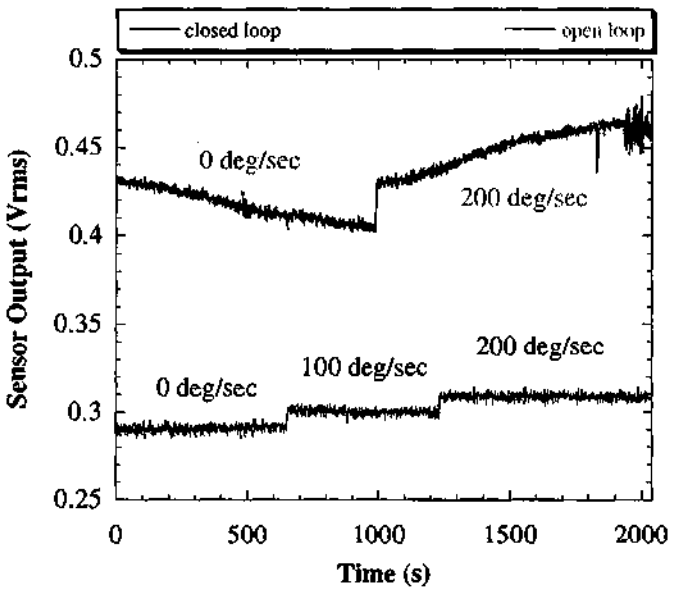

Figure 4.31: the output voltage for a 500B prototype gyroscope, versus the time for two configurations: closed loop and open loop. The magnetic induction is 0.3 Tesla, the driving AC current amplitudes are 4.1 mA (closed loop) and 5.9 mA (open loop) and the amplification gain is 500.

4.5 Conclusion:

A new design of a silicon micromachined gyroscope has been successfully tested. Temperature, rotation and long term measurements have been realised to give an overview of its performances. A sensitivity of 1.2nV/deg/sec has been measured and all tested prototype gyroscopes showed an excellent linearity. A minimum angular rate of 20 deg/sec was measured and a 10 Hz bandwidth was obtained. With an improved electronics, closed loop excitation of the prototype gyroscope displayed promising results.

The main novelty in this new gyroscope design consists in a better stability of the sensor output. A higher symmetry of the device reduced the mechanical cross coupling, which induced a large output without any rotation. The proof mass and the suspension beams are at identical thickness. The separation of the resonant frequency of the first mode (excitation) from the resonant frequency of the second mode (vertical motion) allowed the driving and sensing of the rotation rate to be made at the same frequency (resonant frequency of the first mode) without including large parasitic vibrations due to the second mode. The cross section of the suspension beams was not square but had a high aspect ratio of 1:10. Finally the better performances stemmed not only from the improved concept but also from the control electronics and both were designed simultaneously.

4.6 References:

[4.1] C. Song, "Commercial vision of silicon based inertial sensors", Digest of Technical Papers, International Conference on Solid-State Sensors and Actuators, Transducers'97, Chicago IL, June 16-19, 1997, pp. 839-841.

[4.2] R. H. Grace, "Automotive applications of microelectromechanical systems (MEMS)", Proceedings Sensors Expo Anaheim, Anaheim, CA, April 1996, pp. 133-141.

[4.3] R. Voss, "Silicon micromachined vibrating gyroscopes", Proceedings of the SPIE 1997 Conference: Micromachined Devices and Components III, Austin, TX, September 1997, pp. 62-73.

[4.4] F. Paoletti, M.-A. Grétillat and N. F de Rooij, "A Silicon Micromachined Vibrating Gyroscope with Piezoresistive Detection and Electromagnetic Excitation", Proceedings of the 9th IEEE Workshop on Micro Electro Mechanical Systems, MEMS '96, San Diego, CA, February 1996, pp. 162-167.

[4.5] F. Paoletti, M.-A. Grétillat and N. F de Rooij, "A Silicon Micromachined Tuning Fork Gyroscope", Proceedings of Symposium Gyro Technology 1996, Stuttgart, Germany, September 1996, pp. 5.0-5.8.

[4.6] C. Marselli, H.P. Amann, F. Pellandini, F. Paoletti, M.-A. Grétillat and N. F de Rooij, "Error Modelling of a Silicon Angular Rate Sensor", Proceedings of Symposium Gyro Technology 1997, Stuttgart, Germany, September 1997, pp. 4.0-4.9.

[4.7] N. Wakatsuki, S. Kudo, H. Tanaka, O. Masaaki, S. Yamada, K. Kikuchi and M. Yamauchi, "Improvement of piezoelectric vibratory gyroscope using LiTaO3 crystal", Proceedings of Symposium Gyro Technology 1996, Stuttgart, Germany, September 1996, 6.0-6.11.

[4.8] W. Geiger, B. Folkmer, J. Merz, H. Sandmaier and W. Lang, "A new silicon rate gyroscope", Proceedings of the 11th IEEE Workshop on Micro Electro Mechanical Systems, MEMS'98, Heidelberg, Germany, January 1998, pp. 615-620.

[4.9] K. Tanaka, Y. Mochida, S. Sugimoto, K. Moriya, T. Hasegawa, K. Atsuchi and K. Ohwada, "A micromachined vibrating gyroscope", Sensors & Actuators A - Physical, A 50, 1995, pp. 56-60.

[4.10] J. Söderkvist, "Micromachined vibrating gyroscopes", Digest of Technical Papers of the 7th International Conference on Solid-State Sensors and Actuators, Transducers'93, Yokohama, Japan, June 1993, pp. 638-641.

[4.11] J. Bernstein, S. Cho, A. T. King, A. Kourepenis, P. Maciel and M. Weinberg, "A micromachined comb-drive tuning fork rate gyroscope", Proceedings of the 6th IEEE Workshop on Micro Electro Mechanical Systems, MEMS '93, Fort Lauderdale, FL, February 1993, pp. 143-148.

[4.12] J. Choi, K. Minami and M. Esashi, "Silicon angular rate sensor by deep reactive ion etching", Proceedings of the International Symposium on Microsystems, Intelligent Materials and Robots, Sendai, Japan, September 1995, pp. 29-32.

[4.13] W. A. Clark, R. Horowitz and R. T. Howe, "Surface micromachined Z-axis vibratory rate gyroscope", Technical Digest of IEEE Solid-State Sensor and Actuator Workshop, Hilton Head Island, SC, June 1996, pp. 283-287.

[4.14] B. Kloeck, "Design, fabrication and characterization of piezoresistive pressure sensor, including the study of electrochemical etch-stop", Ph. D. dissertation, Institute of Microtechnology, University of Neuchâtel, Switzerland (1989).

[4.15] T. Tschan, "Simulation, design and characterization of a piezoresistive accelerometer fabricated by a bipolar-compatible industrial process", Ph.D.dissertation, Institute of Microtechnology, University of Neuchâtel, Switzerland (1992).

[4.16] R.-A. Buser, "Theoretical and experimental investigations on silicon single crystal resonant structures", Ph. D. dissertation, Institute of Microtechnology, University of Neuchâtel, Switzerland (1989).

[4.17] Y. Ansel, B. Romanowicz, Ph Lerch and Ph. Renaud, "Optimisation of a vibrating gyroscope by a system level simulation", Proceedings of the 10th European Conference on Solid-State Transducers, Eurosensor X, Leuven, Belgium, September 1996, pp. 1245-1248.

[4,18] S. G. Kelly, "Fundamentals of mechanical vibrations", edited by McGraw-Hill Inc., 1993.

[4.19] H. Kuisma, T. Ryhänen, J. Lahdenperä, E. Punkka, S. Ruotsalainen, T. Sillanpää and H. Seppä, "A bulk micromachined silicon angular rate sensor", Digest of Technical Papers of the 9th International Conference on Solid-State Sensors and Actuators, Transducers '97, Chicago IL, June 1997, pp. 875-878.

[4.20] R. T. Howe, B. E. Boser and A. P. Pisano, "Polysilicon integrated microsystems: technologies and applications", Sensors & Actuators A - Physical, A 56 (1996), pp. 167-177.

[4.21] C. Linder, L. Paratte, M.-A. Grétillat, V. P. Jaecklin and N. F. de Rooij, "Surface micromachining", Journal of Micromechanics and Microengineering, Vol. 2(1992), pp. 122-132.

[4.22] "Microsensors", IEEE Press, Edited by R. S. Muller, R. T. Howe, S. D. Senturia, R. L. Smith and R. M. White, New York, 1991.

[4.23] "Mechanical Sensors", Sensors-A Comprehensive Survey, Edited by H. H. Bau, N. F. de Rooij and B. Kloeck, Weinheim, Vol. 7, 1994.

[4.24] C. Linder, T. Tschan and N. F. de Rooij, "Deep dry etching of silicon: a novel micromachining tool", Sensors and Materials, Vol.3 N°. 6 1992, pp. 311-324.

[4.25] K. Y. Lee, H. LaBianca and S. A. Rishton, "Micromachining applications of a high resolution ultrathick photoresist", Journal of Vacuum Science & Technology B, Vol. 13 N°. 6 1995, pp. 3012-3016.

[4.26] M. Esashi, "High-rate directional deep dry etching for bulk silicon micromachining", Journal of Micromechanics & Microengineering, Vol. 5 1995, pp. 5-10.

[4.27] T. Goto, K. Matsushita and K. Hirono, "Three-dimensional microfabrication of single-crystal silicon by plasma etching", Ieice Transactions on Electronics, Vol. E78-C N°. 2 1995, pp. 167-173.

[4.28] H. Jansen, M. de Boer and M. Elwenspoek, "The black silicon method VI: high aspect ratio trench etching for MEMS applications", Proceedings of the 9th IEEE Workshop on Micro Electro Mechanical Systems, MEMS '96, San Diego, CA, February 1996, pp. 250-257.

[4.29] J. W. Rangelow and H. Löschner, "Reactive ion etching for microelectrical mechanical system fabrication", Journal of Vacuum Science & Technology B, Vol. 13 N°. 6 1995, pp. 2394-2399.

[4.30] VA. Yunkin, VF. Lukichev, KV. Rudenko, D. Fischer and E. Voges, "Experimental study and computer simulation of aspect ratio dependent effects observed in silicon reactive ion etching", Microelectronic Engineering, Vol. 30 N°. 1-4 1996, pp. 345-348.

[4.31] BAM. Andersen, O. Hansen and M. Kristesen, "Spatial variation of the etch rate for deep etching of silicon by reactive ion etching", Journal of Vacuum Science & Technology B, Vol. 15 N°. 4 1997, pp. 993-999.

[4.32] J. K. Bhardwaj and H. Ashraf, "Advanced silicon etching using high density plasmas", Proceedings of the SPIE 1995 Conference: Micromachining and Microfabrication Process Technology, Austin, TX, October 1995, pp. 224-233.

[4.33] J. W. Bartha, J. Greschner, M. Puech and P. Maquin, "Low temperature etching of Si in high density plasma using SF6/O2", Microelectronic Engineering, Vol. 27 1995, pp. 453-456.

[4.34] A. A. Ayon, C. C. Lin, R. A. Braff and M. A. Schmidt, "Etching characteristics and profile control in a time multiplexed inductively coupled plasma etcher", Technical Digest of IEEE Solid-State Sensor and Actuator Workshop, Hilton Head Island, SC, June 1998, pp. 41-44.

[4.35] S. Coward and D. Matthews, "ZASE advances MEMS technology", MST news international activities in microsystem technology, Vol 20 1997, pp. 23.

[4.36] E. H. Klaasen, K. Petersen, J. M. Noworolski, J. Logan, N. I. Maluf, J. Brown, C. Storment, W. McCulley and G. T. A. Kovacs, "Silicon fusion bonding and deep reactive ion etching: a new technology for microstructures", Sensors & Actuators A - Physical, A 52 (1996), pp. 132-139.

[4.37] A. Olsson, P. Enoksson, G. Stemme and E. Stemme, "Micromachined flat-walled valveless diffuser pumps", Journal of Microelectromechanical Systems, Vol. 6 N°. 2 1997, pp. 161-166.

[4.38] P. -A. Clerc, L. Dellmann, F. Grétillat, M. -A. Grétillat, P. -F. Indermühle, S. Jeanneret, Ph. Luginbuhl, C. Marxer, T. L. Pfeffer, G. -A. Racine, S. Roth, U. Staufer, C. Stebler, P. Thiébaud and N. F. de Rooij, "Advanced deep reactive ion etching a versatile tool for microelectromechanical systems", accepted for publication in the Journal of Microelectronics and Microengineering (JMM/95864/PAP).

[4.39] H. E. Elgamel, "Close-form expressions for the relationships between stress, diaphragm deflection, and resistance change with pressure in silicon piezoresistive pressure sensors", Sensors & Actuators A - Physical, A 50 (1995), pp. 17-22.

[4.40] S. M. SZE, "Semiconductor devices physics and technology", edited by John Wiley & Sons, 1985.

[4.41] Data sheet: Corning 7740 borosilicate Pyrex®, Corning Keramik GMBH & CO., Abraham-Lincoln Strasse 30, D-65189 Wiesbaden, Germany.

[4.42] S. Shoji and M. Esashi, "Bonding and Assembling Methods for Realising a μTAS", Proceedings of Miniaturized Total Analysis Systems, μ-TAS94, Twente, The Netherlands, November 1994, pp. 165-179.

[4.43] M.-A Grétillat, F. Paoletti, P. Thiébaud, S. Roth, M. Koudelka-Hep and N.F. de Rooij, "A New Fabrication Method for Borosilicate Glass Capillary Tubes with Lateral Inlets and Outlets", Sensors & Actuators, A 60, 1997, pp. 219-222.

[4.44] J. Gakkestad, P. Ohlckers and L. Halbo, "Effects of process variations in a CMOS circuit for temperature compensation of piezoresistive pressure sensors", Sensors & Actuators A - Physical, A 48 (1995), pp. 63-71.

[4.45] C. Berthoud, M. Ansorge and F. Pellandini , "Effective static response compensation suitable for low-power ASIC implementation with an application to pressure sensors", Proceedings of the IEEE Instrumentation and Measurement Technology Conference, Brussels, Belgium, June 1996, pp. 1168-1173.

[4.46] E. Perraud, "Theoretical model of performance of a silicon piezoresistive pressure sensor", Sensors & Actuators A - Physical, A 57 (1996), pp. 245-252.

[4.47] MICROCOSM, software solutions for MEMS design, 201 Willesden Drive, Cary, NC 27513, davec@memcad.com.

[4.48] Data sheet: Corning 7740 borosilicate Pyrex®, Corning Keramik GMBH & Co., Abraham-Lincoln Strasse 30, D-65189 Wiesbaden, Germany.

[4.49] S. D. Senturia, M. A. Schmidt, Harrison, "Microsystems: mechanical, chemical, optical", Chapter 16, July 1997, pp. 16-21.

[4.50] N. Yazdi, F. Ayazi, K. Najafi, "Micromachined inertial sensors", Proceedings of the IEEE, special issue: integrated sensors, microactuators and microsystems (MEMS), Vol. 86 N°. 8, August 1998, pp. 1640-1659.

[4.51] A. Lawrence, "Modern inertial technology", Springer-Verlag New York Inc., 1993.

[4.52] S. Oho, H. Kajioka, T. Sasayama, "Optical fiber gyroscope for automotive navigation", IEEE Transactions on vehicular technology, Vol. 44 N° 3, August 1995, pp. 698-705.

[4.53] R. Best, "Theorie und Anwedung des Phase Locked Loops" edited by VDE Stuttgart.

[4.54] S. An, Y. S. Oh, B. L. Lee, K. Y. Park, S. J. Kang, S. O. Choi, Y. I. Go and C. M. Song, "Dual-axis microgyroscope with closed-loop detection", Proceedings of the 11th IEEE Workshop on Micro Electro Mechanical Systems, MEMS'98, Heidelberg, Germany, January 1998, pp. 328-333.

[4.55] M. Lutz, W. Golderer, J. Gerstenmeier, J. Marek, B. Maihöfer, S. Mahler, H. Münzel and U. Bischof, "A precision yaw rate sensor in silicon micromachining", Digest of Technical Papers of the 9th International Conference on Solid-State Sensors and Actuators, Transducers '97, Chicago, IL, June 1997, pp. 847-850.

5. Conclusion

5.1 Introduction:

This conclusion will summarizes the work which was done from 1994 to 1998 during this Ph.D. Thesis focusing on the design, the realization and the characterization of two prototype gyroscopes. Chapter 1 explains the principle of a silicon vibrating gyroscope, as well as, the chosen principles of excitation and detection (respectively electromagnetic and piezoresistive). Chapter 3 points out the importance of a technical step: the packaging. Chapters 2 & 4 give a detailed description of the design, the fabrication and the characterization of the two prototype gyroscopes.

Before giving the conclusions and the outlooks of this work, the comparison of the realized devices with other angular rate sensors is presented to place this work in an wider framework. Performance characteristics of commercial gyroscopes have been already listed and only gyroscopes presented in conferences or in scientific publications will be referred [5.1].

5.2 Comparison with other devices:

From 1991 to 1998, several gyroscopes have been presented and their main characteristics are compared with the sensors realized in this Ph.D. thesis. We choose the following parameters: the number of sensing axes, the design, the excitation and detection principles, the range, the sensitivity, the resolution and the bandwidth. Only one 3 axes gyroscope [5.19] and three 2 axes gyroscopes [5.16, 5.22, 5.33] were reported. Considering the gyroscope design, the tuning fork (t.n) design was chosen 9 times [5.5, 5.6, 5.7, 5.9, 5.17, 5.18, 5.19, 5.21, 5.30], as well as, the 1 accelerometer (1 acc) design [5.3, 5.12, 5.15, 5.16, 5.24, 5.26, 5.27, 5.29, 5.35] then the 2 accelerometers (2 acc) design 7 times [5.4, 5.10, 5.11, 5.12, 5.20, 5.22, 5.23, 5.25] and the vibrating shell (v.s) design 6 times [5.7, 5.22, 5.27, 5.31, 5.33, 5.34]. These designs are explained in chapter 1.

Table 5-1: main characteristics of some prototypes gyroscopes.

	[5.2]	[5.3]	[5.4]	[5.5]	[5.6]	[5.7]	*Units*
Year	1991	1991	1993	1993	1993	1993	*year*
Axes	1	1	1	1	1	1	*nb*
Design	bar	1 acc	2 acc	t.n	t.n	t.n	
Excitation	pe	es	es	pe	pe	pe	
Detection	pe	c	c	pe	c	pe	
Material	metal	silicon	polySi	quartz	silicon	quartz	
Range	±150	NA	±270	±50	±1000	±400	*deg/sec*
Sensitivity	33mV	NA	1.57mV	5µV	0.35mV	50pA	
Resolution	30	4	0.19	0.1	5.7	0.1	*deg/sec*
Bandwidth	NA	1	1	NA	NA	40	*Hz*

1 acc: 1 accelerometer
2 acc: 2 accelerometers
bm: bimorph
c: capacitive
em: electromagnetic
es: electrostatic
FOG: fiber optic gyroscope
l: light
pe: piezoelectric
pr: piezoresistive
polySi: polysilicon
s.e: sagnac effect
v.s: vibrating shell
N.A: not available
fq: frequency
t.n: tuning fork

Table 5-2: main characteristics of some prototypes gyroscopes

	[5.8]	[5.9]	[5.10]	[5.11]	[5.12]	[5.13]	*Units*
Year	1994	1994	1995	1995	1995	1995	*year*
Axes	1	1	1	1	1	1	*nb*
Design	v.s	t.n	2 acc	2 acc	1 acc	s.e	
Excitation	es	pe	em	es	es	l	
Detection	c	pe	c	c	c	fq	
Material	nickel	metal	silicon	silicon	polySi	FOG	
Range	NA	±100	±400	±1000	±100	±60	*deg/sec*
Sensitivity	NA	0.38	6fF	0.73fF	NA	NA	
Resolution	0.5	10	50	500	2	0.01	*deg/sec*
Bandwidth	10	NA	NA	NA	NA	NA	*Hz*

1 acc: 1 accelerometer
2 acc: 2 accelerometers
bm: bimorph
c: capacitive
em: electromagnetic
es: electrostatic
FOG: fiber optic gyroscope
l: light
pe: piezoelectric
pr: piezoresistive
polySi: polysilicon
s.e: sagnac effect
v.s: vibrating shell
N.A: not available
fq: frequency
t.n: tuning fork

Table 5-3: main characteristics of some prototype gyroscopes.

	[5.14]	[5.15]	[5.16]	[5.17]	[5.18]	[5.19]	*Units*
Year	1996	1996	1996	1996	1996	1996	*year*
Axes	1	1	2	1	1	3	*nb*
Design	2 acc	1 acc	1 acc	t.n	t.n	t.n	
Excitation	es	es	es	pe	pe	pe	
Detection	c	c	c	pe	c	pe	
Material	polySi	silicon	polySi	metal	silicon	$LiTaO_3$	
Range	NA	±300	±100	±100	±500	±300	*deg/sec*
Sensitivity	NA	15μV	2mV	NA	100μV	0.5mV	
Resolution	1	15	1.2	0.01	3	NA	*deg/sec*
Bandwidth	1	100	25	100	30	NA	*Hz*

1 acc: 1 accelerometer
2 acc: 2 accelerometers
bm: bimorph
c: capacitive
em: electromagnetic
es: electrostatic
FOG: fiber optic gyroscope
l: light
pe: piezoelectric
pr: piezoresistive
polySi: polysilicon
s.e: sagnac effect
v.s: vibrating shell
N.A: not available
fq: frequency
t.n: tuning fork

Table 5-4: main characteristics of some prototypes gyroscopes.

	[5.20]	[5.21]	**Thesis Chap. 2**	[5.22]	[5.23]	[5.24]	*Units*
Year	1996	1996	**1996**	1997	1997	1997	*year*
Axes	1	1	**1**	2	1	1	*nb*
Design	2 acc	t.n	**2 acc**	2 acc	v.s	1 acc	
Excitation	es	es	**em**	bm	em	es	
Detection	c	c	**pr**	c	em	c	
Material	silicon	silicon	**silicon**	nickel	silicon	silicon	
Range	±500	±1000	**±400**	±1000	±100	±300	*deg/sec*
Sensitivity	NA	0.75mV	**4nV**	1.74μV	20mV	NA	
Resolution	0.04	NA	**20**	180	0.15	1	*deg/sec*
Bandwidth	60	NA	**0.33**	NA	30	100	*Hz*

1 acc: 1 accelerometer
2 acc: 2 accelerometers
bm: bimorph
c: capacitive
em: electromagnetic
es: electrostatic
FOG: fiber optic gyroscope
l: light
pe: piezoelectric
pr: piezoresistive
polySi: polysilicon
s.e: sagnac effect
v.s: vibrating shell
N.A: not available
fq: frequency
t.n: tuning fork

Table 5-5: main characteristics of some prototype gyroscopes.

	[5.25]	[5.26]	[5.27]	[5.28]	[5.29]	[5.30]	[5.31]
Year	1997	1997	1997	1997	1997	1997	1997
Axes	1	1	1	1	1	1	1
Design	2 acc	1 acc	1 acc	v.s	1 acc	t.n	t.n
Excitation	em	es	es	es	es	pe	pe
Detection	c	c	c	c	c	pe	pr
Material	silicon	polySi	polySi	nickel	silicon	quartz	silicon
Range	±100	±100	±90	±100	±1000	±100	±1000
Sensitivity	18mV	125µV	NA	0.1V	24mV	19µV	250µV
Resolution	0.5	0.1	0.1	0.5	0.02	10	NA
Bandwidth	NA	4	NA	25	NA	NA	NA

1 acc: 1 accelerometer
2 acc: 2 accelerometers
bm: bimorph
c: capacitive
em: electromagnetic
es: electrostatic
FOG: fiber optic gyroscope
l: light
pe: piezoelectric
pr: piezoresistive
polySi: polysilicon
s.e: sagnac effect
v.s: vibrating shell
N.A: not available
fq: frequency
t.n: tuning fork

Table 5-6: main characteristics of some prototype gyroscopes.

	[5.32]	[5.33]	[5.34]	[5.35]	[5.36]	**Thesis Chap. 4**	*Units*
Year	1997	1998	1998	1998	1998	**1998**	*year*
Axes	1	1	2	1	1	**1**	*nb*
Design	s.e	v.s	v.s	v.s	1 acc	**2 acc**	
Excitation	l	es	es	es	pe	**em**	
Detection	pd	c	c	c	c	**pr**	
Material	silicon	polySi	polySi	silicon	silicon	**silicon**	
Range	±800		NA	±200	±200	**±400**	*deg/sec*
Sensitivity	NA	10mV	NA	2.1fF	7.5mV	**1.2nV**	
Resolution	1	0.01	0.12	NA	20	**20**	*deg/sec*
Bandwidth	NA	50	5	NA	NA	**10**	*Hz*

1 acc: 1 accelerometer
2 acc: 2 accelerometers
bm: bimorph
c: capacitive
em: electromagnetic
es: electrostatic
FOG: fiber optic gyroscope
l: light
pe: piezoelectric
pr: piezoresistive
polySi: polysilicon
s.e: sagnac effect
v.s: vibrating shell
N.A: not available
fq: frequency
t.n: tuning fork

From 1991 to 1995, the best resolution (0.01deg/sec) was only achieved by fiber optical gyroscopes (FOG) [5.13]. The latter can achieve small size but still in the centimeter scale. Micromachined fiber optical gyroscope are not yet available. This is the reason why vibrating micromachined gyroscopes have to be still improved. In 1996, some micromachined angular rate sensors can measure rotation rate smaller than 0.1 deg/sec [5.20, 5.23]. Further improvements should open for the best devices wide application domains including the automotive one, where the highest level of production is expected [5.37].

For the prototype gyroscopes, realized and fabricated in this Ph. D. Thesis, an industrial application can not yet be investigated. But some improvements have been brought in particular, a larger bandwidth and a reduced drift of the sensor thanks to the design improvements and to the phase locked loop driving (chapter 4). The main drawback of both prototype gyroscopes is their bad resolution limited by a large noise. The principal source of noise can be explained by the thermal noise of the piezoresistance [5.38]. With the latter, we can estimate a random walk noise of 4 deg/√sec for the second prototype gyroscope (chapter 4). For a further gyroscope design, the piezoresistive detection should be investigated more carefully to find the way to reduce this thermal noise. Moreover by comparing with other referred devices, a capacitive detection should also be investigated.

5.3 Conclusion:

This work was realized in the framework of the research of the limits in the Microtechnology with a demonstrator: a three axes navigation microsystem based on micromachined sensors [5.39]. In particular, the technical limitations in the fabrication of a silicon micromachined angular rate sensor were investigated. Micromachined gyroscopes required accurate mechanical structures even perfect shapes and a very sensitive mean of detection [5.40]. The deep etching of silicon technique should be further optimized to ensure a better homogeneity through the wafer and to obtain a better sidewalls quality. With the first prototype, the poor resolution was attributed to the parasitic vibration modes of the device but with the second prototype gyroscope, the main noise source was identified to be the thermal noise of the piezoresistances.

With an improved electronics, closed loop excitation of the prototype gyroscope shows promising results. The zero rate output was stabilized and absolute rate measurements were possible. Moreover improved long term stability was demonstrated. This points out the importance of operating an angular rate sensor in a closed loop configuration.

Silicon micromachined gyroscopes illustrate very well the Microtechnology limits because they regroups several complex aspects like dynamic actuation, high resolution and sensitivity, temperature and shock reliability, careful packaging and reliable electronics. Their application domains require high performances and would like to take advantages of the miniaturization (high production level, low cost) [5.40]. Moreover, great emulation between institutions and industries is present, because everybody is expected the same success for angular rate sensor as for pressure sensors and accelerometers.

The main motivation for this work was to study the whole aspects (design, fabrication and characterization) present in the realization of a sensor. Moreover the great impact of this field in the conferences was challenging. As the performances for industrial applications were known, it revealed the difficulties to pass from a demonstrator to an industrial prototype. Several developments like the glass micromachining for the packaging and the improved front end electronic were successful, in particular the collaboration with Professor Ch. Meier and Mr. S. Gempeler from the Engineer School (ETS) of Biel, as well as, the collaboration with Ms. Catherine Marselli from IMT for the sensor errors correction [5.41].

5.4 Outlook:

To improve the prototype gyroscopes, the following domains have to be investigated. On one hand, simulation tools for MEMS should help for the design of the sensor by including the vibrating structure with the technical parameters (residual stress in the deposited layers), the sensing means (stress or displacement conversion in voltage) and the packaging (temperature and pressure) [5.42]. And on the other hand, the electronics design should be investigated before the complete realization of the sensor to ensure a better efficiency in view of its integration [5.43, 5.44, 5.45, 5.46, 5.47, 5.48].

The electronics can provide a useful treatment of the sensor output by canceling some drawbacks like power supply and temperature drift errors [5.50, 5.51].

5.5 References

[5.1] M. Konno, S. Sugawara and S. Kudo, "Piezoelectric vibratory gyroscope as an angular velocity sensor", Electronics & Communications in Japan Part II - Electronics, Vol. 79 N°. 7 1996, pp. 40-52.

[5.2] S. Fujishima, T. Nakamura and K. Fujimoto, "Piezoelectric vibratory gyroscope using flexural vibration of a triangular bar", Proceedings of the 14th IEEE Annual Symposium on Frequency Control, 1991.

[5.3] P. Greiff, B. Boxenhorn, T. King, L. Niles, "Silicon monolithic micromechanical gyroscope", Digest of Technical Papers of the 6th International Conference on Solid-State Sensors and Actuators, Transducers '91, San Francisco, CA, June 1991, pp. 966-968.

[5.4] I. Bernstein, S. Cho, A. T. King, A. Kourepenis, P. Maciel and M. Weinberg, "A micromachined comb-drive tuning fork rate gyroscope", Proceedings of the 6th IEEE Workshop on Micro Electro Mechanical Systems, MEMS '93, Fort Lauderdale, FL, February 1993, pp. 143-148.

[5.5] S. Dalla Piazza and M. Christen, "Quartz crystal rotation rate sensors", Proceedings of the 7th European Frequency and Time Forum Neuchâtel, Neuchâtel, Switzerland, March 1993.

[5.6] K. Maenaka and T. Shiozawa, "Silicon rate sensor using anisotropic etching technology", Digest of Technical Papers of the 7th International Conference on Solid-State Sensors and Actuators, Transducers '93, Yokohama, Japan, June 1993, pp. 642-645.

[5.7] J. Söderkvist, "Micromachined gyroscopes", Digest of Technical Papers of the 7th International Conference on Solid-State Sensors and Actuators, Transducers '93, Yokohama, Japan, June 1993, pp. 638-641.

[5.8] M. W. Putty and K. Najafi, "A micromachined vibratory ring gyroscope", Technical Digest of IEEE Solid-State Sensor and Actuator Workshop, Hilton Head Island, SC, June 1994, pp. 213-220.

[5.9] A. Satoh, Y. Tomikawa and K. Ohnishi, "Piezoelectric vibratory gyro-sensor using a trident-type tuning fork resonator", Japanese Journal of Applied Physics Part 1 - Regular Papers Short Notes & Review Papers, Vol. 33 N°. 9B 1994, pp. 5361-5364.

[5.10] J. Choi, K. Minami and M. Esashi, "Silicon angular rate sensor by deep reactive ion etching", Proceedings of the International Symposium on Microsystems, Intelligent Materials and Robots, Sendai, Japan, September 1995, pp. 29-32.

[5.11] M. Hashimoto, C. Cabuz, K. Minami and M. Esashi, "Silicon resonant angular rate sensor using electromagnetic excitation and capacitive detection", Journal of Micromechanics & Microengineering, Vol. 5 1995, pp. 219-225.

[5.12] K. Tanaka, Y. Mochida, S. Sugimoto, K. Moriya, T. Hasegawa, K. Atsuchi and K. Ohwada, "A micromachined vibrating gyroscope", Sensors & Actuators A - Physical, A 50 1995, pp. 56-60.

[5.13] T. Yuhara, T. Kumagai, H. Soekawa and H. Hajioka, "Fiber-optic gyroscopes for automotive applications", Journal of Circuits Systems and Computers, Vol. 5 N°. 1 1995, pp. 17-36.

[5.14] W. A. Clark, R. Horowitz and R. T. Howe, "Surface micromachined Z-axis vibratory rate gyroscope", Technical Digest of IEEE Solid-State Sensor and Actuator Workshop, Hilton Head Island, SC, June 1996, pp. 283-287.

[5.15] A. J. Harris, J. S. Burdess, J. Cruickshank, D. Wood and G. Cooper, "A silicon membrane gyroscope with electrostatic actuation", Proceedings of the IEE Colloquium on Silicon Fabricated Inertial Instruments, London, UK, N°. 1996/227, pp. 5.1-5.7.

[5.16] T. Juneau and A. P. Pisano, "Micromachined dual input axis angular rate sensor", Technical Digest of IEEE Solid-State Sensor and Actuator Workshop, Hilton Head Island, SC, June 1996, pp. 229-302.

[5.17] P. Léger, "QuapasonTM-A new low-cost vibrating gyroscope", Proceedings of Symposium Gyro Technology 1996, Stuttgart, Germany, September 1996, 15.0-15.8.

[5.18] K. Maenaka, T. Fujita, Y. Konishi and M. Maeda, "A study of silicon angular rate sensors using anisotropic etching technology", Sensors & Actuators A - Physical, A 54 (1996), pp. 568-573.

[5.19] N. Wakatsuki, S. Kudo, H. Tanaka, O. Masaaki, S. Yamada, K. Kikuchi and M. Yamauchi, "Improvement of piezoelectric vibratory gyroscope using $LiTaO_3$ crystal", Proceedings of Symposium Gyro Technology 1996, Stuttgart, Germany, September 1996, 6.0-6.11.

[5.20] M. S. Weinberg, J. Bernstein, J. Borenstein, J. Campbell, J. Cousens, B. Cunningham, R. Fields P. Greiff, B. Hugh, L. Niles and J. B. Sohn, , "Micromachining inertial instruments", Proceedings of the SPIE 1996 Conference: Micromachining and Microfabrication Process Technology II, Austin, TX, October 1996, pp. 26-36.

[5.21] M. Yamashita, K. Minami and M. Esashi, "A silicon micromachined resonant angular rate sensor using electrostatic excitation and capacitive detection", Technical Digest of The 14th Sensor Symposium, Potsdam, Germany, 1996, pp. 39-42.

[5.22] T. Fujita, T. Mizuno, R. Kenny, K. Maenaka and M. Maeda, "Two-dimensional micromachined gyroscope ", Digest of Technical Papers of the 9th International Conference on Solid-State Sensors and Actuators, Transducers '97, Chicago, IL, June 1997, pp. 887-890.

[5.23] I. Hopkin, "Performance and design of a silicon micromachined gyro ", Proceedings of Symposium Gyro Technology 1997, Stuttgart, Germany, September 1997, pp. 1.0-1.10.

[5.24] H. Kuisma, T. Ryhänen, J. Lahdenperä, E. Punkka, S. Ruotsalainen, T. Sillanpää and H. Seppä, "A bulk micromachined silicon angular rate sensor", Digest of Technical Papers of the 9th International Conference on Solid-State Sensors and Actuators, Transducers '97, Chicago, IL, June 1997, pp. 875-878.

[5.25] M. Lutz, W. Golderer, J. Gerstenmeier, J. Marek, B. Maihöfer, S. Mahler, H. Münzel and U. Bischof, "A precision yaw rate sensor in silicon micromachining", Digest of Technical Papers of the 9th International Conference on Solid-State Sensors and Actuators, Transducers '97, Chicago, IL, June 1997, pp. 847-850.

[5.26] Y. Oh, B. Lee, S. Baek, H. Kim, J. Kim, S. Kang and C. Song, "A surface-micromachined tunable vibratory gyroscope", Proceedings of the 10th IEEE Workshop on Micro Electro Mechanical Systems, MEMS '97, Nagoya, Japan, January 1997, pp. 272-277.

[5.27] K. Y. Park, C. W. Lee, Y. S. Oh and Y. H. Cho, "Laterally oscillated and force-balanced micro vibratory rate gyroscope supported by fish hook shape springs", Proceedings of the 10th IEEE Workshop on Micro Electro Mechanical Systems, MEMS '97, Nagoya, Japan, January 1997, pp. 494-499.

[5.28] D. R. Sparks, S. R. Zarabadi, J. D. Johnson, Q. Jiang, M. Chia, O. Larsen, W. Higdon and P. Castillo-Borelley, "A CMOS integrated surface micromachined angular rate sensor : it's automotive applications", Digest of Technical Papers of the 9th International Conference on Solid-State Sensors and Actuators, Transducers '97, Chicago, IL, June 1997, pp. 851-854.

[5.29] T. K. Tang, R. C. Gutierrez, C. B. Stell, V. Vorperian, G. A. Arakaki, J. T. Rice, W. J. Li, I. Charkaborty, K. Shcheglov, J. Z. Wilcox and W. J. Kaiser, "A packaged silicon MEMS vibratory gyroscope for microspacecraft", Proceedings of the 10th IEEE Workshop on Micro Electro Mechanical Systems, MEMS'97, Nagoya, Japan, January 1997, pp. 500-505.

[5.30] Y. Tomikawa, H. Okuyama, A. Satoh, S. Sugawara, K. Ohnishi, "Flatly supported vibratory gyro-sensor using trident-type tuning fork resonator", Proceedings of Symposium Gyro Technology 1997, Stuttgart, Germany, September 1997, pp. 8.0-8.12.

[5.31] R. Voss, "Silicon micromachined vibrating gyroscopes", Proceedings of the SPIE 1997 Conference: Micromachined Devices and Components III, Austin, TX, September 1997, pp. 62-73.

[5.32] P. Mottier, P. Pouteau, "Solid state optical gyrometer integrated on silicon", Electronics Letters, Vol. 33 N°. 23, pp. 1975-1977.

[5.33] W. Geiger, B. Folkmer, J. Merz, H. Sandmaier and W. Lang, "A new silicon rate gyroscope", Proceedings of the 11th IEEE Workshop on Micro Electro Mechanical Systems, MEMS'98, Heidelberg, Germany, January 1998, pp. 615-620.

[5.34] S. An, Y. S. Oh, B. L. Lee, K. Y. Park, S. J. Kang, S. O. Choi, Y. J. Go and C. M. Song, "Dual-axis microgyroscope with closed-loop detection", Proceedings of the 11th IEEE Workshop on Micro Electro Mechanical Systems, MEMS'98, Heidelberg, Germany, January 1998, pp. 328-333.

[5.35] J. J. Choi, R. Toda, K. Minami and M. Esashi, "Silicon angular resonance gyroscope by deep ICPRIE and XeF2 gas etching", Proceedings of the 11th IEEE Workshop on Micro Electro Mechanical Systems, MEMS'98, Heidelberg, Germany, January 1998, pp. 322-327.

[5.36] T. Matsuura, K. Tsutsumi, M. Taguchi, M. Taruya, T. Hara and Y. Ohashi, "Silicon resonant angular rate sensor for vehicle stability control", SAE technical paper series , Warrendale, PA 15096-0001 USA, 980268, pp. 43-47.

[5.37] D. S. Eddy, D. R. Sparks, "Application of MEMS technology in automotive sensors and actuators", Proceedings of the IEEE, special issue: integrated sensors, microactuators and microsystems (MEMS), Vol. 86 N°. 8, August 1998, pp. 1747-1755.

[5.38] G. Gerlach, K. Sager and A. Nakladal, "How accurate are measurements with piezoresistive sensors ?", Technisches Messen, Vol. 63 N°. 11 1996, pp. 403-412.

[5.39] Y. Ansel, P. Lerch, P. Renaud, F. Paoletti, M.-A. Grétillat, N. F. de Rooij, G. Schröpfer, S. Ballandras, M. de Labachelerie, C. Marselli, H. P. Amann and F. Pellandini, "Simulation and design of a three axis navigation microsystem based on micromachined sensors", Proceedings of the 2nd International Conference: Microsim'97, Lausanne, Switzerland, September 1997, pp. 107-116.

[5.40] N. Yazdi, F. Ayazi, K. Najafi, "Micromachined inertial sensors", Proceedings of the IEEE, special issue: integrated sensors, microactuators and microsystems (MEMS), Vol. 86 N°. 8, August 1998, pp. 1640-1659.

[5.41] C. Marselli, H.P. Amann, F. Pellandini, F. Paoletti, M.-A. Grétillat and N. F de Rooij, "Error Modeling of a Silicon Angular Rate Sensor", Proceedings of Symposium Gyro Technology 1997, Stuttgart, Germany, September 1997, pp. 4.0-4.9.

[5.42] S. D. Senturia, "CAD challenges for microsensors, microactuators and microsystems", Proceedings of the IEEE, special issue: integrated sensors, microactuators and microsystems (MEMS), Vol. 86 N°. 8, August 1998, pp. 1611-1626.

[5.43] B. E. Boser, "Electronics for micromachined inertial sensors", Digest of Technical Papers of the 9th International Conference on Solid-State Sensors and Actuators, Transducers '97, Chicago, IL, June 1997, pp. 1169-1172.

[5.44] A. Burnstein, W. J. Kaiser, "Mixed analog-digital highly sensitive sensor interface circuit for low-cost microsensors", Sensors & Actuators A - Physical, A 52 N°. 1-3, pp. 193-197.

[5.45] R. Puers, "Sensor, sensor interfacing and front-end data managment for stand alone microsystems", Technical Digest of The 9th Workshop on Micromachining, Micromechanics and Microsystems, MME '98, Ulvik in Hardanger, Norway, June 1998, pp. 123-130.

[5.46] E. Schmidt, "Packaging technologies and system integration for automotive applications", Proceedings of the 5th International Conference on Micro Electro, Opto, Mechanic Systems and Components, Micro System Technologies 96, Potsdam, Germany, September 1996, pp. 45-54.

[5.47] L. Sprangler and C: J. Kemp, "ISSAC: integrated silicon automotive accelerometer", Sensors & Actuators A - Physical, A 54 (1996), pp. 523-529.

[5.48] M. Tsugai, Y. Hirata, K. Tanimoto, T. Usami, T. Araki and H. Otani, "Airbag accelerometer with a simple switched-capacitor readout ASIC", Proceedings of the SPIE 1997 Conference: Micromachined Devices and Components III, Austin, TX, September 1997, pp. 74-81.

[5.49] L. Zimmermann, J. Ph. Ebersohl, F. Le Hung, J. P. Berry, F. Baillieu, P. Rey, B. Diem, S. Renard and P. Caillat, "Airbag application: a microsystem including a silicon capacitive accelerometer, CMOS switched capacitor electronics and true self-test capability", Sensors & Actuators A - Physical, A 46-47 1995, pp. 190-195.

[5.50] A. Burnstein, W. J. Kaiser, "Self-compensating interface system for high performance MEMS inertial sensors", Proceedings of the SPIE 1996 Conference: Smart Structures and Materials 1996: Smart Electronics and MEMS, San Diego, CA, February 1996, pp. 145-154.

[5.51] C. Berthoud, M. Ansorge and F. Pellandini , "Effective static response compensation suitable for low-power ASIC implementation with an application to pressure sensors", Proceedings of the IEEE Instrumentation and Measurement Technology Conference, Brussels, Belgium, June 1996, pp. 1168-1173.

[5.52] T. Olbrich, A. Richardson, W. Vermeiren and B. Straube, "Integrating testability into microsystems", Microsystem Technologies, 1997, pp. 72-79.

Acknowledgments

First of all, I would like to thank Professor N. F. de Rooij who gave me the opportunity to do this Ph.D. Thesis and for the interest he gave to my work. Furthermore, I would like to thank Professor D. Hauden, Professor F. Pellandini and Professor J. Söderkvist who kindly accepted to be co-examiners of this Ph.D. Thesis.

Parts of this work have been funded by the Swiss National Science Foundation (FNSRS) and the Swiss Foundation for Research in Microtechnology (FSRM) in the framework (Projet Internartional de Coopération Scientifique) of an international exchange between French and Swiss Microtechnology Institutions. In particular, I would like to thank Dr. M. Ecabert from the FSRM for his great interest for the PICS project. I would like to particularly thank the Ph.D. students from the PICS group, Mr. Y. Ansel, Ms. C. Marselli and Mr. G. Schröpfer. The work with Ms. C. Marselli was of great interest and successful.

I would also particularly thank Dr. Marc Grétillat who was my senior assistant during my work at IMT. He has been a very attentive supervisor and much more since 1997, year of our wedding. Several internal collaborations have been successful and I would like to thank Mr. H. P. Amann for the improvement of the first electronic board for the gyroscope, Mr. M. Boillat who helped me to perform temperature measurements and the vacuum anodic bonding, Mr. S. Roth and Mr. P. Thiébaud for the glass micromachining, Mr. P. Torres for the deposition of amorphous silicon on glass substrates. I wisb to express my gratitude to the technical team, Mrs. S. Jenny, Ms. S. Pochon, Mr. P. -A. Clerc, Mr. S. Jeanneret who worked hard to realize the sensors and let us sharing their great experience.

I would also thank the persons who took part in the great adventure of the research laboratory of Professor N. F. de Rooij: Dr. P. Arquint, Dr. N. Blanc and Dr. L. Paratte who left the group, Ms. C. Beuret, Professor M. Koudelka-Hep, Ms. M. Rüegg, Dr. S. Verpoorte, Dr. T. Akiyama, Mr. D. Briand, Mr. Bas de Heij, Mr. L. Dellmann, Mr. B. Droz, Dr. J. C. Fiaccabrino,

Dr. K. Fluri, Mr. O. Guenat, Mr. B. Guldimann, Mr. C. Kottelat, Dr. P. Luginbuhl, Dr. C. Marxer, Mr. M. Meijerink, Dr. P. Michel, Mr. G. Mondin, Dr. W. E. Morf, Dr. W. Noell, Mr. V. Pasquier, Dr. G. A. Racine, Mr. G. Schürmann, Dr. U. Staufer, Mr. C. Stebler, Dr. D. Strike, Dr. B. van der Schoot, Dr. P. van der Wal, Mr. J. Vaquera.

I also express my gratitude to Professor S. D. Senturia at the Massachusetts Institute of Technology who gave me the opportunity to be a visiting scientist during three months in this famous North American Institute. I would thank him for his kind hospitality as well as his coworkers during the Summer 1996.

I would like to thank the following external persons who gave me a great support during my work: Dr. R. Luthier from Asulab S.A who allowed me to make the first rotation measurements, Mrs. B. Bozenda from Micronas S.A who helped me to performed the vacuum anodic bonding at Micronas S.A, Professor Ch. Meier and Mr. S. Gempeler from the ETS of Biel for the realization of the electronic boards, Mrs. M. T. Ivorra and Dr. V. Gass from Mecanex S.A for providing permanents magnets, Dr. N. C. Bui from Microswiss for his interest and financial support for the electronics.

Finally, I would give particular thanks to my family.

Merci à mes parents qui m'ont permis de faire des études et qui m'ont toujours soutenu tout au long de mon parcours. Merci à Emmanuelle et Anthony avec qui nous formons une famille heureuse et très unie malgré les distances. Merci à Marc que le travail m'a fait rencontré, apprécié et surtout aimé. Nous entendons bien continuer notre collaboration au delà du travail et mener à bien nos futurs projets.

Biography

Florence Paoletti (Grétillat) was born on March 26, 1970 in Nancy, France. She received her Engineer degree from the National Institute of Applied Science (INSA) Lyon, France, in July 1993. In March 1994 she joined the Institute of Microtechnology (IMT) at the University of Neuchâtel, as a research and teaching assistant. From June to August 1996, she was a visiting scientist at the Massachusetts Institute of Technology (MIT) in the group of Professor Stephen Senturia. She get married in August 1997 with Marc-Alexis Grétillat. Since 1994, her research interest has been including angular rate sensor, micromachining of glass and packaging of sensors and in October 1998, she defended successfully her Ph. D. Thesis entitled "Silicon Micromachined Vibrating Gyroscopes with Piezoresistive Detection and Electromagnetic Excitation".

Bibliography

- F. Paoletti, M.-A. Grétillat and N. F de Rooij, "A Silicon Micromachined Vibrating Gyroscope with Piezoresistive Detection and Electromagnetic Excitation", Proceedings of the 9th IEEE Workshop on Micro Electro Mechanical Systems, MEMS '96, San Diego, CA, February 1996, pp. 162-167.
- F. Paoletti, M.-A. Grétillat and N. F de Rooij, "A Silicon Micromachined Tuning Fork Gyroscope", Proceedings of Symposium Gyro Technology 1996, Stuttgart, Germany, September 1996, pp. 5.0-5.8.
- F. Paoletti, M.-A. Grétillat and N. F. de Rooij, "A Silicon Micromachined Tuning Fork Gyroscope", Technical digest of the IEE colloquium on Silicon Fabricated Inertial Instruments, Digest N° 1996/227, London, England, December 1996, pp. 3/1-3/6.
- M.-A Grétillat, F. Paoletti, P. Thiébaud, S. Roth, M. Koudelka-Hep and N.F. de Rooij, "A New Fabrication Method of Borosilicate Glass Capillary Tubes with Lateral Inlets and Outlets", Proceedings of the 10th European Conference on Solid-State Transducers, Eurosensor X, Leuven, Belgium, September 1996, pp. 259-262.
- M.-A Grétillat, F. Paoletti, P. Thiébaud, S. Roth, M. Koudelka-Hep and N.F. de Rooij, "A New Fabrication Method of Borosilicate Glass Capillary Tubes with Lateral Inlets and Outlets", Proceedings of Miniaturized Total Analysis Systems, μ-TAS96, Analytical Methods & Instrumentation, Basel, Switzerland, November 1996, p. 214.
- M.-A Grétillat, F. Paoletti, P. Thiébaud, S. Roth, M. Koudelka-Hep and N.F. de Rooij, "A New Fabrication Method for Borosilicate Glass Capillary Tubes with Lateral Inlets and Outlets", Sensors & Actuators, A 60 (1997), pp. 219-222.
- C. Marselli, H.P. Amann, F. Pellandini, F. Paoletti, M.-A. Grétillat and N. F de Rooij, "Error Modelling of a Silicon Angular Rate Sensor", Proceedings of Symposium Gyro Technology 1997, Stuttgart, Germany, September 1997, pp. 4.0-4.9.

- Y. Ansel, P. Lerch, P. Renaud, F. Paoletti, M.-A. Grétillat, N. F. de Rooij, G. Schröpfer, S. Ballandras, M. de Labachelerie, C. Marselli, H. P. Amann and F. Pellandini, "Simulation and design of a three axis navigation microsystem based on micromachined sensors", Proceedings of the 2nd International Conference: Microsim'97, Lausanne, Switzerland, September 1997, pp. 107-116.
- P. -A. Clerc, L. Dellmann, F. Grétillat, M. -A. Grétillat, P. -F. Indermühle, S. Jeanneret, Ph. Luginbuhl, C. Marxer, T. L. Pfeffer, G. -A. Racine, S. Roth, U. Staufer, C. Stebler, P. Thiébaud and N. F. de Rooij, "Advanced deep reactive ion etching a versatile tool for microelectromechanical systems", accepted for publication in the Journal of Microelectronics and Microengineering (JMM/95864/PAP).